Machine-Learning Assisted Atomic Simulations of Defect Dynamics in Multicomponent Concentrated Alloys

Wenjiang Huang

Dissertation submitted to the faculty of
Virginia Polytechnic Institute and State University
in partial fulfillment of the requirement for the degree of

Doctor of Philosophy
in
Materials Science and Engineering

Xianming Bai, Chair
William Reynolds
Sean Corcoran
Hongliang Xin

November 21st, 2024
Blacksburg, VA 24060

Key words: high-entropy alloys, machine learning, molecular dynamics, Monte Carlo, sluggish diffusion, short-range orders

Machine-Learning Assisted Atomic Simulations of Defect Dynamics in Multicomponent Concentrated Alloys

Wenjiang Huang

Abstract

This dissertation investigates the complex defect diffusion behaviors in concentrated solid solution alloys (CSAs) including high-entropy alloys (HEAs), which are critical for understanding their exceptional mechanical and radiation-resistant properties. Through a combination of multiple atomistic-level simulation techniques and novel machine learning methods, this work reveals how the intricacies of local atomic arrangements and chemical heterogeneities influence diffusion processes, thereby offering new insights into alloy design and optimization.

The research initially focuses on the vacancy-mediated diffusion employing binary Ni-Fe concentrated alloys as model systems. To evaluate the impact of local chemical short-range orders (SROs) on vacancy diffusion, both random solid solution configurations and alloys with SROs are prepared using hybrid molecular dynamics (MD) and metropolis Monte Carlo (MMC) methods. The results demonstrates that the development of SROs can significantly impede vacancy-mediated diffusion and enhance the chemically biased diffusion between Fe and Ni sites. Such findings suggest that the diffusion behavior in CSAs can be intricately controlled by adjusting the chemical ordering, a principle that could revolutionize alloy design strategies. Moreover, the study establishes a linear correlation between changes in the enthalpy of mixing and the formation of

SROs, indicating that the reduction of enthalpy of mixing towards the more negative direction within an alloy system acts as a driving force for the observed diffusional slowdown.

Advancing the methodological frontier, this dissertation introduces a state-of-the-art approach that integrates machine learning (ML) with kinetic Monte Carlo (KMC) simulations to efficiently investigate the controversial phenomenon of "sluggish diffusion" in concentrated alloys. As the first step, the Ni-Fe concentrated alloys are used as model systems. The complexity of defect diffusion in varying local atomic environment in CSAs makes it impractical to apply the standard nudged elastic band (NEB) method for on-the-fly determination of defect migration barriers at each step. By developing an artificial neural network (ANN) model trained on a dataset of NEB-computed migration barriers, it enables precise, efficient, and on-the-fly predictions of vacancy migration barriers for arbitrary local atomic environments during KMC simulations, including both random solution configuration and alloys with SROs. The diffusivities derived from this ANN-KMC modeling closely align with those from independent MD and temperature-accelerated dynamics (TAD) simulations at their accessible temperatures. The research delves into the sluggish diffusion mechanisms over the entire composition range of the Ni-Fe alloy system, elucidating them through the lens of ANN-KMC-derived insights at both high and low temperatures.

The exploration then extends to quinary FeNiCrCoCu HEAs, utilizing a similar but improved ANN model to predict vacancy migration barriers across a wide compositional range. Due to the challenges of exploring the vast HEA compositional space, to date most experimental and computational studies have been limited to equiatomic compositions. This model, remarkably effective despite being trained solely on equiatomic HEA data, accurately predicts vacancy

migration barriers in non-equiatomic compositions and their binary to quinary subsystems. Implementing this ANN model as an on-the-fly barrier calculator for KMC simulations, such ANN-KMC framework derives diffusivities nearly identical to the those from independent MD simulations but with far higher efficiency. This capability facilitates an extensive study of over 1,500 HEA compositions, uncovering the presence of sluggish diffusion in many non-equiatomic compositions. The analysis provides critical insights into the interplay between compositions, complex potential energy landscape, and percolation effect of the faster diffuser (i.e., Cu) on sluggish diffusion behaviors, offering invaluable perspectives for experimental alloy design and development.

Lastly, the dissertation delves into interstitial-mediated diffusion in FeNiCrCoCu HEAs, confirming the presence of sluggish interstitial diffusion by comparing the equiatomic HEA with a range of reference systems. To study the non-monotonic concentration dependences in interstitial diffusion, a machine learning KMC (ML-KMC) method has been developed to simulate ⟨100⟩ dumbbell interstitial diffusion across various HEA compositions. Diverging from conventional KMC (C-KMC) and random sample KMC (RS-KMC) approaches, which approximate transition energies through a mean-field and random sampling methods, respectively, the ML-KMC predicts dumbbell formation energy on-the-fly based on local atomic configurations. This enables it to effectively replicate diffusion patterns from independent MD simulations. This novel ML-KMC approach offers a promising high-throughput method for studying HEAs, avoiding the expensive computational overhead associated with calculating dumbbell migration barriers. The impact of the percolation effect of faster diffusing elements (Cr, Cu) is also analyzed.

Insights from this study can advance the understanding of compositional-dependent diffusion and provide valuable insights for the HEA design.

Beyond the achievement of these completed works, two promising future projects have been evaluated that could significantly advance the field of diffusion research. The first initiative seeks to broaden the scope of the ANN-KMC framework, aiming to significantly enhance simulation efficiency across a broad range of HEA compositions. An accurate ANN model for predicting interstitial migration barriers has already been developed, and its full integration into the KMC framework could enable more accurate diffusion simulations. The second project aims to develop a comprehensive ML interatomic potential tailored specifically for HEAs, intended to improve the predictive accuracy of MD simulations. Although progress has been made in modeling an equiatomic CoCrFeMnNi HEA, constructing a robust ML potential for HEAs faces substantial challenges, primarily due to the extensive data requirements and computational demands.

Machine-Learning Assisted Atomic Simulations of Defect Dynamics in Multicomponent Concentrated Alloys

Wenjiang Huang

General Audience Abstract

This dissertation investigates the complex defect diffusion behaviors in concentrated solid solution alloys (CSAs) including high-entropy alloys (HEAs), which are critical to understanding their exceptional mechanical and radiation-resistant properties. Through a combination of multiple simulation techniques and novel machine learning methods, this work reveals how the intricacies of local atomic arrangements and chemical heterogeneities influence diffusion processes, thereby offering new insights into alloy design and optimization.

The research initially focuses on the complex vacancy diffusion mechanism in concentrated Ni-Fe alloys, demonstrating that local chemical short-range orders (SROs) significantly impede vacancy-mediated diffusion. Such findings suggest that the diffusion behavior in CSAs can be intricately controlled by adjusting the chemical ordering, a principle that could revolutionize alloy design strategies. Moreover, the study revealed a linear correlation between changes in the enthalpy of mixing and the formation of SROs, indicating that the enthalpy of mixing may be important for the diffusional behavior in CSAs.

Advancing the methodological frontier, this dissertation introduces a cutting-edge approach that integrates machine learning (ML) with kinetic Monte Carlo (KMC) simulations to efficiently investigate the controversial "sluggish diffusion" phenomenon using Ni-Fe

concentrated alloys as the initial model systems. By developing an artificial neural network (ANN) model trained on pre-calculated migration barriers using the standard nudged elastic band (NEB) method, this approach enables precise, efficient, and on-the-fly predictions of vacancy migration barriers for arbitrary local atomic environments, including both random solution configuration and alloys with SROs. The diffusivities obtained from this ANN-KMC modeling closely align with independent molecular dynamics (MD) and temperature-accelerated dynamics (TAD) simulations at their accessible temperatures, but with a far better efficiency.

The ANN-KMC approach is then extended to non-equiatomic FeNiCrCoCu HEAs. An improved ANN model is developed to predict vacancy migration barriers across a wide compositional range. This model, remarkably effective despite being trained solely on equiatomic HEA data, accurately predicts vacancy migration barriers in non-equiatomic compositions and their binary to quinary subsystems. This capability facilitates an extensive study of over 1,500 HEA compositions, uncovering the presence of sluggish diffusion in many non-equiatomic compositions. The analysis provides critical understanding of the diffusion behavior in a vast compositional space, offering invaluable insights for experimental alloy design and development.

Lastly, the dissertation delves into interstitial-mediated diffusion in FeNiCrCoCu HEAs, confirming the presence of sluggish interstitial diffusion. A machine learning KMC (ML-KMC) method has been developed to simulate $\langle 100 \rangle$ dumbbell interstitial diffusion across various HEA compositions, closely replicating diffusion patterns as independent MD simulations. This novel ML-KMC approach offers a promising high-throughput method for studying HEAs, avoiding the expensive computational overhead associated with calculating migration barriers. The impact of the percolation effect of faster diffusing elements (Cr, Cu) is also analyzed.

Regarding future research directions, two promising projects are evaluated. The first expands the ANN-KMC framework to render more accurate interstitial diffusion simulations, and the second focuses on developing a ML potential for an equiatomic CoCrFeMnNi HEA. The progresses and challenges are discussed.

Dedication

To my dad and mom, my wife Qiaoqiao, my young sister Shuhui, and my cat NaiCha

Acknowledgements

First and foremost, I would like to express my deepest gratitude to my mentor, Dr. Xianming Bai, for his invaluable guidance, patience, and unwavering support throughout every stage of my dissertation. His insightful feedback and encouragement were pivotal in overcoming the challenges I encountered during my research. My time under his mentorship has been the most memorable and enriching experience of my life, one that will undoubtedly shape my future career.

I extend my sincere thanks to my committee members, Dr. William Reynold and Dr. Sean Corcoran from the Materials Science and Engineering Department, and Dr. Hongliang Xin from the Chemical Engineering Department, for their expert advice and constructive critiques. Their diverse perspectives and rigorous evaluations have been instrumental in refining my research work. Special appreciation goes to Ms. Kim Grandstaff and Ms. Cindy Perdue for their administrative assistances. A heartfelt thank you to my groupmates, Dr. Yaxuan Zhang, Dr. Weiming Chen, Dr. Ziqi Xiao, Dr. Jarin French, and Dr. Axel Alcocer Seoane, for their invaluable help and support.

I acknowledge the financial support from the National Science Foundation (NSF) under Grant No. 1847780. I also thank the Advanced Research Computing (ARC) at Virginia Tech for providing the high-performance computational resources for this work.

Last but certainly not least, I dedicate a special acknowledgment to my family and my wife. The values of hard work and education instilled in me by my parents, the ceaseless encouragement from my siblings, and the constant companionship, confidence, and inspiration provided by my wife have been the cornerstones of my journey. Their unwavering support and belief in me have been my greatest motivators.

Attribution

This dissertation is a collaborative effort that benefited from the contributions of multiple scientists and colleagues. Below is a brief description of the contributions to each chapter:

Chapter 2: I was responsible for conducting all simulations and drafting the manuscript as the lead author. Dr. Xianming Bai provided the research outline and major direction for this study, contributed to discussions on simulation details, and assisted with manuscript revisions. This manuscript is intended for submission to a peer-review journal in the future.

Chapter 3: My role included conducting all simulations, programming, and drafting the manuscript as the lead author, with Dr. Bai providing the research outline, major direction, and detailed discussions on simulation aspects. Dr. Bai also assisted with manuscript revisions and served as the corresponding author.

This chapter reproduces work from our publication [Huang, W., & Bai, X. M. (2023). Machine learning based on-the-fly kinetic Monte Carlo simulations of sluggish diffusion in Ni-Fe concentrated alloys. Journal of Alloys and Compounds, 937, 168457], with permission from Elsevier.

Chapter 4: I conducted all simulations, programming, and took the lead in manuscript preparation. Dr. Bai guided the research direction and engaged in discussions about the simulation details, besides helping with manuscript revisions. He served as the corresponding author. Dr. Diana Farkas from our Materials Science and Engineering Department also provided the average atom potentials for simulations as well as insightful assistance for reviewing and revising the manuscript.

This chapter reproduces work from our publication [Huang, W., Farkas, D., & Bai, X. M. (2023). High-throughput machine learning-Kinetic Monte Carlo framework for diffusion studies in Equiatomic and Non-equiatomic FeNiCrCoCu high-entropy alloys. Materialia, 32, 101966], with permission from Elsevier.

Chapter 5: My contributions include conducting all simulations and leading the manuscript preparation as the lead author. Dr. Bai provided the research outline, the major direction for the study, participated in simulation detail discussions, and supported manuscript revisions. This manuscript is intended for submission to a peer-reviewed journal in the future.

Chapter 6: I was responsible for all simulations and drafting a milestone report. Dr. Bai contributed the research outline and the study's major direction.

Table of Contents

List of Figures

List of Tables

CHARPTER 1 Introduction

1.1 Background

In the evolving landscape of material science, the advent of concentrated solid solution alloys (CSAs), in particular the high-entropy alloys (HEAs) that contain five or more nearly equiatomic components [1], has marked a paradigm shift, challenging conventional alloy design principles and ushering in a possibly new era of material engineering. Characterized by their multi-component and nearly equiatomic compositions, HEAs could collectively give desirable properties such as excellent mechanical properties at both low and high temperatures [2, 3], good corrosion resistance [4], and enhanced radiation tolerance [5, 6]. The underlying chemical complexity in HEAs, arising from the homogenous or heterogenous distribution of multiple elemental species, plays a pivotal role in their unique properties. The complex atomic configurations in CSAs or HEAs may lead to the sluggish diffusion, which has been commonly quoted as the origin behind those remarkable properties observed in HEAs [7-9]. However, its existence remains a subject of debate. The efforts to demystify the sluggish diffusion in HEAs have spanned extensively, through both experimental and atomic-scale simulation studies [10-15]. For example, one prevalent debate around sluggish diffusion highlights that its existence often is observed at the homologous temperature scale rather than the absolute temperature scale [11]. These findings underscore the importance of thoroughly examining sluggish diffusion to propel the design and development of HEAs forward.

Experimental investigation of the diffusion properties in CSAs or HEAs presents substantial challenges, particularly in interpretating interdiffusion or tracer diffusion coefficients

derived from the measured components profiles. Moreover, the expansive compositional space of HEAs makes exhaustive experiments impractical. In this context, atomic simulations of point defects such as vacancy- and interstitial-mediated diffusion may offer valuable insights, as they can directly investigate the specific mechanisms of interest. Recent advancements have deepened our understanding of sluggish diffusion in CSAs or HEAs, particularly through the lens of vacancy-mediated processes. For example, Osetsky et al. have demonstrated that in Ni-Fe concentrated alloys, the sluggish nature of compositional-dependent diffusivity arises primarily from a blend of site percolation and chemical-biased diffusion [16]. However, the sluggish diffusion mechanism becomes increasingly complex with the addition of more components in CSAs. For instance, a study on concentrated CoCrNi ternary alloys has suggested that the potential energy landscape, rather than the percolation effect, plays a more critical role in affecting diffusion sluggishness [17]. These observations suggest caution should be taken for extrapolating findings from simpler CSAs to more complex CSAs/HEAs, highlighting the need of focused research to deepen our understanding of sluggish diffusion. Furthermore, while it is often assumed that alloying elements in CSAs/HEAs are randomly distributed to form a single-phase solid solution, such as face-centered-cubic (fcc) and body-centered-cubic (bcc) phases, numerous experimental evidence has revealed that CSAs/HEAs may contain some extent of short-range orders (SROs) or other ordered phases, and the effects of such non-random structures cannot be overlooked [18-20].

Molecular dynamics (MD) presents a direct and thus presumably more accurate method for examining atomic transport through thermally activated migration of lattice defects. *Ab initio* MD, the most precise variant of MD, demands significant computational resources and has thus far been limited to analyzing interstitial-mediated diffusion mechanisms in small systems (~ 100

atoms). If a reliable interatomic potential is used and a sufficient trajectory of defects or solute jumps is simulated, classic MD can offer reasonably accurate estimations of diffusion parameters, such as diffusion coefficients and mechanisms. However, the utility of MD is constrained by its inherently short timescale, typically up to a few tens of nanoseconds. This limitation becomes evident in the study of complex CSAs, where, for instance, MD simulations have shown that diffusion coefficients in Ni-Fe concentrated alloys were not converged until reaching the microsecond timescale [16]. While the timescale of MD simulations can be extended to microseconds with significant computational resources, this often remains impractical due to the extensive compositional space exploration required for CSAs, even more for HEAs. Consequently, in studies of vacancy-mediated diffusion, the temperature range is usually restricted to higher temperatures [21], in that some rare but important diffusion events at low temperatures might not be captured by MD. In this regard, the kinetic Monte Carlo (KMC) method has been employed in attempts to extend the diffusion simulation timescale as well as the temperature range for CSAs or HEAs, as reported in [22, 23]. However, the conventional KMC method struggles to accurately represent their complex potential energy landscape (PEL) because the energy barrier for each defect migration can vary significantly depending on the local atomic configurations (LACs) in CSAs or HEAs. To approximate the intricate PEL, techniques such as the random sampling method and the species-average migration barrier method have been developed [22-24]. But these strategies tend to oversimplify the influence of the diverse atomic configurations on diffusing objects, potentially leading to inaccurate conclusions. For a KMC simulation to be reliable, it is essential to precisely determine the migration barriers for each defect jump, such as on-the-fly calculations of these barriers through methods like the nudge elastic band (NEB) [25] or the

activation relaxation technique nouveau (ARTn) [26]. However, such requirement significantly increases computational demands and is often impractical.

In recent years, machine learning (ML) has emerged as a promising tool for tackling high-dimensional and complex problems, garnering significant interest from researchers in the field of materials science [27-31]. This dissertation introduces two innovative approaches for diffusion simulations in CSAs/HEAs. For vacancy diffusion, ML models have been developed to predict the relationship between vacancy migration barriers and LACs. These models function as efficient on-the-fly calculators within KMC simulations, significantly reducing the reliance on traditional, computationally intensive barrier calculation methods like the nudged elastic band (NEB) or the activation-relaxation technique (ARTn). This ML-KMC methodology streamlines the study of vacancy diffusion in HEAs, offering a much more efficient approach. On the other hand, for interstitial diffusion, another ML-KMC method has been crafted to simulate $\langle 100 \rangle$ interstitial dumbbell diffusion across varied HEA compositions. By dynamically predicting the dumbbell formation energy based on LACs, the ML-KMC method accurately replicates diffusion patterns, as corroborated by independent MD simulations. These advancements not only accelerate the exploration of complex diffusion mechanisms in CSAs and HEAs but also markedly improve the simulation efficiency, particularly in scenarios where MD simulations are not feasible.

In this dissertation, the exploration of vacancy- and interstitial-mediated diffusion is conducted through a synergistic approach that combines ML, KMC, MD, and temperature-accelerated dynamics (TAD). This investigation primarily focuses on uncovering the phenomena

and underlying mechanisms of sluggish diffusion, aiming to provide insightful guidance for alloy exploration and design. The study initially starts with relatively simple binary concentrated alloys, specifically Ni-Fe systems, serving as foundational models. In this work, a promising ML-KMC model is developed, enabling detailed discussions on the short-range order effects and the mechanisms behind vacancy-mediated sluggish diffusion. Building on the successes achieved in the binary systems, the research is then extended to more complex quinary HEAs, using FeNiCrCoCu alloys as model systems. Here, the ML-KMC model is further refined to facilitate high-throughput simulations of non-equiatomic HEA compositions, thereby advancing our comprehension of vacancy sluggish diffusion phenomena. Additionally, the ML-KMC method is developed to adeptly simulate interstitial diffusion in HEAs. This progressive exploration from binary to quinary systems, and from vacancy to interstitial diffusion, illustrates a methodical strategy designed to probe the intricate diffusion behaviors in HEAs.

Acknowledging the crucial importance of precise force-field descriptions in atomic simulations, this dissertation also outlines an aspirational future direction where the author intends to develop a machine learning-driven methodology to craft interatomic potentials with density functional theory (DFT)-level accuracy. This forward-looking ambition aims to significantly refine the predictive accuracy of the ML-KMC framework, ensuring simulations that closely mirror the complexities of real-world alloy behaviors. This endeavor represents a promising extension of the current work, aiming to bridge the gap between theoretical models and practical alloy design through the power of machine learning and advanced computational techniques.

1.2 Objectives

In this work, the objectives are to employ atomic-scale simulations, including molecular dynamics (MD), temperature-accelerated dynamics (TAD), and kinetic Monte Carlo (KMC), alongside machine learning techniques, to investigate the dynamics of defects with a focus on elucidating the sluggish diffusion mechanism. The investigations range from binary Ni-Fe model systems to more complex quinary Fe-Ni-Cr-Co-Cu model systems. The following sections provide concise overviews of each chapter.

In Chapter 2, MD simulations are conducted to study the impacts of short-range orders (SROs) on the vacancy-mediated diffusion using Ni-Fe as model systems.

In Chapter 3, a machine learning model, artificial neural network (ANN), is developed to accurately predict vacancy migration barriers for arbitrary atomic configurations in Ni-Fe model systems. This ANN model is then coupled with the KMC (ANN-KMC) to investigate vacancy sluggish diffusion at a wide range of alloy compositions and temperatures.

In Chapter 4, based on achieving satisfactory results within binary systems from Chapter 3, the ANN-KMC model is refined and extended to five-component HEAs using FeNiCrCuCu as a new model system. This expansion allows us to investigate a wide compositional space in an efficient manner, including both equiatomic and non-equiatomic compositions, thereby enabling high-throughput exploration of the vast compositional space of HEAs and studying their vacancy/species diffusion behaviors.

In Chapter 5, molecular dynamics (MD) simulations are employed to examine the sluggish diffusion behaviors of self-interstitial atoms in an equiatomic FeNiCrCoCu HEA at various temperatures. In addition, a machine learning kinetic Monte Carlo (ML-KMC) method is developed to accurately replicate the diffusion patterns observed in these MD simulations across different HEA compositions. This approach offers a viable solution for high-throughput modeling of HEAs over long timescales and enables the investigation of rare events where traditional MD simulations are impractical.

In Chapter 6, two forward-looking projects are presented. The first project involves developing an ML model to accurately predict interstitial migration barriers. Fully integrating this model within the KMC framework offers substantial potential for pioneering research in diffusion dynamics. The second project focuses on creating a ML potential specifically tailored for HEAs. This initiative aims to enhance the predictive accuracy of both the ANN-KMC framework and MD simulations. While there have been some progresses in modeling the equiatomic CoCrFeMnNi HEA, the creation of a fully realized ML potential for broader HEA applications poses a considerable challenge due to the need of vast datasets and significant computational resources.

CHATPTER 2 Short-Range Order Effects in Vacancy-Mediated Diffusion in Concentrated Ni-Fe Alloys

2.1 Introduction

The term of concentrated solid solution alloys (CSAs), including high-entropy alloys (HEAs), refers to alloys that have multiple principal alloying elements in high concentrations, which could collectively give desirable properties such as excellent mechanical strength at high temperatures and outstanding fracture toughness at low temperatures [2, 32], as well as good corrosion and radiation resistance [33, 34]. Most of these properties are closely related to atomic-level defect or solute diffusion kinetics. While plenty of experimental and computational efforts have been conducted with the aim of understanding the atomic diffusion mechanisms in such complex alloy systems, one of the salient features pertaining to CSAs, the so-called "sluggish diffusion" core effect, still lacks the common consensus. The sluggish diffusion in HEAs gained initial support from a landmark diffusion experiment by Tsai et al. in 2013 [35], demonstrating lower diffusion coefficients in an equiatomic CoCrFeMnNi alloy compared to conventional alloys or pure components at the homologous temperature scale (T/T_m, where T_m denotes the melting temperature). The researchers attributed this phenomenon to the inherent chemical disorder and potential energy fluctuations in HEAs, suggesting that a multitude of low-energy lattice sites can act as diffusion traps, thereby significantly slowing the diffusion kinetics. Such sluggish diffusion has also been reported in other studies; for instance, Zhao et al. observed significantly slower coarsening of $L1_2$ precipitates an $(NiCoFeCr)_{94}Ti_2Al_4$ HEA compared to a Ni-based counterpart [36].

However, the existence and universality of sluggish diffusion in HEAs are subjects of ongoing investigation. One prevalent debate around sluggish diffusion highlights its existence often observed at the homologous temperature scale rather than the absolute temperature scale. For example, Vaidya et al. reported faster diffusivities in a five-component CoCrFeMnNi HEA compared to a four-component CoCrFeNi HEA when measured on the absolute temperature scale [37]. This discrepancy can be partly attributed to lower melting point of Mn, which influences the equilibrium vacancy concentration and thus the diffusion rates at different temperature scales [38]. Moreover, Dabrowa et al. highlighted that sluggish diffusion, when evaluated on a homologous temperature scale, could also be observed even in binary Mn-containing alloys [11]. In terms of the trapping effects induced by the chemical complexity, Seoane et al. [21] conducted molecular dynamics (MD) simulations to demonstrate that the presence of compositional complexity in an HEA does not necessary induce sluggish diffusion with respect to a hypothetical single-element average atom material. Similarly, Mehta et al. found that the experimentally measured diffusivities of many HEAs did not inversely correlate with the potential energy fluctuation as postulated in the HEA concept [39]. These findings underscore the importance of thoroughly examining sluggish diffusion to propel the design and development of HEAs forward.

While the formation of a single-phase random solid-solution concentrated alloy (CSA) is ideal to maximize configurational entropy as per the high-entropy alloy concept, in practice, many CSAs/HEAs demonstrate varying degrees of short-range orders (SROs) or even ordering phases [40-43]. For example, it has been observed that external factors, such as radiation, can facilitate the development of SROs in some CSAs [41, 44]. The existence of SROs is expected to further affect many materials properties on the top of chemical disorder, including the atomic diffusion.

This is because SROs alter the local atomic configurations and thus can change the distributions of defect formation and migration energies [45-47]. However, experimentally isolating the effects of SROs presents a significant challenge due to the difficulty in creating two distinct atomic configurations (a random solution vs one with SROs) for the same alloy composition. Consequently, atomistic modeling has become a preferred approach for comparing the influence of SROs on material properties by contrasting a SRO-containing alloy with its random solid-solution counterpart.

To study the effects of SROs, a hybrid Monte Carlo (MC) and MD simulations have been widely employed to generate crystal structures with local orderings [45, 47, 48]. For instance, Zhao et al. explored interstitial and vacancy diffusion in a CuNiCoFe HEA, finding that SROs can impede interstitial diffusion while facilitating vacancy diffusion [45]. Also, Xing et al. examined vacancy-mediated diffusion in face-centered cubic (fcc) CrCoNi and body-centered cubic (bcc) MoNbTa alloys, discovering that SROs can reduce vacancy diffusivity by enhancing the roughness of the potential energy landscape [48]. Additionally, Manzoor et al. investigated the impact of SROs on vacancy diffusion in fcc NiCoCr, fcc CoCuFeNiPd, and bcc HfNbTaZr alloys [47]. Their results showed that SROs can significantly retard vacancy diffusion in NiCoCr and HfNbTaZr. These atomistic modeling studies illustrate that SROs can variably affect defect diffusion (either hinder or enhance), underscoring the necessity for further investigation into their complex influences.

The development of SROs is often attributed to the non-ideal mixing behavior in some CSAs, where the enthalpy of mixing (ΔH_{mixing}) has a non-zero value. Other factors such as

magnetic state [40, 49] and local lattice distortion [43] could also affect the development of SROs. To investigate the impact of ΔH_{mixing}, Jin et al. conducted MD simulations to study cascade damage in concentrated Ni-Fe alloys with various compositions. Their results revealed a linear correlation between the cascade damage and the ΔH_{mixing} [50], suggesting a significant role of ΔH_{mixing} in the evolution of defects within CSA. Despite these insights, the direct effects of the ΔH_{mixing} on defect diffusion in CSAs are still largely unexplored.

In this study, we aim to elucidate the correlation between SROs and the ΔH_{mixing}, and their influences on vacancy diffusion using $Ni_{1-x}Fe_x$ (x = 0 – 1) alloy as a model system. This particular alloy is chosen because it exhibits pronounced sluggish diffusion [16]. Our results revealed that the development of SROs is linearly correlated with the decrease in ΔH_{mixing} (i.e., more negative ΔH_{mixing}), leading to reduction in both tracer diffusion coefficients and self-diffusivities. Furthermore, the analysis of the distributions of vacancy migration barriers and formation energies reveals that the presence of SROs can enhance the chemically biased diffusion.

2.2 Methods

2.2.1 MD simulations

Two groups of fcc $Ni_{1-x}Fe_x$ (x = 0 – 1) alloy structures were studied in this work: random atomic configurations (denoted as “Random” structures) and SROs-containing configurations (denoted as “MMC” structures). Each group comprises eight alloy compositions with x_{Fe} = 10%, 20%, 25%, 35%, 50%, 65%, 80%, 90%. All structures were modeled within a simulation box

consisting of 10 × 10 × 10 fcc unit cells. For the Random structures, Ni and Fe atoms were randomly mixed across all compositions. To generate MMC structures, a hybrid Monte Carlo (MC) + MD method, similar to the metropolis MC method, was employed using the LAMMPS [51]. The Embedded Atom Method (EAM) interatomic potential [52] was used for the MC+MD optimization and all subsequent simulations. During a MC+MD optimization, pairs of randomly selected Ni and Fe atoms were swapped, with the acceptance probability of each swap based on the change in the system potential energy. After each swap, the system was equilibrated by a short (0.01 ps or 5 timesteps) MD run under the NVT (constant number of atoms, volume, and temperature) ensemble at 300 K. This procedure was repeated for a total of 400,000 MC steps. The resulting MMC structures consistently show lower potential energies compared to their Random counterparts. Figure 2.1 illustrates the evolution of potential energy during the MC+MD optimization of an $Ni_{50}Fe_{50}$ alloy. The characteristics and implications of the SRO presence in these structures will be thoroughly examined in the *Results 2.3.*

MD simulations were performed to compute vacancy diffusivities in both Random and MMC structures at temperature ranging from 900 to 1300 K. Each simulation system was initialized with a single vacancy and conducted within the NPT ensemble (constant number of atoms, pressure, and temperature). Temperature and zero-bar pressure control were achieved using the Nose-Hoover thermostat and barostat [53] respectively. The simulations employed a time step of 2 fs. To obtain reliable statistics of vacancy diffusivity at each simulation condition, ten independent simulations with each up to 100 ns were conducted at lower temperatures (900 and 1000 K); whereas six independent simulations with each up to 40 ns were conducted at higher

temperatures (1100 to1300 K), as the vacancy diffuses faster at high temperatures. The vacancy diffusion coefficient at each condition was calculated by the Einstein relation [54],

$$D_V = \frac{ASD}{6t} \tag{2.1}$$

where ASD is the atomic square displacement and t is the simulation time. The self-diffusion coefficient was calculated by considering the equilibrium vacancy concentration, written as,

$$D_{self} = \exp\left(-\frac{Q_f}{k_B T}\right) \cdot D_V \tag{2.2}$$

where k_B is the Boltzmann constant, T is temperature, and Q_f is the vacancy formation energy. In CSAs, Q_f is approximated as the mean value of vacancy formation energy distribution.

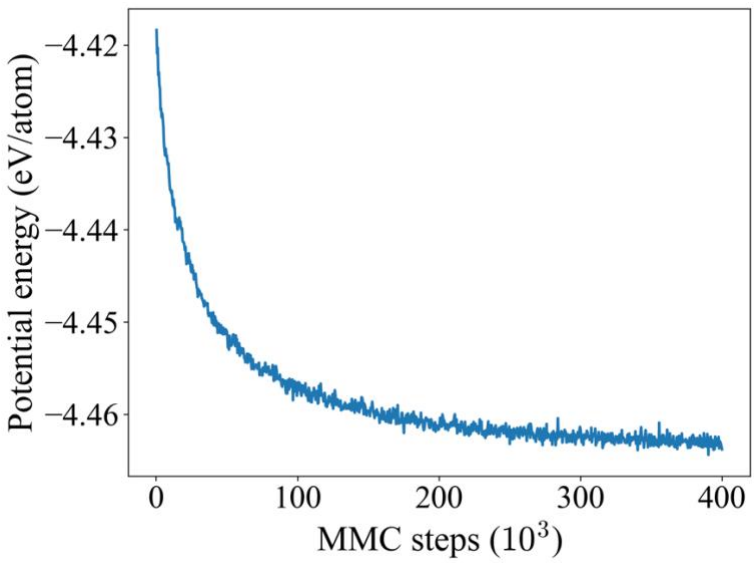

Fig. 2.1. Potential energy change of an $Ni_{50}Fe_{50}$ alloy starting from an initial Random structure to an MMC structure using a hybrid MC + MD optimization.

2.2.2 SROs and enthalpy of mixing (ΔH_{mixing})

The Warren-Cowley SRO parameter [55] was used to measure the degree of SROs for different elemental pairs (i.e., Ni-Ni, Ni-Fe, and Fe-Fe), written as,

$$\alpha_k^{ij} = 1 - \frac{p_k^{ij}}{c_j} \tag{2.3}$$

where p_k^{ij} represents the conditional probability of finding an *j*-type atom surrounding the *i*-type atom at its kth nearest-neighboring shell, and c_j denotes the concentration of the species *j*. An α_k^{ij} value of zero suggests that *i-j* pairs are randomly distributed, while a positive (negative) α_k^{ij} value indicates a tendency of unfavored (favored) *i-j* pairs at the kth shell. The enthalpy of mixing (ΔH_{mixing}) of the $Ni_{1-x}Fe_x$ alloy system is defined as,

$$\Delta H_{mixing} = H_{Ni_{1-x}Fe_x} - (1 - x_{Fe})H_{Ni} - x_{Fe}H_{Fe} \tag{2.4}$$

where $H_{Ni_{1-x}Fe_x}$, H_{Ni}, and H_{Fe} are the enthalpies per mole of the $Ni_{1-x}Fe_x$ alloy and the corresponding pure fcc Ni and Fe metals, respectively.

2.2.3 Vacancy migration barriers

The nudged elastic band (NEB) method [25] was used to calculate the vacancy migration barriers (E_m) for both Random and MMC structures. At each alloy structure, a vacancy was created

at each lattice site, one at a time. Then a vacancy migration path was randomly chosen between the vacancy and one of its twelve 1st nearest-neighboring atoms. This results in 4,000 migration barrier calculations for each composition. To test if this sampling method is sufficient for obtaining an accurate distribution of the migration barriers, a full calculation of all twelve migration barriers at each vacancy site was also conducted, which leads to 48,000 barriers as the benchmark. Fig. 2.2 shows that the two approaches result in nearly identical barrier distributions in an $Ni_{80}Fe_{20}$ Random alloy. Therefore, the first approach was used for obtaining the migration barriers for all other compositions as it has a lower computational cost. In all NEB calculations, the number of NEB images (including the initial and final states) is 13 and the spring constant is set to 1.0 eV/Å^2.

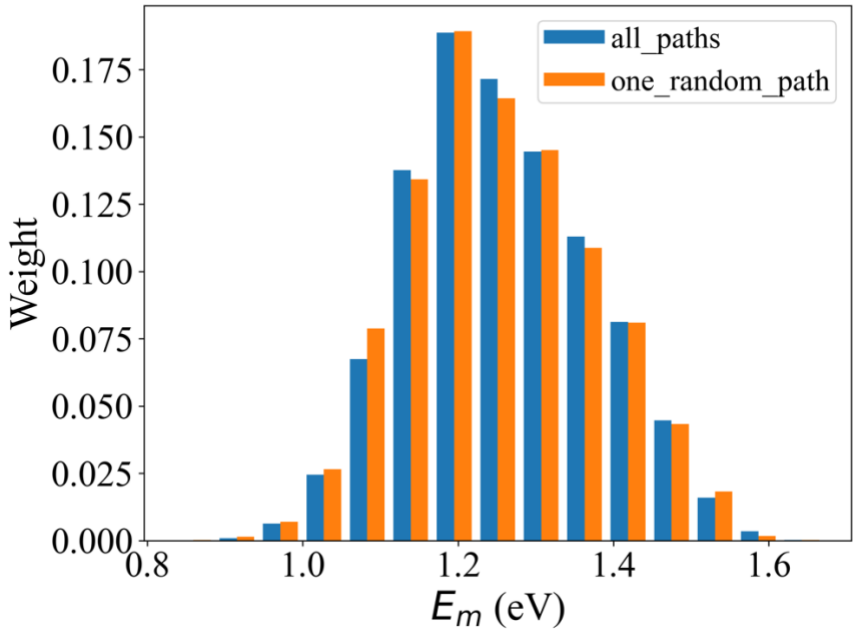

Fig. 2.2. Vacancy migration barrier distribution in an $Ni_{80}Fe_{20}$ Random alloy that is obtained by (1) randomly selecting one migration path from twelve migration paths and (2) calculating all twelve migration paths at each vacancy site.

2.2.4 Vacancy formation energies

A vacancy formation energy (E_f) was calculated by comparing the energy difference between a defective configuration that contains a vacancy and a defect-free reference configuration. At each Ni-Fe composition, a vacancy was created at every lattice site *i*, one at a time, and the E_f at the site *i* was computed by,

$$E_f^i = E_v^i - E_0 + \mu_i \tag{2.5}$$

where E_v^i and E_0 are the total potential energies of defective and reference systems, respectively; μ_i is the chemical potential of the removed atom (Ni or Fe) at the site *i*. To compute μ_i, the Widom-type substitution method [56] was used. This approach quantifies the difference in chemical potentials between two different atomic species based on the energy difference observed before and after one atomic species is substituted for the other, written as,

$$\mu_i - \mu_j = E_{ij} - E_0 \tag{2.6}$$

$$N_i\mu_i + N_j\mu_j = E_{ij} \tag{2.7}$$

where E_{ij} is the current potential energy after using an atomic species *i* to replace an original *j* species, and N_i and N_j denote the number of species *i* and *j* in the current configuration, respectively.

2.3. Results

2.3.1 The development of SROs

The SRO values for Ni-Fe pairs in both Random and MMC structures across various compositions are depicted in Fig. 2.3(a). It is evident that the Random structures lack distinct ordering tendencies, as indicated by SRO values close to zero for all shells at every composition. In contrast, the MMC structures display notable ordering tendencies, particularly in the second and third coordination shells, with less pronounced ordering in the first and fourth shells. Therefore, the MMC structures are characterized by a predominance of like pairs (Ni-Ni or Fe-Fe) in the second shells and unlike pairs (Ni-Fe) in the third shells. In addition, the degree of ordering is maximized at $x_{Fe} = 35\%$ and 65%. To further elucidate the structural differences between Random and MMC configurations, the radial distribution functions *g(r)* for Ni-Fe pairs were calculated for both groups across different compositions, as illustrated in Fig. 2.3(b). Generally, MMC structures exhibit smaller peaks for the second nearest neighbors but larger peaks for the third nearest neighbors, compared to their Random counterparts. The most significant differences are observed at $x_{Fe} = 35\%$ and 65%, aligning with the SRO observations presented in Fig. 2.3(a)

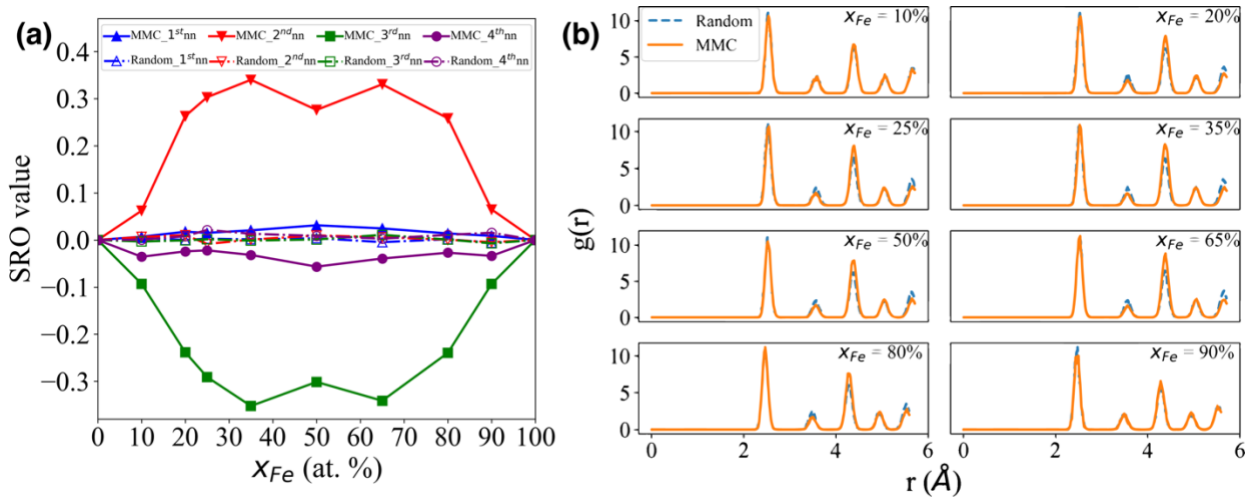

Fig. 2.3 (a) SRO values for Ni-Fe pairs up to the fourth nearest neighbor (nn) in both Random (dashed lines) and MMC (solid lines) structures. (b) Radial distribution functions *g(r)* for Ni-Fe pairs in the Random and MMC structures.

2.3.2 Correlation between SRO and ΔH_{mixing}

Figure 2.4(a) compares the ΔH_{mixing} between Random and MMC structures across different compositions. The MMC structures consistently exhibit lower ΔH_{mixing} values across the entire compositional spectrum than their Random counterparts, indicating a stronger ordering effect between atoms in MMC structures. The percentage change, $\delta(\Delta H_{mixing}) = (\Delta H_{mixing}^{MMC} - \Delta H_{mixing}^{Random}) / \Delta H_{mixing}^{Random}$, is calculated and shown in Fig. 2.4(b). It shows a peak value when $x_{Fe} =$ 35% or 65%, which coincides with the maximum SRO values as discussed in Fig. 2.3(a). A linear regression analysis between $\delta(\Delta H_{mixing})$ and SRO values at the second shell, as shown in the inset of Fig. 2.4(b), reveals a significant linear correlation with R^2 of 0.96. This suggests that the changes

in ΔH_{mixing} are directly responsible for the development of SROs. For clarity, the subsequent discussion in this section will compare the SRO-induced changes in diffusion properties (i.e., diffusivity, migration barrier, and formation energy) with the $\delta(\Delta H_{mixing})$, to explore whether there are clear correlations between them.

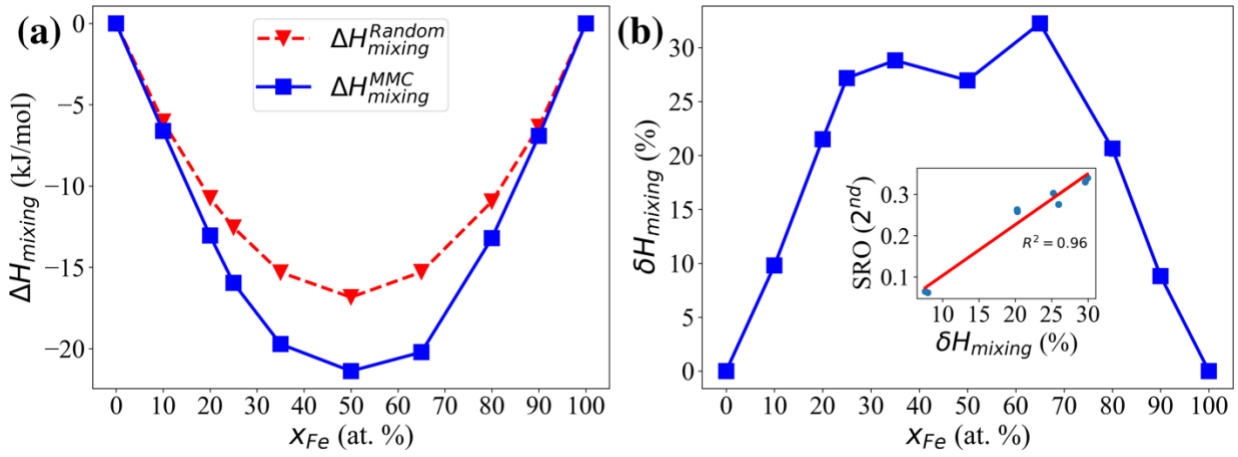

Fig. 2.4 (a) Enthalpy of mixing (ΔH_{mixing}) in Random and MMC structures for different compositions. (b) The $\delta(\Delta H_{mixing})$ between Random and MMC structures. The inset is the linear regression between $\delta(\Delta H_{mixing})$ and SRO values at the second shell.

2.3.3 Diffusivities of Random and MMC structures

Figure 2.5(a) shows the total vacancy diffusion coefficients from both Random and MMC structures across the entire composition, at temperatures from 900 K to 1300 K. Notably, the MMC structures exhibit lower vacancy diffusivities than the Random structures at most compositions (e.g., x_{Fe} = 10 – 80 at. %). The lowest vacancy diffusivity in the Random structures is observed

near the Fe percolation threshold, approximately at x_{Fe}~ 20 at. %, aligning with the prior work [16]. However, the point of minimum diffusivity in the MMC structures shifts to x_{Fe} of 25 ~ 35%. The percentage change in diffusivity between Random and MMC structures, $\delta_D = \left(D_V^{MMC} - D_V^{Random}\right)/D_V^{Random}$ is calculated and presented in Fig. 2.5(b). The predominance of negative δ_D value indicates slower diffusivities in the MMC structure, e.g., at 900 K, the diffusivity in the $Ni_{50}Fe_{50}$ MMC structure is 70% lower than its Random counterpart. Additionally, the δ_D curves exhibit a strong negative correlation with the $\delta(\Delta H_{mixing})$ curve. This is demonstrated by a linear correlation R^2 of 0.91 when performing linear regression between δ_D at 900 K and $\delta(\Delta H_{mixing})$, as shown in the inset of Fig. 2.5(b), which suggests that a decrease in the enthalpy of mixing (more negative) directly leads to reduced vacancy diffusivity.

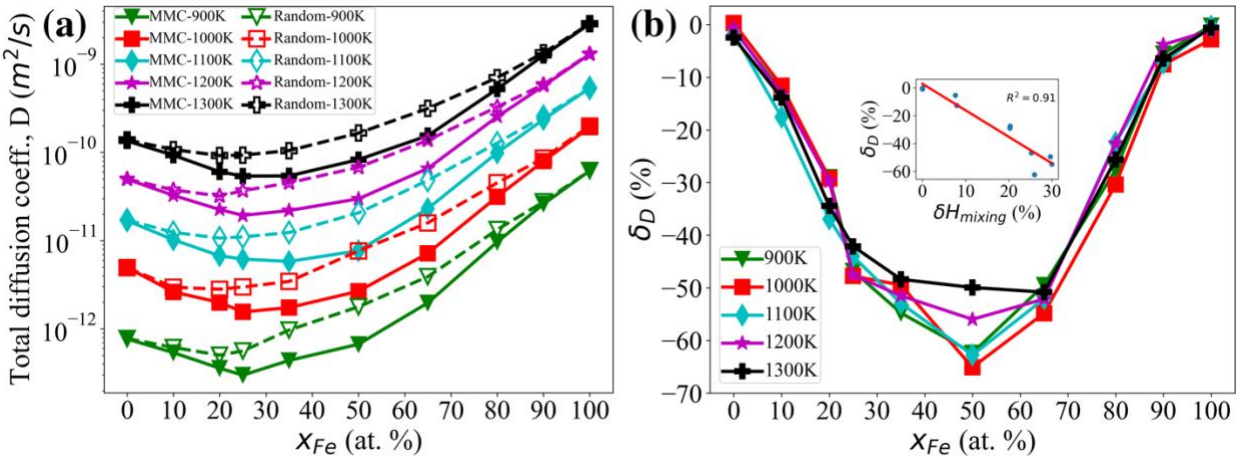

Fig. 2.5 (a) Total vacancy diffusivities in the Random and MMC structures at temperatures from 900 to 1300 K. Each data point is averaged over 6 to 10 independent MD simulations. (b) The percentage diffusivity change δ_D between Random and MMC structures.

Figure 2.6(a) shows the self-diffusivities of Random and MMC structures across the full composition and temperature ranges, which are calculated by Equation (2.2). Consistent with previous findings, the MMC structures exhibit lower self-diffusivities compared to the Random structures. The lowest self-diffusivities for both structural types are observed at x_{Fe} of 50 at. %, likely reflecting the minimum ΔH_{mixing} at this equimolar composition aforementioned in Fig. 2.4(a). The percentage change in self-diffusivity, $\delta_{D_{self}}$, is calculated and shown in Fig. 2.6(b). The $\delta_{D_{self}}$ curves exhibits a trend similar to δ_D. A linear regression between $\delta_{D_{self}}$ at 900 K and $\delta(\Delta H_{mixing})$ is performed and displayed in the inset of the Fig. 2.6(b), revealing a linear correlation factor R^2 of 0.97. This indicates that changes in enthalpy of mixing also have a direct impact on the self-diffusion processes.

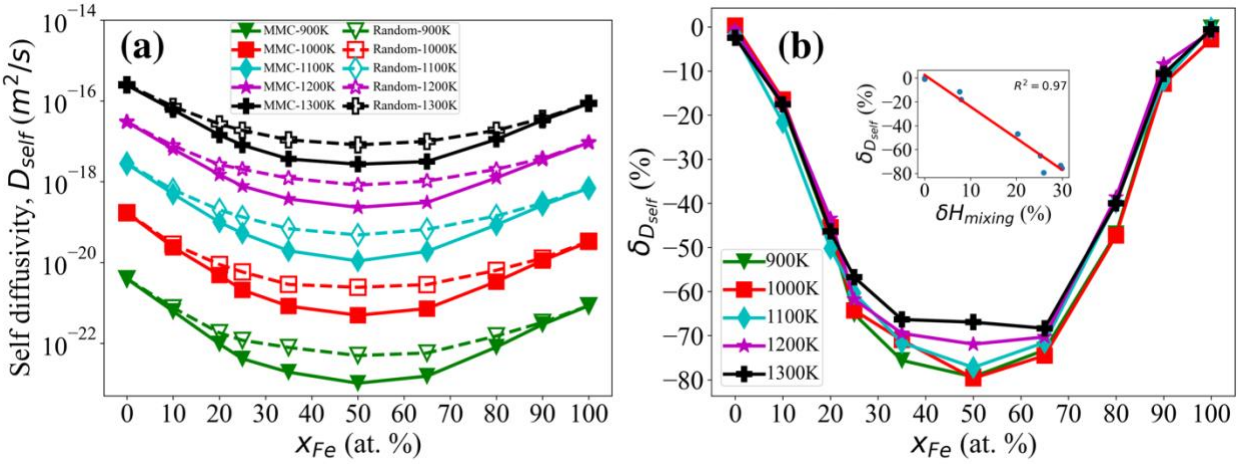

Fig. 2.6 (a) Self-diffusivities as a function of compositions in the Random and MMC structures at temperature from 900 to 1300 K. (b) The percentage changes in self-diffusivity ($\delta_{D_{self}}$) between Random and MMC structures.

2.3.4 Vacancy migration barriers

Figure 2.7 exhibits the distributions of species migration barrier (E_m^{Ni} and E_m^{Fe}) for Random and MMC structures. These migration barriers are analyzed using Gaussian distributions to derive analytical probability distributions, where a larger variance suggests a rougher potential energy landscape (PEL). The mean values of species barrier distributions for both Random and MMC structures at each composition are displayed in the upper right corner of each subfigure. Within each panel of Fig. 2.7, it is evident that the distributions of migration barriers for both Ni and Fe shift toward higher migration barriers in the MMC structures. Figure 2.8(a) details the standard deviation in migration barrier distributions for both the alloy and individual species. MMC structures exhibit larger standard deviation compared to Random structures, signifying a more rugged PEL in the MMC structures, which is likely to cause stronger trapping effects. Specifically, at Ni sites, MMC structures show larger standard deviations than in Random structures for compositions with $x_{Fe} \leqslant 50$ at. %, whereas the opposite trend observed at Fe sites. This distinct behavior underscores that the influence of SROs is chemically oriented and selectively impacts different atomic species, potentially introducing additional chemically-biased diffusion.

Figure 2.8(b) and (c) present the mean values of total and individual species migration barriers ($E^*_{m,all}$, $E^*_{m,Ni}$, $E^*_{m,Fe}$), along with the activation energy (E^{act}) derived from the Arrhenius treatment for Random and MMC structures, respectively. It shows that the maximum $E^*_{m,all}$ occurs at $x_{Fe} \approx 20\%$ in the Random structures, while in MMC structures, it shifts to $x_{Fe} \approx 35\%$. These peaks correspond to the minimal diffusivities observed in Fig. 2.5(a) for both structure groups. The percentage change in the average migration barrier between Random and MMC structures, $\delta E^*_{m,all}$,

is computed and shown in Fig. 2.8(d). Notably, $\delta E^{*}_{m,all}$ exhibits a similar trend to $\delta(\Delta H_{mixing})$, which is further supported by a strong linear regression factor R^2 of 0.89 between $\delta(\Delta H_{mixing})$ and $\delta E^{*}_{m,all}$ in the inset of Fig. 2.8(d).

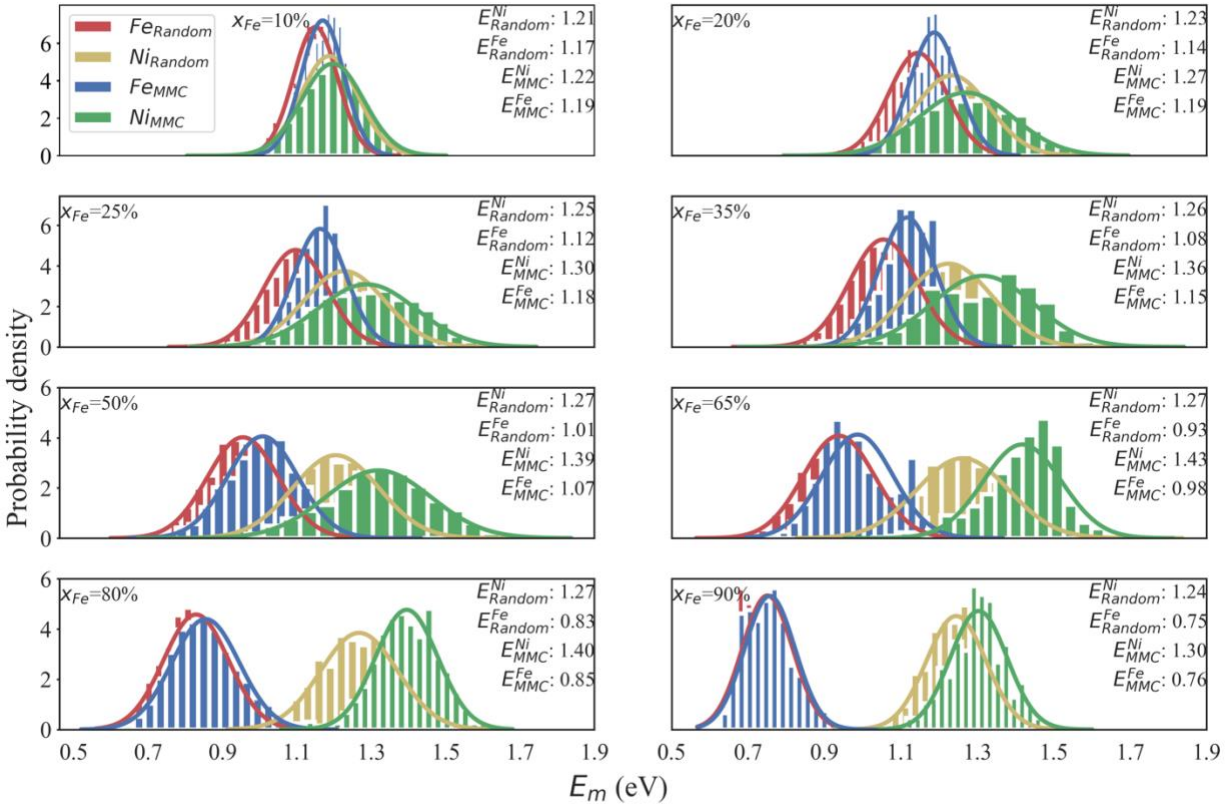

Fig. 2.7 Migration barrier distributions for Ni or Fe sites from NEB calculations for both Random and MMC structures at different compositions.

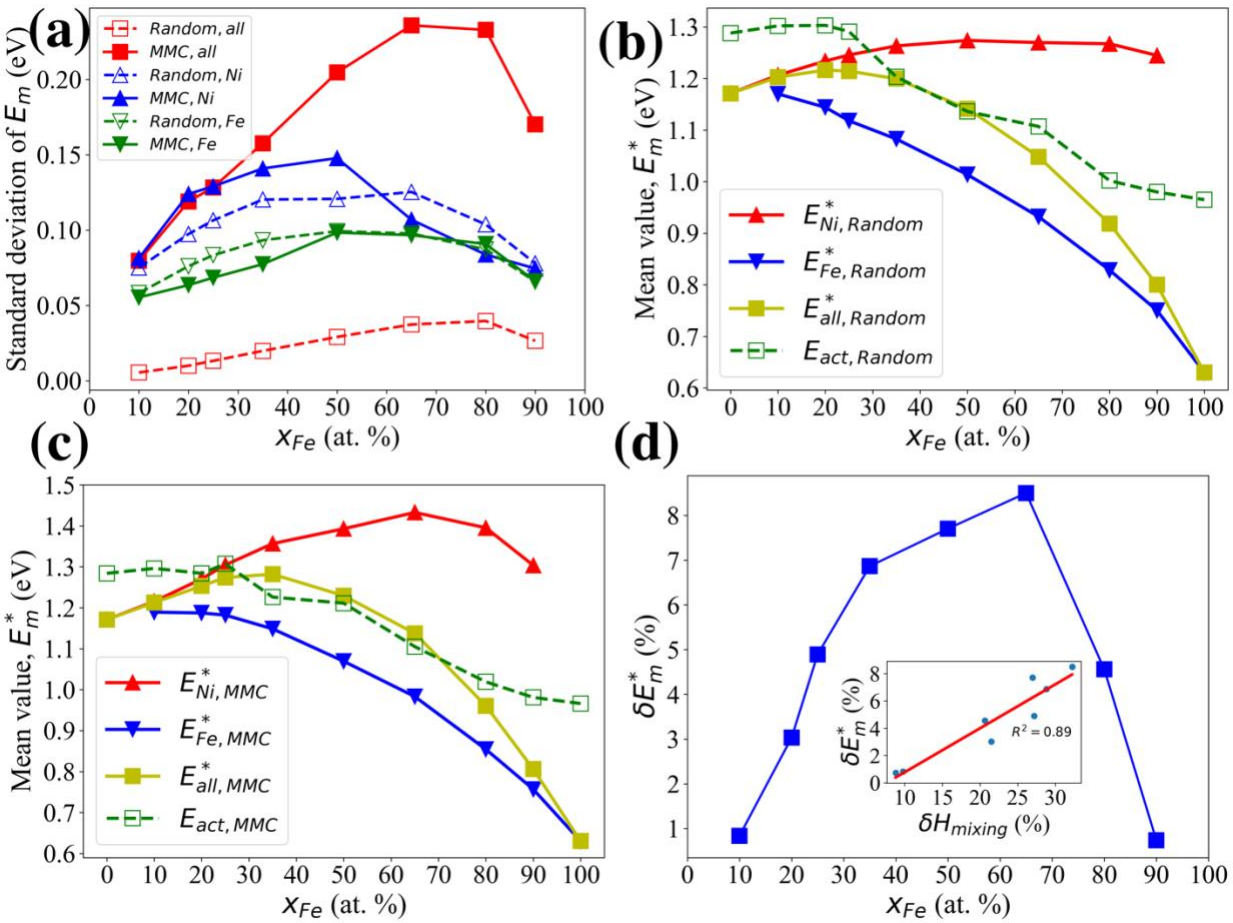

Fig. 2.8(a) The standard deviation of migration barrier distributions for Random and MMC structures; The average migration barriers in (b) Random structures and (c) MMC structures; (d) The percentage change in the average migration barrier, $\delta E^*_{m,all}$, between Random and MMC structures. The inset shows the linear regression between $\delta(\Delta H_{mixing})$ and $\delta E^*_{m,all}$.

2.3.5 Vacancy formation energy

Figure 2.9 presents the vacancy formation energy distributions for individual species (E_f^{Ni} and E_f^{Fe}) in both Random and MMC structures. These distributions are fitted by Gaussian distributions, with mean values displayed in the upper right corner of each subplot. Table 2.1 lists the elemental chemical potentials used in formation energy calculations. Figures 2.10(b) and (c) illustrate the average vacancy formation energy for the alloy and individual species in Random and MMC structures, respectively. In the Random structures, the average vacancy formation energies at Ni and Fe sites are nearly identical, aligning with typical behavior observed in other random alloys [57]. However, the MMC structures show lower average values at Fe sites and higher values at Ni sites, indicating that vacancies are more readily formed at Fe sites compared to Ni sites and an increased relative preference for Fe diffusion. Figure 2.10(a) displays the standard deviation in vacancy formation energy for the Random and MMC structures and no significant difference between system variance were observed. Fig. 2.10(d) shows the percentage change in average formation energy between Random and MMC structures, $\delta E_{f,all}^{*}$. This metrics also shows a trend similar to $\delta(\Delta H_{mixing})$, supported by a strong linear regression factor R^2 of 0.94 between $\delta(\Delta H_{mixing})$ and $\delta E_{f,all}^{*}$, as shown in the inset in Fig. 2.10(d).

Table. 2.1 Chemical potentials of Ni and Fe in both Random and MMC structures at different compositions. All energies are in eV/atom.

x_{Fe} (%)	10	20	25	35	50	65	80	90

Random	μ_{Ni}	-4.45	-4.48	-4.49	-4.53	-4.62	-4.74	-4.90	-5.02
	μ_{Fe}	-4.68	4.56	-4.50	-4.41	-4.29	-4.20	-4.14	-4.12
SRO	μ_{Ni}	-4.45	-4.48	-4.50	-4.56	-4.66	-4.82	-4.98	-5.06
	μ_{Fe}	-4.72	-4.65	-4.60	-4.49	4.33	-4.22	-4.15	-4.12

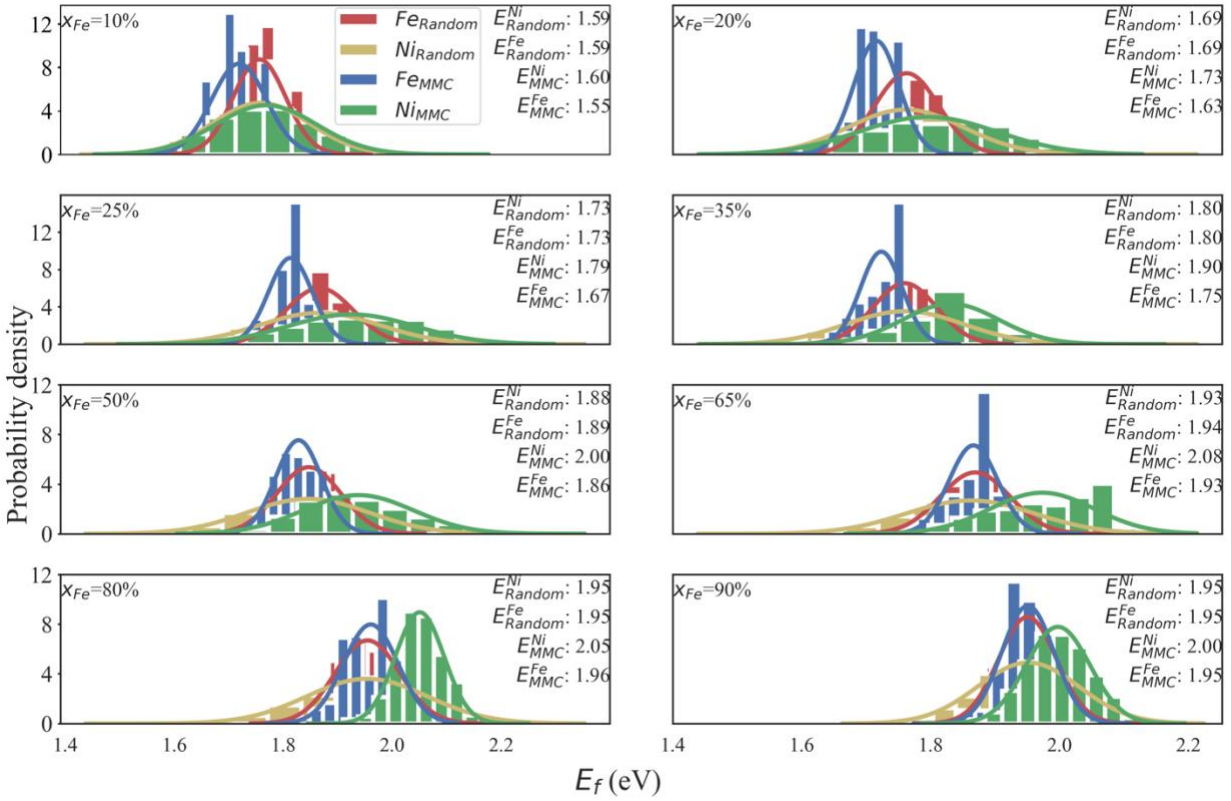

Fig. 2.9 Vacancy formation energy distributions for Ni and Fe sites in both Random and MMC structures at different compositions.

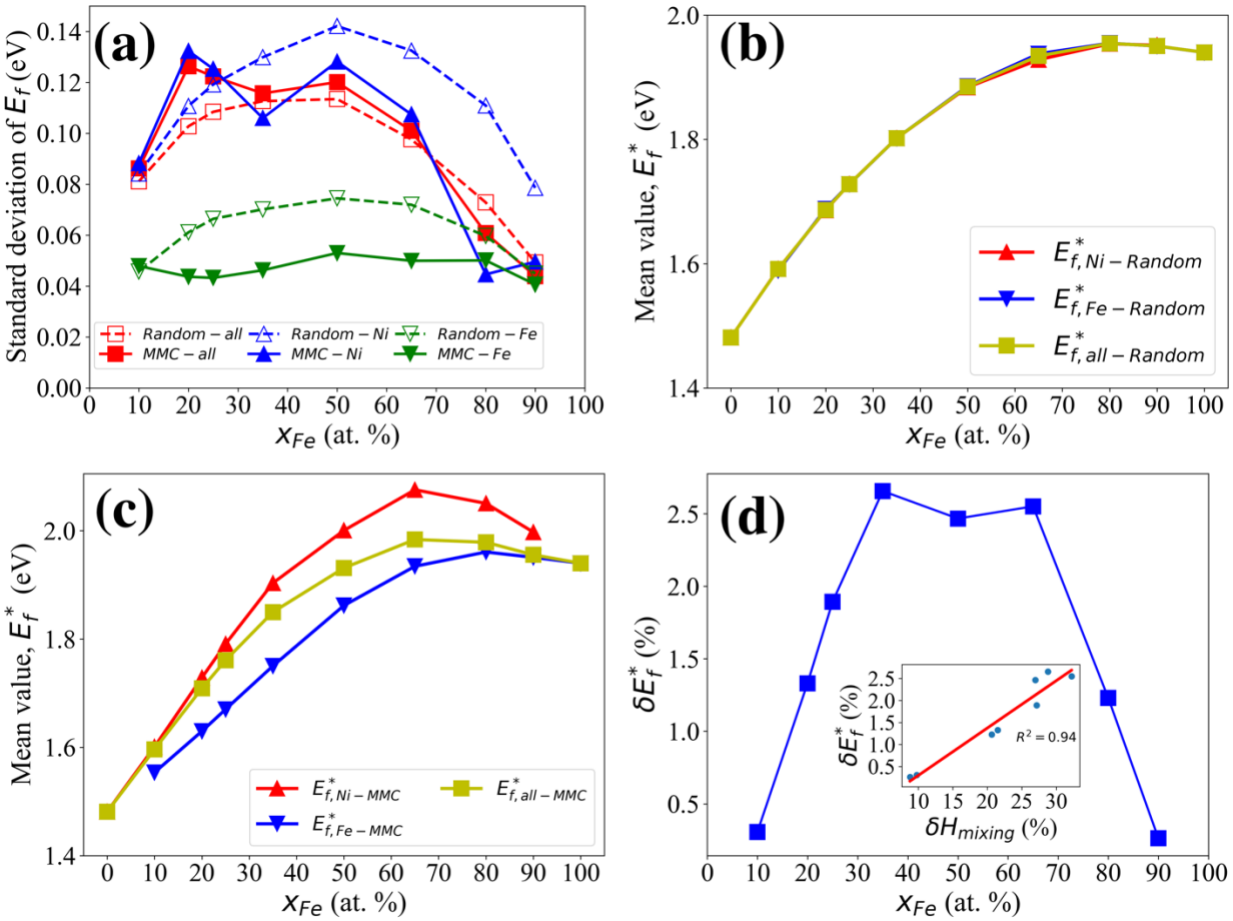

Fig. 2.10 (a) The formation energy variances for the system and individual species in Random and MMC structures at different compositions; The average formation energies in (b) Random structures and (c) MMC structures; (d) The percentage changes in the average formation energies (δE_f^*) between Random and MMC structures. The inset shows the linear regression between $\delta(\Delta H_{mixing})$ and $\delta E^*_{f,all}$.

2.4. Discussion and Conclusion

Through MC+MD optimizations, the potential energy of Ni-Fe alloys is reduced, leading the system to achieve a lower (more negative) enthalpy of mixing (ΔH_{mixing}), which in turn promotes the formation of short-range orders (SROs). The degree of SROs linearly correlates with the percentage changes in ΔH_{mixing} (i.e., $\delta(\Delta H_{mixing})$), as illustrated in Fig. 2.4. These changes subsequently induce a series of alterations in diffusion properties, especially including tracer and self-diffusivities, vacancy migration barrier, and formation energies. Notably, $\delta(\Delta H_{mixing})$, demonstrates negative linear correlations to diffusivities (δ_D or $\delta_{D_{self}}$), and positive linear correlations with percentage changes in average migration barrier ($\delta E^*_{m,all}$) and formation energy ($\delta E^*_{f,all}$). Also, the presence of SROs impacts different species in distinct ways, potentially indicating a tendency towards an enhanced chemically preferential diffusion at Fe sites. Specifically, the vacancy formation energy is decreased at Fe sites while it increases at Ni sites. This differential effect enhances the likelihood of vacancies forming at Fe sites. Moreover, the migration barriers at Fe sites are elevated, which lengthens the time required for vacancies to escape. These combined effects are expected to prolong the residence time of vacancies at Fe sites, thereby lowering the vacancy diffusivities.

In conclusion, this study explores the impacts of SROs on vacancy diffusion in concentrated Ni-Fe alloys by comparing diffusion behaviors between Random and Metropolis Monte Carlo (MMC) optimized structures. Both configurations exhibit a sluggish diffusion phenomenon. However, MMC structures demonstrate a strong sluggish effect than their Random counterparts, with the composition exhibiting the lowest diffusivity shifting from $x_{Fe} \approx 20\%$ to x_{Fe}

≈35%. This shift aligns with the composition that exhibits the highest SRO content. Additionally, the changes in the enthalpy of mixing is likely the driving force behind the development of SROs and the resultant alterations in diffusion properties. The observed slower diffusivities are likely caused by enhanced chemically biased diffusion facilitated by SROs. However, the current study primarily focuses on the average measurement of global diffusion properties. Further detailed investigations are necessary to gain more comprehensive insights into the impact of SROs on sluggish diffusion, particularly at the atomic level. Such studies could provide a deeper understanding of the mechanisms at play and potentially guide the development of alloys with tailored diffusion characteristics.

CHATPTER 3 Machine Learning Based On-The-Fly Kinetic Monte Carlo Simulations of Sluggish Diffusion in Ni-Fe Concentrated Alloys

3.1 Introduction

Computer modeling is a powerful tool for understanding and predicting the defect/solute diffusion in materials. However, there are some challenges for modeling concentrated solid solution alloys (CSAs). For example, some theoretical models such as multi-frequency models [58] can be used for predicting the atomic diffusion. However, these analytical models are typically applicable to dilute alloys [59, 60]. Given the uncountable number of nonequivalent atomic configurations in CSAs, these models may not be easily generalized to concentrated alloys. An alternative tool for studying atomic-level defect diffusion is the molecular dynamics (MD) method [21, 61, 62], in which optimal diffusion paths are automatically chosen based on the local potential energy landscape, provided suitable and accurate interatomic potentials are available. If a simulated trajectory is sufficiently long to ensure the statistics of defect or solute jumps, MD can accurately simulate their diffusion events. However, MD is limited by its inherently short timescale, typically up to a few tens of nanoseconds. As a result, many slow but important diffusion processes (e.g., rare events) that happen at low temperatures of interest may not be captured by MD. The kinetic Monte-Carlo (KMC) method, which implicitly treats atomic vibrations and only considers the kinetics of defects or solutes, can extend the atomic-level simulation to the experimentally accessible timescale [63, 64]. In the conventional rigid-lattice KMC, atoms are restricted to the predefined positions such as fcc lattice sites. The reliability of KMC modeling depends heavily on the accurate description of migration barriers of defect jumps, E_m, which need to be provided to

the model as *a priori* knowledge. However, in CSAs the defect migration barrier changes from site to site due to the varying local atomic environment. Therefore, it is nearly impossible to determine all the migration barriers beforehand and provide the complete event table to KMC. On the other hand, it is possible to use the off-lattice KMC [65] such as the kinetic activation-relaxation technique (k-ART) [66, 67] to determine the migration barriers on-the-fly in CSAs, as demonstrated by Osetsky et al. [16]. However, the on-the-fly determination of migration barriers using the nudged elastic band (NEB) method [25, 68, 69] or the activation relaxation technique nouveau (ARTn) [70] entails a high computational cost.

Recently, machine learning techniques such as the artificial neural networks (ANNs) have attracted researchers' significant interests for studying various materials science problems [27-31]. Machine learning is a powerful tool for analyzing high-dimensional and complex problems to identify the underlying correlations with some material features or descriptors, if sufficient and accurate training data are available. For the defect or solute diffusion in CSAs that is the focus of this work, it is envisioned that one may develop an advanced regression algorithm or machine learning model for predicting the migration barriers in CSAs based on the local atomic configurations (LACs) around a defect or solute, because its migration barrier strongly depends on its neighboring chemical species as well as its jumping pathway. After such a model is established, one may replace the computationally expensive on-the-fly calculation of migration barriers in KMC with such a more computationally efficient model.

In this work, we aim to develop an ANN model to predict vacancy migration barriers for arbitrary atomic configurations in CSAs and couple it with the conventional KMC to study the

vacancy diffusion at a wide range of alloy compositions and temperatures. The concentrated fcc $Ni_{1-x}Fe_x$ (x = 0 – 1) alloy system is used as a model system because it has been shown to have strongest sluggish diffusion at the percolation threshold of $x_{Fe} \approx 0.2$ [16]. Two types of atomic configurations are considered: fully random distribution of alloying elements (a chemically disordered structure) as in previous MD studies [16, 21], and the Metropolis Monte-Carlo (MMC) optimized structures that encompass local SROs as characterized by the Warren-Cowley SRO parameter [55]. A finite number of NEB calculations are conducted to obtain necessary training data for the ANN-based machine learning model. The trained ANN model is then coupled with KMC to predict the vacancy migration barrier on-the-fly and calculate the effective vacancy diffusivity in this alloy system. A composition- and temperature-dependent jump attempt frequency model, rather than a fixed frequency that is commonly used in many KMC studies [16, 71], is also developed. The calibrated ANN-KMC model can predict similar vacancy diffusivities as independent results by MD at high temperatures and by temperature accelerated dynamics (TAD) [72] at moderate temperatures, demonstrating that the approach can achieve very high computational efficiency without compromising its accuracy. The approach thus enables us to study defect diffusion in CSAs at low temperatures that may not be accessible by other atomistic simulation methods.

3.2 Methods

A number of complementary simulation methods are used in this work: NEB, ANN based machine learning, KMC, MMC, MD, and TAD. For the NEB, MMC, MD, and TAD, the Ni-Fe

interatomic potential developed by Bonny et al. [52] is used. These methods are briefly described as follows.

3.2.1 Alloy structures and NEB database of vacancy migration barriers

As mentioned earlier, two groups of atomic configurations for the $Ni_{1-x}Fe_x$ ($x = 0 – 1$) fcc alloys are considered: random distribution of alloying elements and MMC-optimized structures that contain SROs. In each group, eight compositions are studied: x_{Fe} = 10%, 20%, 25%, 35%, 50%, 65%, 80%, 90%. To create the first group (denoted as the "Random" group), Ni and Fe atoms are randomly mixed in a $10a_0 \times 10a_0 \times 10a_0$ fcc lattice containing 4,000 atoms at each composition. To create the second group (denoted as "MMC" group), the hybrid MC+MD method implemented in the LAMMPS package [51] is applied to optimize each generated random structure. During the optimization, a randomly selected Ni is swapped with a randomly selected Fe atom, and the acceptance probability of this swap depends on the change of the system potential energy. Following every swap, a short (0.01 ps or 5 timesteps) MD simulation is performed in an NVT (constant number of atoms, volume, and temperature) ensemble at 300 K to relax the system. This procedure is repeated for a total of 400,000 MMC steps. The resulting alloy structures in the MMC group have much lower potential energies than the counterparts in the Random group and an example is shown in Fig. 3.1(a). The MMC-optimized structures exhibit some extent of short-range orders. To quantify the degree of ordering, the Warren-Cowley SRO parameter [55] is calculated up to four nearest neighboring (nn) shells for each composition, as shown in Fig. 3.1(b). Clearly, the Random structures have no discernible ordering because the SRO values of all shells are nearly zero, while the MMC structures have distinctive ordering, as indicated by the large

positive (clustering of Ni-Ni or Fe-Fe pairs) or negative (clustering of Ni-Fe pairs) SRO values in the second and third shells.

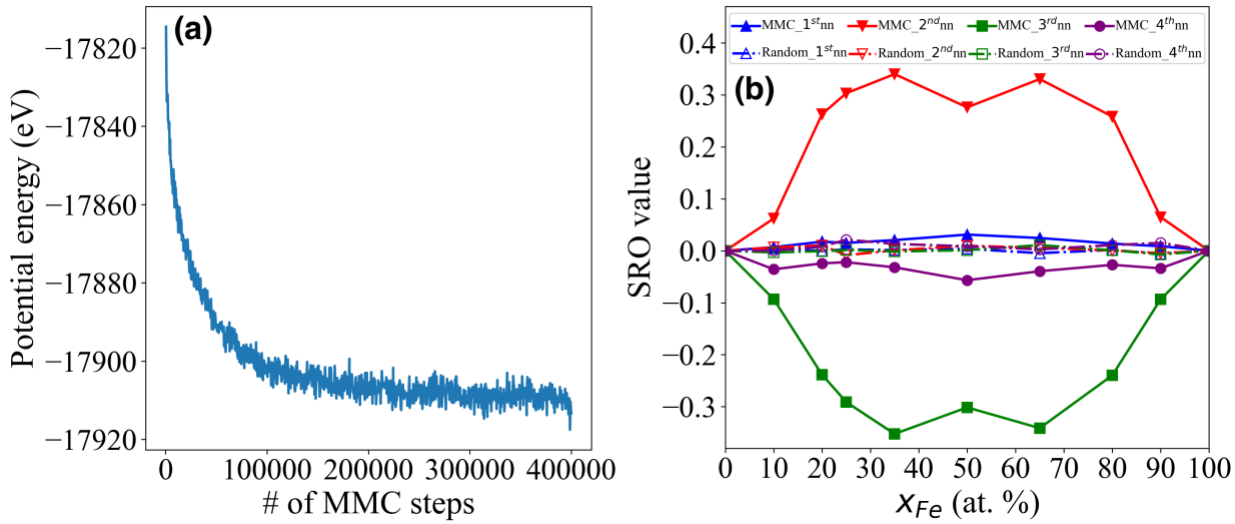

Fig. 3.1 (a) Potential energy change during a hybrid MC + MD simulation (denoted as MMC optimization) in an $Ni_{80}Fe_{20}$ alloy that has an initially random atomic configuration. (b) Warren-Cowley SRO values up to the 4th nn for both Random and MMC structures at different compositions.

After both Random and MMC structures are created, the NEB method [25, 69] implemented in LAMMPS is used to calculate the vacancy migration barriers (E_m) for different atomic environments. At each Ni-Fe composition, a vacancy is created at every lattice site, one at a time. At each vacancy site, the vacancy migration path is randomly chosen between the vacancy and one of its twelve 1st nn atoms and the corresponding migration barrier (E_m) is calculated. This results in 4,000 barriers at each composition and 32,000 barriers in each structural group (because

there are eight compositions in each group). In all NEB calculations, the number of NEB images (including the initial and final states) is 13 and the spring constant is set to 1.0 eV/Å^2.

3.2.2 LAC definition and ANN model

In an $Ni_{1-x}Fe_x$ fcc alloy, a vacancy can diffuse to one of its 12 nearest neighbor sites, as schematically illustrated in Fig. 3.2(a). The vacancy migration barrier of each pathway depends on not only the atom type at the neighboring site along that pathway, but also the local atomic configuration (LAC) around that neighboring site. Therefore, a well-defined LAC is a premise for an ANN model that can accurately predict the vacancy migration barrier (E_m). Figure 3.2(b) schematically shows two possible vacancy migration pathways between the vacancy "V" and atom "$A_{i\,=\,1,\,2}$". The LAC of an atom "A_i" includes all atoms as well as the vacancy site within a cutoff radius (large dash circle) from A_i. In the relaxed $Ni_{1-x}Fe_x$ alloys, atoms can have small displacements from the perfect fcc lattice sites due to the mixing effect. Although the NEB calculations include all local chemistry and lattice distortion, the migration events in the conventional KMC are still described in a rigid lattice framework. To keep this advantageous simplicity of the KMC model, the small off-site displacement of an atom in the equilibrium state is neglected in our ANN model if it stays within the original Wigner-Seitz cell [73] (see Fig. 3.2(b)). Therefore, all sites in the same nearest neighboring shell have the same distance from the central atom/site. The description of a LAC is represented by a string of integers for each neighboring shell in consideration, e.g., 1 for Ni, 2 for Fe and 0 for vacancy. Four neighboring shells are taken

into consideration for constructing LAC vectors. A closer shell is endowed with a higher weight. For example, the first two neighboring shells around a moving atom "A_i" can be defined as,

$$1nn\ LAC = W_{1nn}[1,0,1,2,1,2,1,1,1,2,1,1,1],$$

$$2nn\ LAC = W_{2nn}[1,2,2,2,1,1],$$

where W_{1nn}, W_{2nn} are the weights for 1st and 2nd neighboring shells, respectively, and $W_{1nn} > W_{2nn}$.

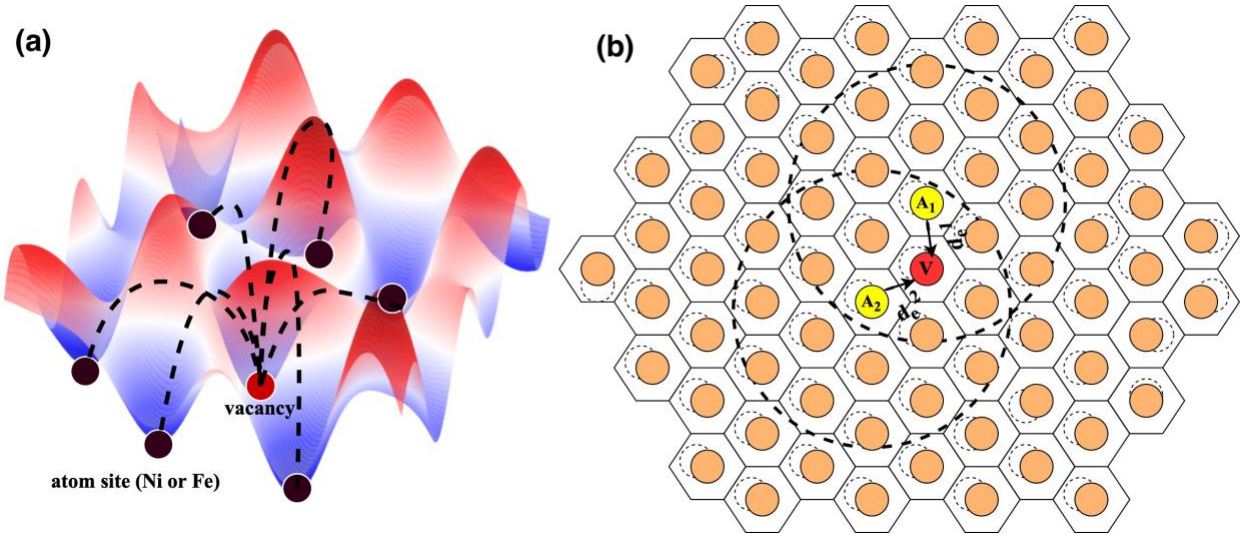

Fig. 3.2 (a) Schematic illustration of vacancy migration pathways in the potential energy landscape. (b) 2D schematic illustration of two possible vacancy migration pathways (from "V" to "$A_{i=1,2}$") in a rigid lattice approximation of a distorted crystal structure. Hexagons represent Wigner-Seitz cells, within which small dash circles denote real equilibrium positions of atoms and filled circles are rigid lattice sites. Here "A_i" represents the moving atom (Ni or Fe), "V" is the vacancy site and

"d_e^i" represents the atom movement direction of the pathway. The large dash circle around each A_i shows the cutoff radius within which all neighboring sites are included in constructing its LAC.

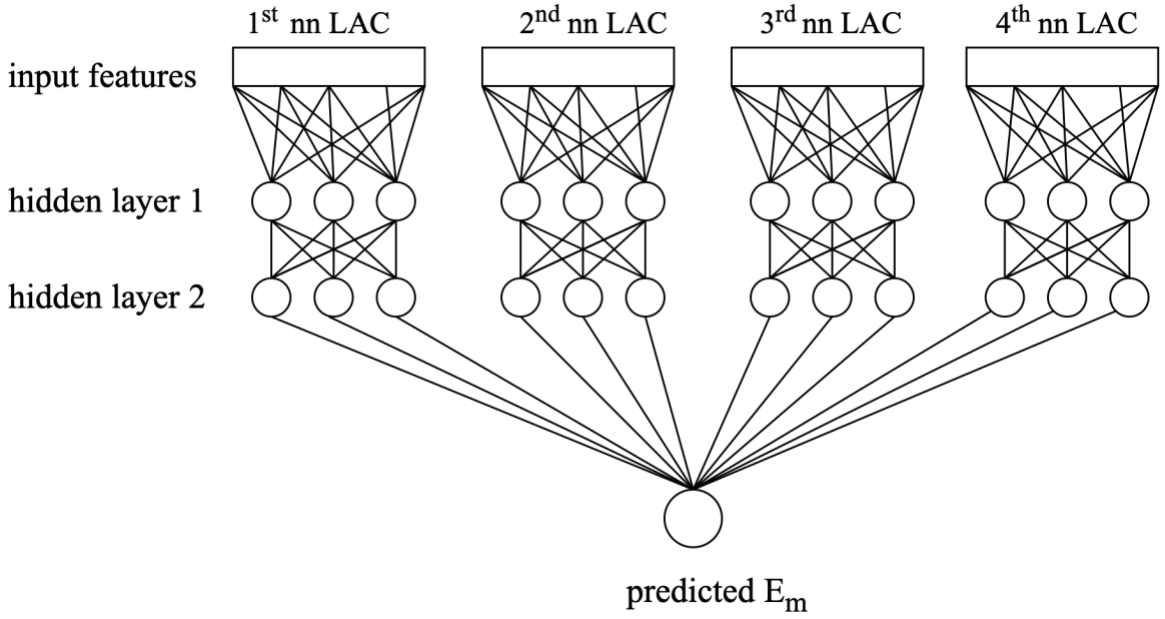

Fig. 3.3 Schematic of the ANN architecture. There are three neurons (solid circles) in the hidden layers 1 and 2 for each input shell vector to integrate all information to predict E_m values.

The ANN architecture is shown in Fig. 3.3 The training logic is: (i) The LAC input features from the 1st nn to 4th nn shells are separately connected to the first hidden layer; (ii) The first hidden layer is implemented to integrate the information for each shell; (iii) The second hidden layer desegregate the information passed by the first hidden layer to give the predicted E_m. The number of neurons and layers are determined empirically by trial-and-error. The training algorithm uses the Levenberg-Marquardt method [74], a hybrid technique that uses both Gauss-Newton update

and gradient descent to converge to an optimal solution, and its superior performance for similar applications has been demonstrated [75, 76].

3.2.3 ANN-KMC modeling

The trained ANN model is coupled with the rigid-lattice KMC using the KMCLib package [77] to simulate the vacancy diffusion in $Ni_{1-x}Fe_x$ alloys for both MMC and Random groups. In the lattice KMC model, atom diffusion is solely driven by the thermally activated migration jumps that a single vacancy takes. The rate of a vacancy jump event from an initial position *i* to one of its neighboring sites *j* is expressed by the standard transition state theory,

$$\Gamma_{ij} = \nu_o \exp\left(-\frac{E_{m,ij}}{k_B T}\right), \tag{3.1}$$

where ν_o is the jump attempt frequency, k_B is the Boltzmann's constant, T is the absolute temperature, and $E_{m,ij}$ is the vacancy migration barrier from site *i* to *j*. At each KMC step, the ANN model predicts $E_{m,ij}$ for all 12 possible jumping pathways on-the-fly with a negligible computational cost. A random number r_1 in the range of (0, 1] will pick a path *s* among 12 possible pathways following,

$$\sum_{j=1}^{s} \Gamma_{ij} > r_1 \cdot \sum_{j=1}^{12} \Gamma_{ij}, \tag{3.2}$$

and the system evolves into a new state by the path *s*. The time elapsed is calculated by another random r_2 in the range of (0, 1] according to the residence time algorithm [64],

$$\Delta t = -\frac{\ln(r_2)}{\sum_{j=1}^{12} \Gamma_{ij}}. \tag{3.3}$$

In this work, 10,000 – 30,000 KMC steps are conducted for each simulation. The diffusion coefficient is calculated using the Einstein relation [78],

$$D = \frac{\Delta r_s^2(t)}{6t} \tag{3.4}$$

where $\Delta r_s^2(t)$ is the sum of the atomic square displacements (ASDs) of all atoms (for total diffusivity) or individual type of atoms (for partial diffusivity) in 3D, and *t* is the simulation time. To obtain reliable statistics, six independent simulations are conducted at each condition and the average diffusivities are reported in this work.

Regarding the jump attempt frequency (v_o), it was typically set to a fixed value close to the phonon frequency ($10^{12} \sim 10^{13}$ s^{-1}) in many previous KMC simulations [79, 80]. However, it could be affected by both temperature and composition. For example, in some studies it was found to be two orders of magnitude higher or lower than the phonon frequency [81, 82]. In this work, a temperature- and composition-dependent v_o is developed because a constant v_o leads to unsatisfactory results. The details are discussed in the Results section.

3.2.4. MD simulations

To compare with ANN-KMC results at high temperatures, MD simulations of vacancy diffusion in the $Ni_{1-x}Fe_x$ alloys are conducted at 900 – 1300 K using LAMMPS [51]. The structures in both Random and MMC groups are studied. The effects of atomic configurations and other material properties on the vacancy diffusivities will be presented in detail elsewhere. Here only the calculated diffusivities are reported, which are used to validate ANN-KMC results. The MD simulations are conducted in an NPT ensemble (constant number of atoms, pressure, and temperature). The Nose-Hoover thermostat and barostat [53] are used to control the system temperature and pressure (at zero bar), respectively. The time step is set to 2 fs. The simulations at lower temperatures, such as 900 K and 1000 K, are conducted up to 100 ns each for ten independent simulations to improve the statistics at each condition; Whereas the simulations at higher temperatures (> 1000 K), which have faster diffusivities, are completed over 40 ns each for six independent simulations. Same as in KMC, the total and partial diffusion coefficients are calculated from the atomic square displacements (Eq. 3.4).

3.2.5. TAD simulations

The vacancy diffusivities calculated by MD are limited to high temperatures. In order to obtain diffusivities at a moderate temperature (800 K) for further validating the KMC results, the TAD method [72] implemented in LAMMPS is used. TAD is one type of accelerated molecular dynamics (AMD) methods [83, 84], and has the ability to reach much longer timescale than MD but still maintains the full atomic fidelity as MD [85, 86]. TAD conducts basin-constrained MD at

a high temperature to accelerate the search of many candidate transition events from the current state (basin). Unlike in the rigid-lattice KMC, TAD does not require *a priori* knowledge of these candidate transition paths or mechanisms. Once a candidate transition event is detected, the NEB method is used to calculate the transition barrier on-the-fly. The system is then brought back to the current basin and new searches continue, until a stopping criterion is met. For a candidate transition event j, the time at the low temperature of interest ($t_{Low,j}$) is extrapolated from its high-temperature MD time ($t_{High,j}$) based on the transition state theory,

$$t_{Low,j} = t_{High,j} exp\left[E_{m,j}\left(\frac{1}{k_B T_{Low}} - \frac{1}{k_B T_{High}}\right)\right], \quad (3.5)$$

where $E_{m,j}$ is the transition barrier obtained by NEB (e.g., the vacancy migration barrier in this work) along the path j, T_{Low} is the low temperature of interest, and T_{High} is the high temperature for accelerating the transition. Among the detected candidate events after the stopping criterion is met, the event with the shortest time at T_{Low} is accepted. Therefore, the candidate events that should not happen at T_{Low} are filtered out. Then the system advances to a new basin and the process repeats. In this work, T_{High} and T_{Low} are set to 1600 K and 800 K, respectively. The simulation system contains 864 atoms of different compositions in a $6a_0 \times 6a_0 \times 6a_0$ fcc lattice. The time step for the high-temperature MD is 2 fs. A transition is defined when the displacement of any atom is greater than 0.6 Å and the transition is checked every 50 steps. The desired confidence level for stopping criterion is set to δ=0.05. The minimum pre-exponential factor is set to $\nu_{min} = 2\times10^{12}$ s^{-1} (or t_{max} = 0.5 ps). The simulation time is over 60 ns at T_{High}, which results in μs-scale time at T_{Low}. Same as in KMC and MD, the atomic square displacements (Eq. 3.4) are used to calculate the diffusion

coefficients. In addition, the transition barriers of all accepted events during the vacancy diffusion are recorded by TAD, which will be presented in the Results section.

3.3 Results

3.3.1 ANN model for vacancy migration barriers

To train the ANN model of vacancy migration barriers (E_m), the two groups (Random and MMC) of databases mentioned above are not identically utilized. In this work, the barriers in the MMC group, which contain some SROs, are used to train the ANN model. Specifically, the data in the MMC group are split to serve the functions of training, validation, and testing with a ratio of 70%:15%:15%. Once an ANN model has been adequately trained, e.g., obtained a satisfactory performance on the testing set, the data in the Random group, equivalent to unseen data to the trained ANN model, are tested to verify the transferability of the ANN model. The trained ANN model is accepted when it also reaches satisfactory performances on the data in the Random group. Figure 3.4(a) shows a good correlation between ANN predicted and NEB calculated E_m on the MMC group dataset. It is adequately accurate with the average prediction error within 0.040 eV, and R^2 of ~95%. Figure 3.4(b) presents an average error of 0.043 eV and R^2 of 93% on the Random group dataset. Some outliers do exist, possibly related to the rigid lattice approximation. However, the accuracy of the KMC model is not affected by these extreme and rare cases because they make little difference to the statistics.

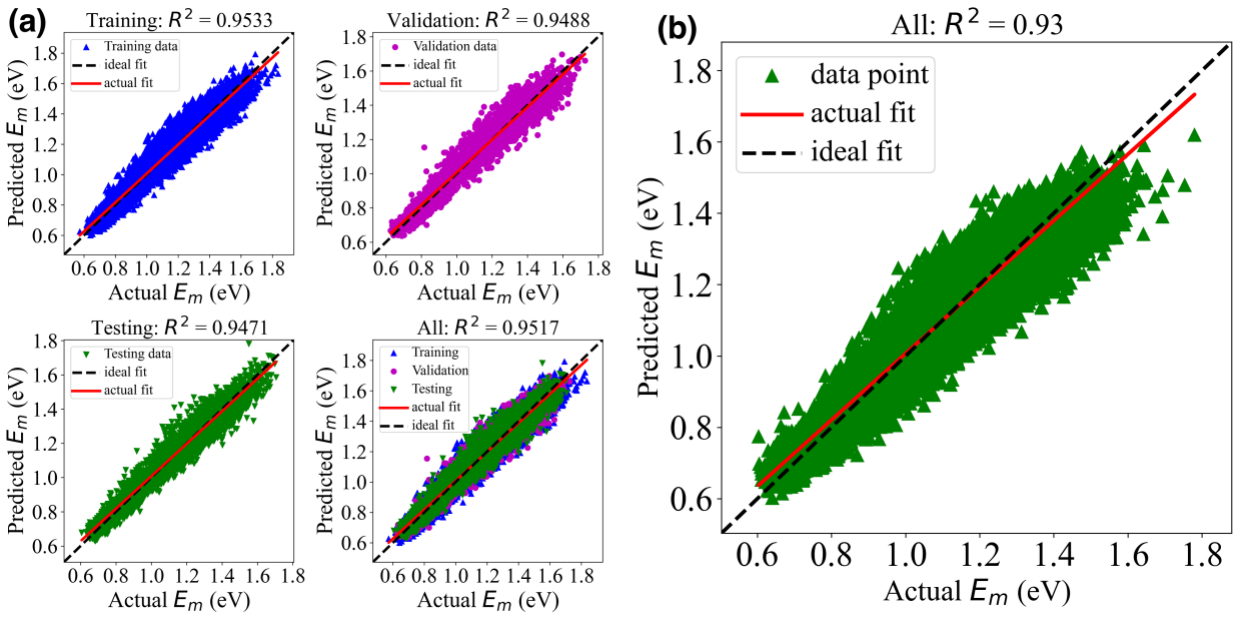

Fig. 3.4 (a) The trained ANN model of vacancy migration barriers that only uses the MMC group's data. Four plots indicate regression accuracies on training, validation, testing, and overall dataset. (b) The performance of the trained ANN model in (a) on the unseen data from the Random group.

3.3.2 ANN-KMC results of the MMC group

The ANN model developed in the previous section is coupled with KMC to calculate the vacancy diffusivities in the MMC-group structures that contain SROs. The first test is using a fixed jump attempt frequency, ν_o = 10^{13} s^{-1}, as in many previous studies [16, 71]. The calculated diffusion coefficients are compared with the MD results as a function of alloy composition at 1300 K, as shown in Fig. 3.5(a). Clearly, there is a large discrepancy between ANN-KMC and MD results when the Fe concentration x_{Fe} < 80%. The most distinctive difference is the pure Ni, which is independent of the ANN model because it only has a single vacancy migration barrier. Therefore,

the fixed v_o value is likely the reason that induces such discrepancies. To solve this problem, in this work v_o is treated as both composition- and temperature-dependent. According to Kong and Lewis [87], the temperature-dependent attempt frequency has the form,

$$v_o = \frac{k_B T}{h} \exp\left(\frac{-\Delta F_{vib}}{k_B T}\right), \tag{3.6}$$

where h is the Planck's constant, ΔF_{vib} is the vibrational free energy difference between the transition state and the initial state. For simplicity, the exponential term in Eq. (3.6) is replaced by a polynomial function of composition,

$$v_o = \frac{k_B T}{h} f(x_{Fe}), \tag{3.7}$$

where $f(x_{Fe})$ will be calibrated with the MD diffusivity data, as discussed below.

To determine $f(x_{Fe})$, the v_o values are obtained by fitting to the MD data at 1300 K for all compositions, as shown in Fig. 3.5(b). At this temperature, the coefficient $\frac{k_B T}{h}$ = 2.71×10^{13} s^{-1}, and a 4th order polynomial function is used to fit $f(x_{Fe})$,

$$f(x_{Fe} = x) = 1.764 - 8.92 \times 10^{-3}x + 3.96 \times 10^{-5}x^2 - 4.16 \times 10^{-6}x^3 + 3.2 \times 10^{-8}x^4, \tag{3.8}$$

To determine v_o for other temperatures *T*, Eqs. (3.7-8) are directly used and no other fitting is needed. Essentially this scales the v_o values at 1300 K with a factor of *T*/1300, i.e., $v_{o,T}$ = $\frac{T}{1300} v_{o,1300K}$ for the corresponding compositions. It should be noted that the MD data at x_{Fe} = 25% (i.e., $Ni_{75}Fe_{25}$) is not included in the fitting but $f(x_{Fe})$ still works well for this composition. Also

noted that although $f(x_{Fe})$ is only fitted to the MD data of the MMC group at 1300 K, it works well at other temperatures for both MMC and Random groups, as shown below.

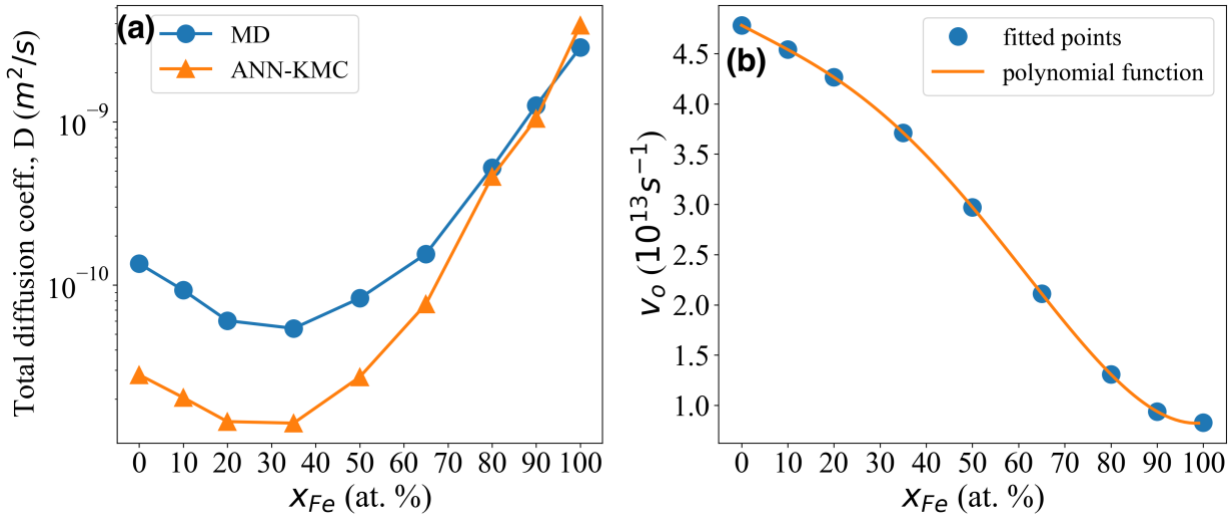

Fig. 3.5 (a) Total diffusion coefficients obtained from ANN-KMC at 1300 K using a constant jump attempt frequency, v_o = 10^{13} s^{-1}, which show large discrepancies with the MD results at x_{Fe} < 80%. (b) The fitted v_o values (filled circles) against the MD data at 1300 K. The solid line shows the fitted 4th order polynomial function (Eqs. (3.7 – 8)).

Figure 3.5(b) shows that v_o decreases monotonically with increasing Fe concentration. It also shows that v_o in pure Ni is about 5 times higher than in pure Fe, even though they both have an fcc structure in this work, consistent with many previous studies that it is material dependent [87]. After the composition-dependent v_o is calibrated at 1300 K, it is used in ANN-KMC to predict the vacancy diffusivities at lower temperatures. Figure 3.6(a) shows a complete comparison of vacancy diffusivities obtained via ANN-KMC and MD simulations for temperatures from 900

K to 1300 K. The error bar of each MD data point represents the standard deviation from 6 – 10 independent simulations. Each diffusivity value from ANN-KMC is averaged from 6 independent simulations, and its error bar is ignored due to very small variance. Clearly, the ANN-KMC predicts nearly identical vacancy diffusivities as the MD results in a wide range of compositions and temperatures, even though v_o is merely fitted to the MD data at 1300 K. There are some discrepancies under some conditions, primarily at low temperatures (e.g., $Ni_{65}Fe_{35}$ at 900 K). This is likely due to the insufficient statistics in MD simulations because the short timescale in MD poses an inherent challenge for studying the slow diffusion kinetics at low temperatures. At all temperatures, the vacancy diffusivity first decreases then increases with the increasing Fe concentration, consistent with Osetsky et al.'s work [16]. The two end points (i.e., pure Ni and pure Fe) at each temperature indicate that Fe is a faster diffuser than Ni. The minimum diffusivity occurs around $x_{Fe} = 25{\sim}35\%$ for the structures of the MMC group in this work, slightly different from ~20% (which is the Fe percolation threshold) in Osetsky et al.'s work [16].

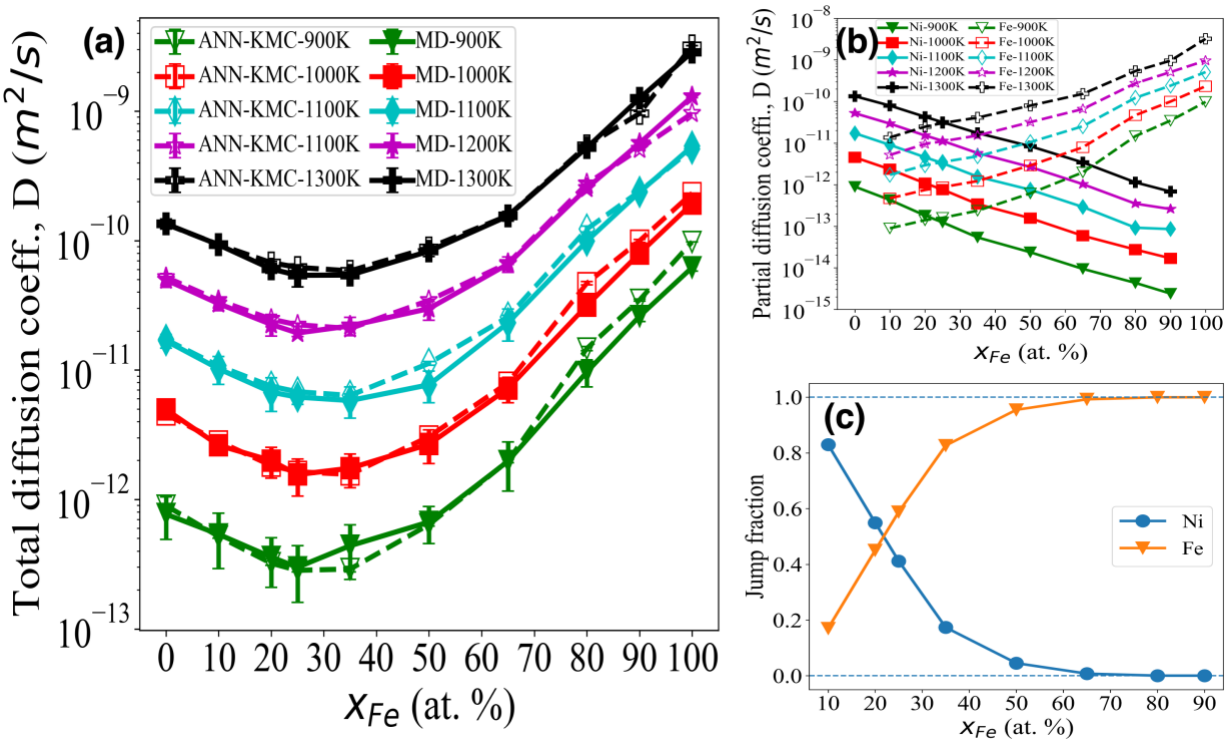

Fig. 3.6 (a) Total vacancy diffusivities as a function of composition in the MMC-optimized $Ni_{1-x}Fe_x$ model alloys calculated from ANN-KMC and MD simulations at 900 – 1300 K. Note only the MD data at 1300 K are used to calibrate the v_o in ANN-KMC. Solid lines with filled symbols are MD data, and dashed lines with unfilled symbols are ANN-KMC data. Each error bar represents the standard deviation of 6 – 10 MD results. The error bars in ANN-KMC results are ignored due to the negligible variances. (b) Partial diffusivities as a function of alloy composition from ANN-KMC results at different temperatures. (c) Jump fractions of Ni and Fe as a function of composition at 1200 K.

Figure 3.6(b) shows the partial diffusion coefficients of Ni and Fe from the ANN-KMC modeling. At all temperatures, Ni diffusivity (D_{Ni}^{MMC}) decreases while Fe diffusivity (D_{Fe}^{MMC}) increases with increasing Fe concentration, because Fe is a faster diffuser. The intersection between D_{Ni}^{MMC} and D_{Fe}^{MMC} is located at x_{Fe} = 20 ~ 25% and slightly shifts rightward (to higher x_{Fe}) with the increasing temperature. This crossover Fe concentration is slightly lower than that for the minimal total diffusivity in Fig. 3.6(a), which is in the range of $x_{Fe} = 25{\sim}35\%$. At x_{Fe} = 20% (in the $Ni_{80}Fe_{20}$ alloy), the ratio of D_{Fe}^{MMC} / D_{Ni}^{MMC} is 0.79, 0.72, 0.65, 0.58, 0.55 for 900 ~ 1300 K, respectively. This indicates that the contribution from the faster diffuser Fe increases as the temperature decreases. Figure 3.6(c) shows the fractions of vacancy jump types (i.e., a vacancy jump via Ni or Fe atom) as a function of Fe concentration at 1200 K. It can be seen that the dominant vacancy jump type changes from Ni to Fe in the range of x_{Fe} = 20 ~ 25% (about x_{Fe}= 22%), similar to the crossover concentration for the partial diffusivities in Fig. 3.6(b). After the crossover, the jump via Fe becomes more and more dominant. When x_{Fe} > 65%, the Fe jumps dominate completely and there are almost no Ni jumps.

The excellent agreement between ANN-KMC and MD results at 900 ~ 1300 K suggests that ANN-KMC may be used to predict the diffusivities at low temperatures. However, as mentioned earlier the events that happen at high temperatures in MD may not happen at the lower temperatures of interest. Therefore, to further validate the ANN-KMC model, the TAD method is used to calculate the total vacancy diffusivities in the $Ni_{1-x}Fe_x$ alloy at a moderate temperature, T = 800 K. The comparison between TAD and ANN-KMC results at different compositions at 800 K is shown in Fig. 3.7(a). Note that the TAD results are completely independent (blind) to the ANN-KMC model because the system size in TAD is different from that in ANN-KMC and the

simulated structures are also different. Nevertheless, the agreement between ANN-KMC and TAD results is reasonably good. Even though there are slight discrepancies, the error bars (standard deviations) in TAD results overlap with ANN-KMC results at many compositions. Both TAD and ANN-KMC give similar minimal diffusivities at $x_{Fe} = 20 \sim 25\%$, which is slightly different from the minimum diffusivities occurring at $x_{Fe} = 25 \sim 35\%$ at higher temperatures (900 – 1300 K) shown in Fig. 3.6(a). Since ANN-KMC results have good agreement with MD and TAD results at both high and moderate temperatures, the ANN-KMC is used to predict the total vacancy diffusivities at a low temperature (T = 500 K) that is inaccessible to MD, as shown in Fig. 3.7(a). Again, the minimal diffusivity happens at $x_{Fe} = 20 \sim 25\%$, similar as at T = 800 K. It should be noted that the sluggish diffusion effect at this composition is more pronounced than at high temperatures (Fig. 3.6(a)) because the minimum vacancy diffusivity at 500 K is about one and five orders of magnitude than the diffusivities in pure Ni and Fe, respectively.

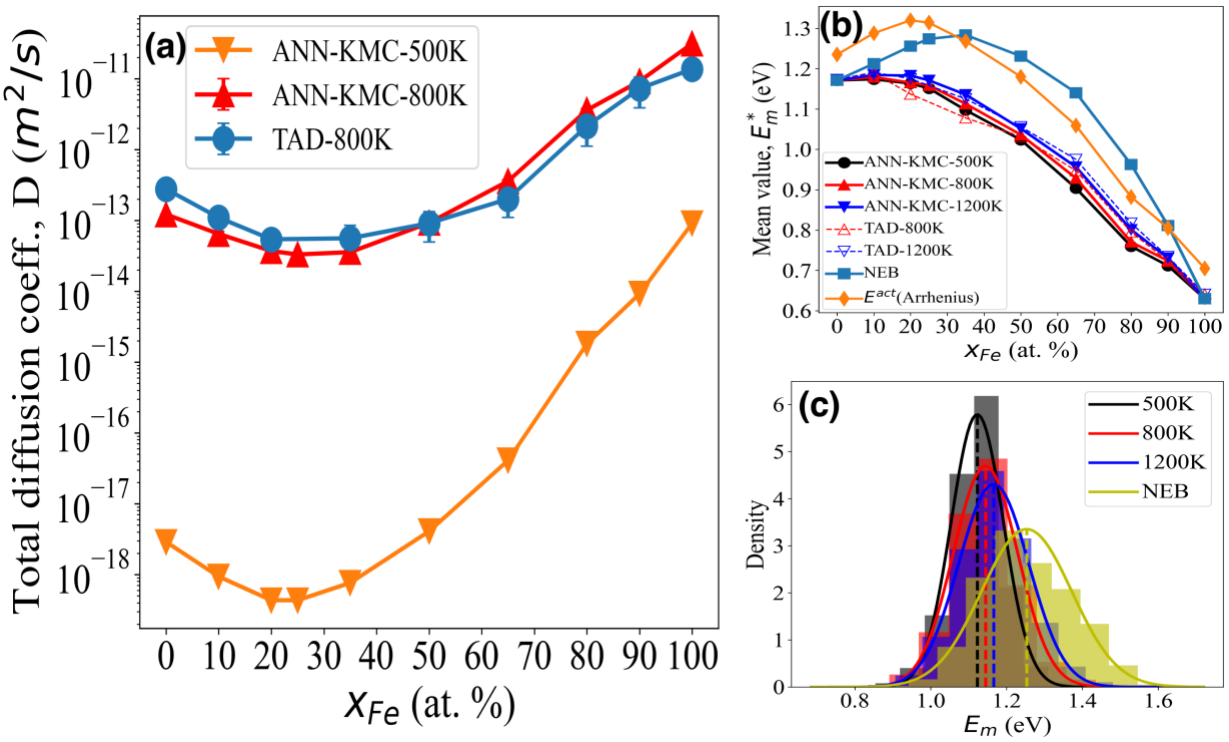

Fig. 3.7 (a) Comparison of the total diffusivities in the MMC group alloys obtained by TAD and ANN-KMC at 800K as a function of composition. The ANN-KMC results at a low temperature (500 K) that is unreachable to MD is also shown. (b) Two methods for estimating the effective vacancy migration energies at different compositions: Arrhenius fitting of ANN-KMC diffusivities at 500, 800 – 1300 K; The average of the migration barriers from executed (accepted) jumps during ANN-KMC and TAD simulations. For comparison, the average of the static NEB barriers at 0 K is also shown at each composition. (c) The migration barrier distributions from static NEB calculations at 0 K, and the ANN-KMC simulations at 500K, 800K, and 1200K for the $Ni_{80}Fe_{20}$ alloy.

Here, two methods are used to present the effective migration energies. The first is the activation energy extracted from an Arrhenius-type treatment of ANN-KMC diffusivities at all temperatures, E^{act}, as seen in previous studies [16, 88], and the second is to record each executed migration barrier in ANN-KMC and TAD, and the averaged value is displayed as E_m^*, shown in Fig. 3.7(b). In addition, the average of all static NEB barriers at 0 K is shown as function of composition, even though many of them may have never been visited during the vacancy diffusion. Figure 3.7(b) shows that E^{act} increases initially and reaches a maximum value at the percolation threshold $x_{Fe} = 20\%$, which was claimed in Ref. [16] to be one of the reasons for the sluggish diffusion in Ni-Fe alloys. The E^{act} trend is similar as the average of the NEB barriers, although for the later the maximum barrier occurs at a higher Fe concentration ($x_{Fe} \sim 35\%$). However, the E_m^* values based on the average of accepted barriers either from ANN-KMC or TAD simulations do not show a clear maximum. Instead, they exhibit a monotonically decreasing trend. Closer examination also shows that both KMC and TAD result in higher E_m^* values at higher temperatures at each composition. Figure 3.7(c) presents the distribution of executed migration barriers in the $Ni_{80}Fe_{20}$ alloy (which shows significant sluggish diffusion) at 500 K, 800 K, and 1200 K from KMC simulations, as well as the distribution of the static NEB barriers. Each spectrum is fitted to a Gaussian function in which the vertical dash line indicates its mean value. It shows apparent decline in the average migration energy as well as the distribution variance as the temperature decreases. Therefore, at low temperatures vacancy jumps are primarily along the low-barrier paths, and many of them are through the fast diffuser, Fe. At $x_{Fe} = 20\%$, however, there are only limited number of percolated paths that enable the long-range Fe diffusion. Therefore, vacancy diffusion may be trapped by Fe and sluggish diffusion occurs.

3.3.3 ANN-KMC results of the Random group

To exclude the statistical errors potentially induced by different atomic configurations, first the random configurations in ANN-KMC simulations are created as same as those used in the MD (note the small off-lattice distortions presented in the MD structures are ignored in ANN-KMC). In the next section, our further tests demonstrate that the choice of random configurations has a negligible effect on the diffusivities predicted by ANN-KMC. Figure 3.8(a) shows the total vacancy diffusivities of the Random group at different compositions predicted by the ANN-KMC from 900 K – 1300 K. The MD results are also shown for comparison. It should be noted that the ANN-KMC results are independent to the MD data because the jump attempt frequencies are the same as those in the Section 3.4.2 (for the MMC group) and no new fitting has been conducted. Nevertheless, ANN-MKC predicts vacancy diffusivities very close to the independent MD results, demonstrating the robustness and transferability of the ANN-KMC model. The minimum diffusivity happens at x_{Fe} = 20 ~ 25% at these temperatures, which is slightly lower than the MMC group (Fig. 3.6(a)). Similar to the partial diffusivities in the MMC group (Fig. 3.6(b)), in the Random group D_{Ni}^{random} and D_{Fe}^{random} also intersect at x_{Fe} = 20 ~ 25% and the cross-over composition slightly shifts rightward (to higher Fe concentrations) as the temperature increases, as shown in Fig. 3.8(b). The cross-over compositions are also close to the minimum diffusivities in Fig. 3.8(a). Figure 3.8(c) shows the jump fractions of Ni and Fe at different compositions at 1200 K. Again the Fe fraction increases while Ni fraction decreases with the increasing Fe concentration. The cross-over composition is at x_{Fe} = 20 ~ 25%, which is the same as that for the minimum total diffusivities shown in Fig. 3.8(a) and the cross-over composition for D_{Ni}^{random} and D_{Fe}^{random} shown in Fig. 3.8(b).

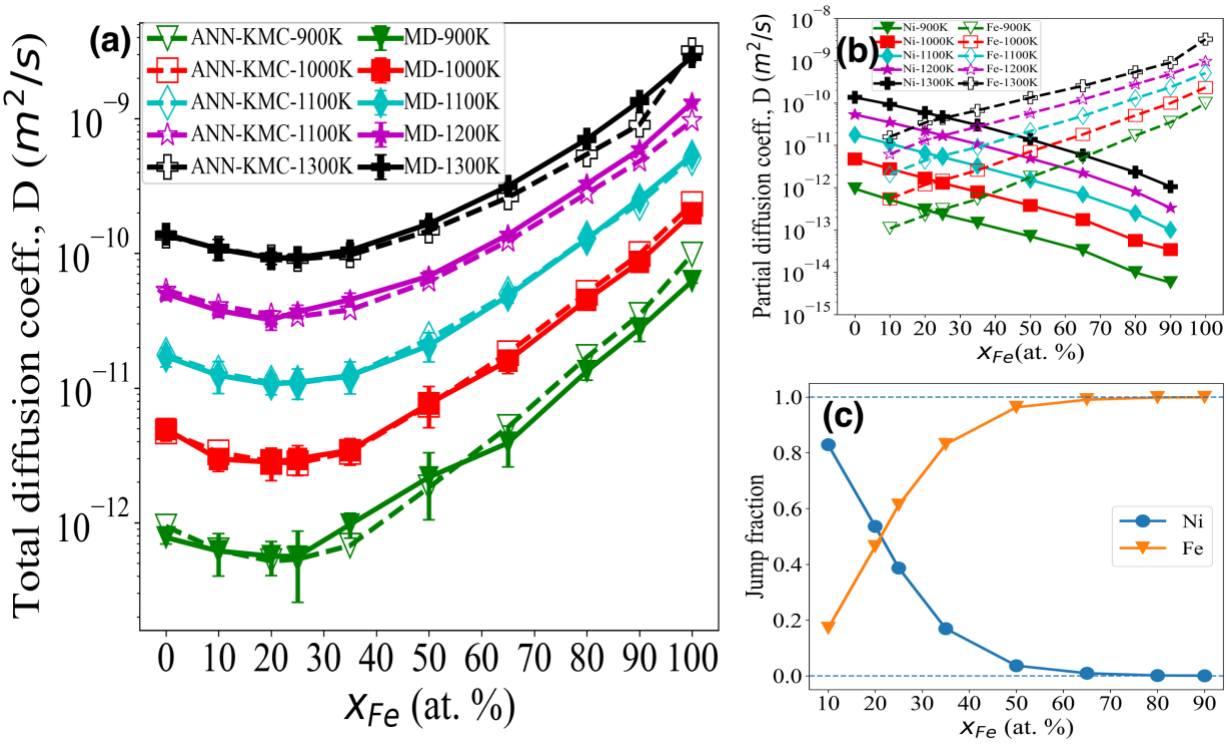

Fig. 3.8 (a) Total vacancy diffusivities at different Fe concentrations for the Random group alloys calculated from ANN-KMC. The independent MD results are also shown for comparison. Solid lines are MD results, and dash lines are ANN-KMC results. Each error bar represents the standard deviation of 6 – 10 MD simulations. The error bars in ANN-KMC results are ignored due to the negligible variances. (b) Partial diffusivities of Ni and Fe as a function of Fe concentration from the ANN-KMC simulations at different temperatures. (c) Jump fractions of Ni and Fe at different Fe concentrations from the ANN-KMC simulations at 1200 K.

TAD simulations are also conducted to study the vacancy diffusivities in the Random alloys. Figure 3.9(a) shows the good agreement between ANN-KMC and independent TAD results

at all compositions at 800 K, where the minimum total diffusivity is observed at x_{Fe} = 20%. The ANN-KMC is also used to calculate the total diffusivities of Random group alloys at 500 K. In comparison to the results at 500 K in the MMC group alloys shown in Fig. 3.7(a), the sluggish diffusion is less pronounced, indicating that the atomic configuration or SRO can be another important factor for affecting the sluggish diffusion. The ANN-KMC results in the Random alloys at 500 K are also compared with the work of on-the-fly KMC coupled with k-ART by Osetsky et al. [16], in which a constant v_o of 10^{13} s^{-1} was used for all compositions. Although the overall trend is similar between the two studies, the diffusivities in our work are about 5 times faster than in their work. The discrepancies could be due to different v_o values as well as the different methodologies for calculating vacancy migration energies in the two studies. Similar to the analysis for the MMC group (Fig. 3.7(b)), the Arrhenius-type treatment of activation energy (E^{act}) and the average migration energies (E_m^*) from the accepted events in ANN-KMC and TAD simulations at different compositions are shown in Fig. 3.9(b). Again, while the E^{act} curve has a convex shape with a maximal value at about x_{Fe} = 20%, the E_m^* curves for both ANN-KMC and TAD simulations decrease monotonically with x_{Fe}. Both E^{act} and E_m^* are different from the average of the static NEB barriers at 0 K. Figure 3.9(c) shows the distribution of the accepted migration energies in the $Ni_{80}Fe_{20}$ alloy obtained by ANN-KMC at 500 K, 800 K, and 1200 K, along with the distribution of the static NEB barriers. It can be clearly seen that many high-energy NEB barriers have never been visited by the ANN-KMC. In addition, the average migration energy of executed events (E_m^*) decreases as temperature decreases. For example, E_m^* = 1.16 eV at 1200 K while E_m^* = 1.07 eV at 500 K. Again, the results indicate that vacancy diffusion is mainly

through low-barrier paths at low temperatures. If the number of such low-barrier paths is limited (e.g., at x_{Fe} = 20%), sluggish diffusion occurs.

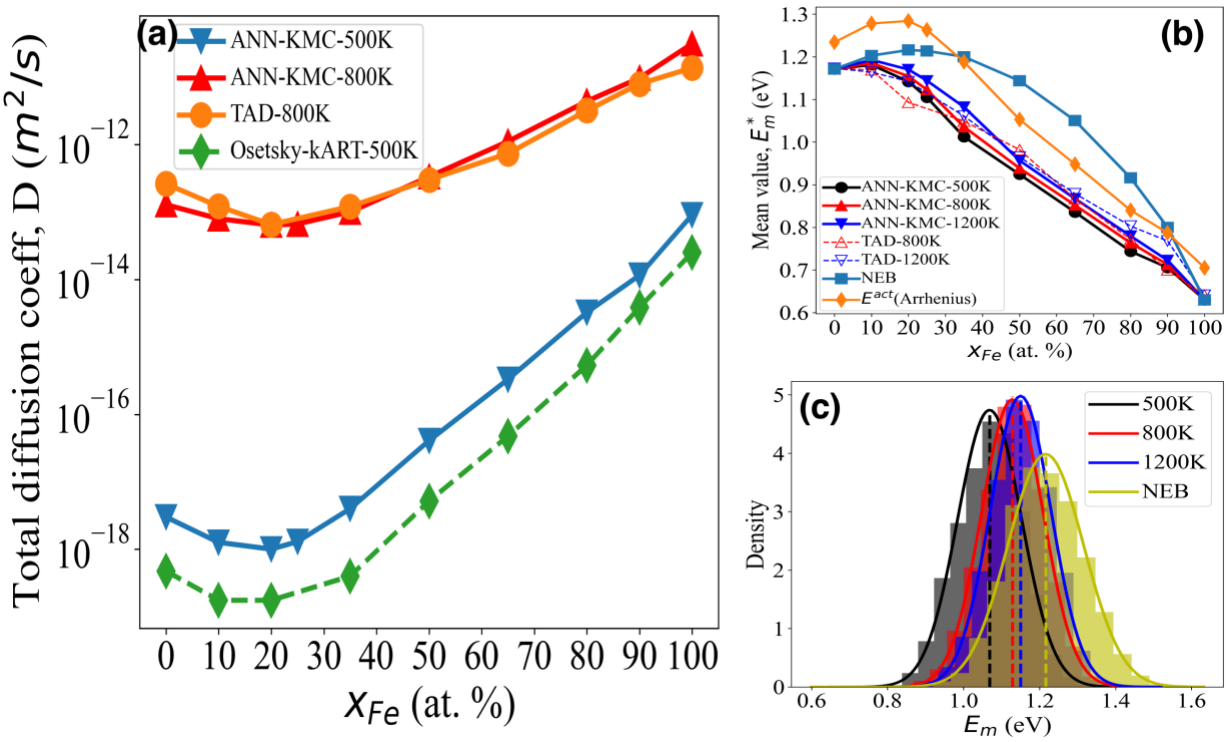

Fig. 3.9 (a) Comparison of the total diffusivities in the Random alloys obtained by TAD and ANN-KMC at 800 K at different compositions. The ANN-KMC results at 500 K are compared with a previous on-the-fly k-ART + KMC study [16]. (b) Two methods for estimating the effective vacancy migration energies at different compositions: Arrhenius-like treatment of ANN-KMC diffusivities at 500, 800 – 1300 K; The average of migration barriers from executed jumps during ANN-KMC and TAD simulations. For comparison, the average of the static NEB barriers at 0 K is also shown at each composition. (c) Migration barrier spectra of the static NEB barriers at 0 K and from the ANN-KMC simulations at 500K, 800K, and 1200K in the $Ni_{80}Fe_{20}$ random alloy.

3.4. Discussion

A comparison of the results from two structural groups reveals some commonalities and discrepancies. First, both MMC and Random structures have partial diffusivities and jump fractions crossing at x_{Fe} = 20~25%, which is close to the percolation threshold of Fe at x_{Fe} = 20%. However, while these cross-over values are identical to the minimal diffusivities in Random structures, MMC structures have the minimal diffusivities at x_{Fe} = 25~35%. The main factor that causes this discrepancy could be the presence of SROs in MMC structures, which can be a non-eligible factor in diffusion processes. For example, Zhao et al. have shown that the existence of ordered phases in concentrated alloys resulted in a significant delay in defect evolution [89]. As shown in Fig. 3.1(b), the MMC-optimized $Ni_{65}Fe_{35}$ (x_{Fe} = 35%) alloy has the largest extent of SROs. The SROs may hinder the vacancy diffusion, changing the minimum diffusivity from x_{Fe} = 20~25% in Random structures to 25~35% in the MMC structures. Second, both MMC and Random structures have a convex-shape curve of the effective migration energy (E^{act}) from the Arrhenius-type treatment, and the maximum value occurs at x_{Fe} = 20% in both cases, which coincides with the cross-over compositions for the partial diffusivities and jump fractions discussed above. The MMC and Random structures, therefore, may have a similar site percolation threshold around x_{Fe} = 20%, even though the MMC structures contain significant SROs. Third, the average migration barrier (E_m^*) for both MMC and Random structures, obtained by averaging the accepted migration barriers in ANN-KMC and TAD simulations, decreases monotonically with the increasing x_{Fe} or decreasing temperature. In addition, the E_m^* values are lower than the NEB and E^{act} counterparts for the same composition. Similar trends were also observed in Ref. [16] in which E_m^* from k-ART was 0.96 eV for $Ni_{50}Fe_{50}$ at 500 K while E^{act} and NEB values were 1.08

eV and 1.20 eV, respectively. The discrepancy between the average of the accepted barriers and the average of all NEB barriers indicates that only a fraction of NEB barriers are actually visited during vacancy diffusion, and most of the accepted barriers are at the smaller barrier side. Many of these smaller barriers are related to the jump of faster diffuser, Fe. When there are sufficient diffusion paths for Fe such as at high x_{Fe}, the overall diffusivity is high. However, if the Fe diffusion paths are limited such as near the Fe percolation threshold (x_{Fe} = 20%), the vacancy diffusion may be trapped by these local and disconnected small-barrier events, which leads to sluggish diffusion. As discussed earlier, however, this work also suggests that the percolation threshold may not be the sole factor for determining sluggish diffusion. Other factors including the presence of SROs can also influence it.

This work demonstrates that the combination of lattice KMC model and ANN-based on-the-fly determination of vacancy migration energy can achieve accurate results with high computational efficiency. However, the accuracy of the on-the-fly KMC is highly dependent on the quality of the ANN model. Here, the ANN-KMC approach is tested from three perspectives in order to evaluate its transferability, reliability, and practicality. First, the ANN model should be capable of predicting the migration energies for arbitrarily random configurations in a robust manner. Second, the accuracy of the ANN-KMC model should not be affected by the size of simulating system. Third, the effort required to obtain a database for training an ANN model should be feasible from a computational standpoint. To address the first concern, a set of random structures with the same compositions and number of atoms (4,000 atoms) as those in Section 4.3, but with different random arrangements of elements, are created. Regarding the second concern, a set of larger Ni-Fe random alloy system consisting of 108,000 atoms are created. Figure 3.10 shows

the total diffusivities calculated by ANN-KMC for the two new sets of alloys at 1000 K, along with the results for the original random alloys studied in Section 4.3. Clearly, both new sets of alloys have nearly the same diffusivities as those reported in Section 4.3 over the entire composition range, while the slight discrepancies are likely caused by the statistical errors. The results indicate that the ANN-KMC model is able to predict robust results for Ni-Fe alloys of different atomic configurations and sizes.

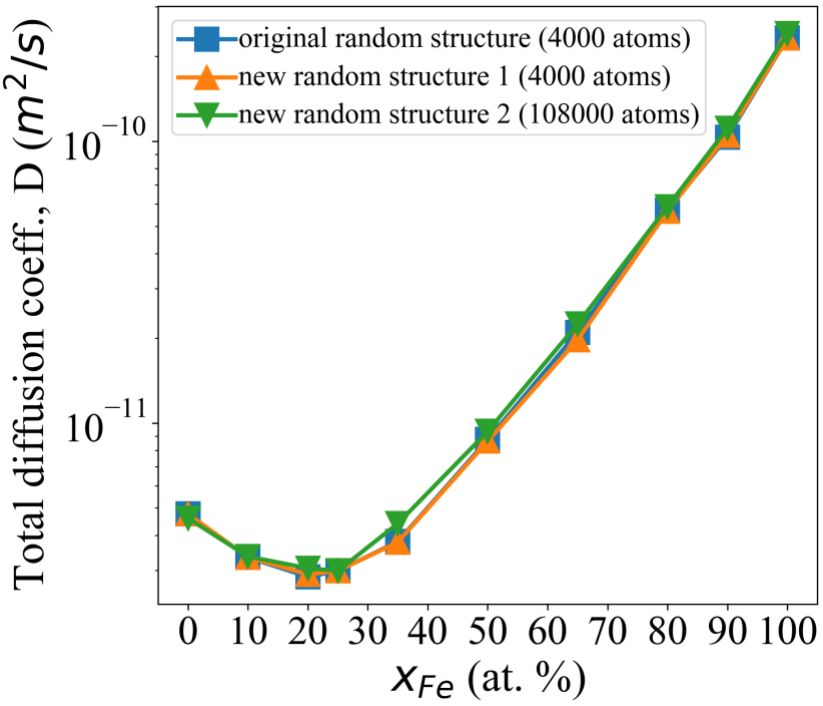

Fig. 3.10. Total vacancy diffusivities for two new sets of random structures of different system sizes (4,000 and 108,000) calculated by ANN-KMC at 1000 K. The results are compared with the diffusivities for the original Random structures reported in Section 3.4.3 at all compositions.

To address the third concern, a fraction of the NEB barrier database rather than the entire database (i.e., 32,000 data points in the MMC group) is chosen to complete the training, validation, and testing for obtaining an ANN model. Figure 3.11(a) illustrates the relationship between the ANN performance (using R^2 as the performance metrics) and the percentage of the database used. A two-fold effect is observed: On the one hand, the performance of the ANN model improves with the increasing percentage of database usage, as expected; On the other hand, the improvement is only significant at the early stage (for instance, from 10% to 20%); After that, the improvement is unremarkable. Next, the two ANN models that are trained with 10% and 20% of the database, respectively, are coupled with KMC to calculate total diffusivities in a random Ni-Fe system. The results are compared with the original ANN-KMC model that is based on the whole database in Section 4.3, as shown in Fig. 3.11(b). It is evident that the diffusivities obtained from these two new models only differ slightly from those obtained from the original full model, and the discrepancies are more evident for the ANN model using the 10% of database. Despite of this, both models yield similar trends in diffusivity, with an overall deviation less than 20% from the full model (note the large deviation mainly appears in the 10% case), which can be considered acceptable in practice. Such a trade-off could be useful when the computational cost for obtaining the NEB barriers is high, for example, in density functional theory (DFT) calculations.

A final remark is that to achieve an accurate prediction of E_m across all compositions, the ANN model should be trained on the NEB data that cover different compositions. For example, it is found that training an ANN model with only $Ni_{50}Fe_{50}$ data is not able to predict E_m accurately across all compositions. Thus, a good strategy for building the database is to use a subset of data from each composition and include many different compositions.

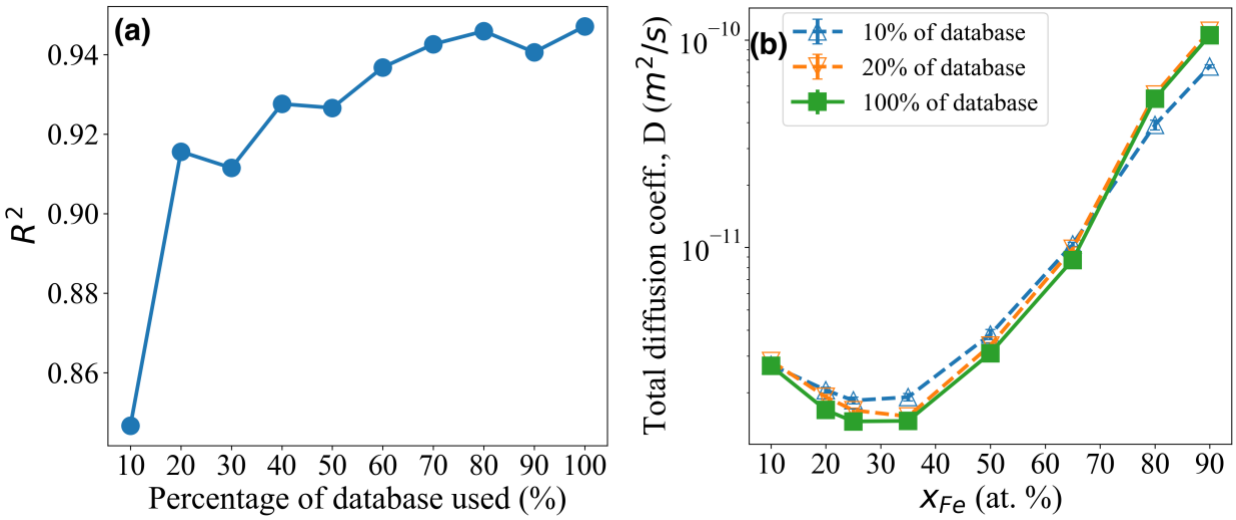

Fig. 3.11. (a) The R^2 performance of the ANN model using different percentages of the NEB database for obtaining an ANN model. (b) Total diffusivities predicted by the ANN-KMC models using 10%, 20%, and 100% of NEB database, respectively.

3.5. Conclusions

In this work, the ANN based machine learning method is coupled with KMC to study the sluggish vacancy diffusion in an fcc $Ni_{1-x}Fe_x$ (x = 0 – 1) concentrated model alloy system, in which the atomic-environment-dependent vacancy migration energy is determined by the ANN model on-the-fly. Two different groups of atomic configurations are studied: MMC-optimized structures that contain SROs and Random structures with randomly distributed Ni and Fe atoms. Using only the NEB migration barriers from the MMC structures for training, the ANN model can predict the

vacancy migration barriers in the Random structures with satisfactory accuracy. A composition- and temperature-dependent jump attempt frequency model is also developed in this work, which is calibrated only using the MD data of the MMC structures at 1300 K. Using this new jump attempt frequency model, the ANN-KMC model can predict the vacancy diffusivities in excellent agreement with independent MD and TAD results at both high and moderate temperatures, for both MMC-optimized and Random structures, and across all compositions, indicating the model has good robustness and transferability. This novel and computationally efficient ANN-KMC approach enables the simulation of vacancy diffusion at low temperatures and long timescale that are unreachable by other methods such as MD. This study also evaluates the practicability of the ANN-KMC approach by using a subset of database. The results indicate that using 20% of training data can result in a satisfactory accuracy. Therefore, the ANN-KMC approach may be applied to other studies in which the collection of the NEB barrier database is computationally expensive, such as in DFT calculations. Although this work uses a binary fcc concentrated alloy system as a model system, it is expected that the ANN-KMC approach can be generalized to other concentrated alloys with more components such as high-entropy alloys as well as other crystal structures.

For the $Ni_{1-x}Fe_x$ (x = 0 – 1) concentrated model alloy system studied in this work, a "sluggish diffusion" phenomenon is observed, with the lowest diffusivity being x_{Fe} = 20~25% for Random structures while x_{Fe} = 25~35% for MMC-optimized structures that contain SROs. Although these results support the argument that the percolation threshold (x_{Fe} = 20%) is an important factor for affecting sluggish diffusion, this work also shows that other factors such as SRO can influence the sluggish diffusion behavior. At low temperatures such as 500 K, the sluggish diffusion becomes more pronounced, particularly in the MMC-optimized structures. The

average of the accepted migration barriers from ANN-KMC modeling is smaller than the average of all NEB barriers. In addition, it decreases with the decreasing temperature. The results indicate that smaller-barrier events, which are mainly related to the faster diffuser Fe, play significant roles on affecting the total diffusivity. When the Fe migration paths are limited and disconnected such as at x_{Fe} < 25%, the smaller-barrier events may trap the vacancy locally to inhibit its long-range diffusion and thus induce sluggish diffusion. When the Fe migration paths are abundant at high Fe concentrations, these smaller-barrier events can dominate the long-range diffusion and lead to fast diffusivities.

CHAPTER 4 High-Throughput Artificial Neural Network - Kinetic Monte Carlo (ANN-KMC) Framework for Diffusion Studies in Equiatomic and Non-equiatomic FeNiCrCoCu High-Entropy Alloys

4.1. Introduction

High-entropy alloys (HEAs), which typically contain five or more principal elements with intrinsic chemical disorder [90, 91], have garnered immerse attention in recent years, ushering in what can be aptly described as a "High-Entropy Materials" age [92]. The heightened interest stems from their exceptional mechanical and structural properties, such as strength retention at high temperatures [93], exceptional fracture toughness at cryogenic temperatures [2, 94], good corrosion resistance [34, 95], and outstanding radiation resistance [96]. In addition, some dual-phase HEAs are among the few alloys known to overcome the strength-ductility tradeoff [97]. It has been suggested that some of these excellent properties may be tied to the possible sluggish diffusion kinetics of HEAs [7]. Specifically, the random arrangement of principal elements in HEAs leads to substantial fluctuations in the potential energy landscape (PEL), creating enormous atomic traps and barriers that could result in a reduced diffusivity. As such, the concept of "sluggish diffusion" has been commonly quoted to explain many of the outstanding properties in HEAs [7-9]. However, numerous experimental and computational studies have shown that sluggish diffusion in HEAs or in concentrated alloys is a rather complex phenomenon, yielding conflicting results [10, 13, 14, 16, 21, 98]. To date, the existence of sluggish diffusion remains a subject of ongoing debate. Therefore, understanding the mechanism of sluggish diffusion — if

present, and designing HEAs with enhanced performance continue to be a challenging endeavor, given the complexity of HEAs and the conflicting results presented in various studies.

Understanding the controlling mechanism of sluggish diffusion is fundamentally rooted in deciphering how atomic transport is influenced by the complex PEL or local atomic configuration (LAC) in HEAs. While the experimental techniques such as diffusion couples or tracer techniques can accurately measure the diffusion coefficients [13, 37], they provide little insights about the underlying diffusion mechanisms. As an alternative, atomic-level simulation methods such as molecular dynamics (MD) are often employed to study the diffusion mechanisms in concentrated alloys including HEAs [16, 21, 98]. Previous simulation studies in binary or ternary concentrated alloys provided valuable insights about the sluggish diffusion mechanisms, which could inform our approach as we delve deeper into the intricacies of HEAs. For example, Osetsky et al. have shown that the compositional-dependent diffusivity in a Ni-Fe concentrated alloy reaches its minimum at the percolation threshold, about 20 at.% of Fe, instead of the equiatomic composition. The coincidence of retarded diffusion with the percolation threshold suggests that the local trapping effects could be caused by the faster-diffusing species, Fe, before it reaches the percolation threshold [16, 99]. However, recent work on concentrated CoCrNi ternary alloys revealed that the percolation threshold does not always result in sluggishness, and the role of PEL may be more critical [17]. In our recent MD studies of diffusion in an equiatomic FeNiCrCoCu HEA, no sluggish effect is observed in the vacancy-mediated bulk diffusion [21], although the diffusion in a Σ5(210) grain boundary is sluggish [98]. These findings suggest a multitude of factors can affect defect/species diffusion in HEAs, many of which remain to be explored. For example, sluggish diffusion could exist at some non-equiatomic compositions in HEAs. Given

their enormously large compositional space, it is very costly and unfeasible to use experimental techniques to search for the sluggish compositions. Another challenge for experiments is the lack of a fair reference system for determining the sluggish effect, while in modeling a hypothetical average atom (AA) material [100] can be used, which predicts the same average bulk properties as in the HEA but without HEA's compositional complexity [21]. Therefore, to solve these challenges it is imperative to design a high-throughput modeling framework to study the diffusion behavior in HEAs of both equiatomic and non-equiatomic compositions.

Although MD is a powerful tool for investigating atomic-level diffusion mechanisms, its applicability is limited by its inherently short timescale (typically at a few tens of nanoseconds). For vacancy-mediated diffusion studies, the applicable temperature range is typically limited to high temperatures [21] due to its inherent timescale limitation. However, multiple diffusion mechanisms can happen simultaneously at high temperatures while some of them may not be relevant at low temperatures of interest. Even though the timescale of MD can be extended to microseconds through modern supercomputers, the problem may still persist for studying the diffusion in concentrated alloys. For instance, in a 4000-atom Ni-Fe alloy at a high temperature of 1200 K, a microsecond-scale MD simulation (a very long simulation time for MD) captured only about 4500 vacancy jumps [62]. Consequently, the complex atomic environment in concentrated alloys may not be visited sufficiently. In addition, MD simulations do not perform well at low temperatures of interest so that some rare but important diffusion events might not be captured by MD. In this regard, the kinetic Monte Carlo (KMC) method has been employed in attempts to extend the diffusion simulation timescale as well as the temperature range for HEAs, as reported in [22, 23]. However, conventional KMC encounters difficulties of describing the rough PEL in

HEAs because the vacancy migration barrier varies significantly with the LAC. Several approaches have been developed to approximate the rough PEL, such as random sampling method and species-average migration barrier method [22-24]. However, these approaches over-simplify the effects of the varying atomic environment surrounding the diffusing objects, which may lead to inaccurate conclusions. A reliable KMC simulation requires an accurate description of the candidate migration barriers as a prior knowledge at each defect jump event. This, in turn, demands an on-the-fly calculation of migration barriers using the nudge elastic band (NEB) [25] or the activation relaxation technique nouveau (ARTn) [26], which leads to an immense computational cost and is often impractical.

Alternatively, machine learning (ML) can serve as an efficient tool to map the dependency of PEL or migration barrier on the LAC surrounded by a defect and/or the migrating solute. Once a well-trained ML model is established, the computationally expensive on-the-fly calculation of migration barriers in KMC can be replaced, enabling long-time and accurate simulations of defect/species diffusion in concentrated alloys including HEAs. Previous studies have demonstrated that the artificial neural network (ANN), which is a widely used ML method, can effectively serve as an on-the-fly barrier calculator for KMC modeling in concentrated alloys with up to four components [17, 101-103], including our recent ANN-KMC modeling of vacancy-mediated diffusion in concentrated Ni-Fe alloys for different compositions, short-range orders (SROs), and temperatures [104]. The accuracy of the ML model is a prerequisite for developing such a reliable ML-KMC framework. However, previous studies have shown that the prediction performance tends to decline with the rapidly increasing complexity of LACs as the number of alloying species increases [17, 101]. For instance, Xu et al. reported that their ANN models

achieved mean absolute errors (MAEs) of 15, 35, and 88 meV for their binary, ternary, and quaternary alloys, respectively [101]. Therefore, particular attention should be given to constructing an accurate ML model for HEAs when more components are present. In addition, one limitation of current ML models is their limited predictability, because they might only be applied to the systems covered in the training dataset. Specifically, a ML model trained on the equiatomic composition may not be capable for non-equiatomic compositions or their sub-systems. As a result, a different ML model should be trained for each distinct composition, leading to significant inefficiency when it comes to deal with the vast composition space of HEAs.

In this work, we present the first comprehensive effort to combine ANN-based ML method and KMC for studying the possible sluggish diffusion in five-component HEAs, using FeNiCrCoCu as a model HEA system and with the focus on its non-equiatomic compositions. This HEA system is described by an EAM (Embedded Atom Method) potential developed by one of present authors (Farkas) [105]. There are a few reasons for choosing this HEA system. First, it predicts the stable face-centered-cubic (FCC) phase over a wide range of compositions so that the multi-phase complexity in some HEA systems [106] is excluded. Second, it has a low heat of mixing (-0.0002 kJ/mol) so that the ordering effect is small. Third, its pure components have a wide spread of diffusivities (e.g., Cu diffuses much faster than Ni and Fe in this model system) [21] so that the role of different species diffusivities on sluggish diffusion can be explored. To develop a robust ML model for predicting the vacancy migration barriers, special considerations have been given to the construction of LACs, which serve as training features (descriptors) for our ANN model. Remarkably, our ANN model is trained using a modest dataset of about 17,000 migration barrier samples only from the equiatomic FeNiCrCoCu composition, yet it is capable of

accurately predicting non-equiatomic compositions as well as its respective sub-systems, i.e., quaternary, ternary and binary alloys. Based on the success of our previous ANN-KMC modeling work for the Ni-Fe binary system [104], a species- and temperature-dependent jump attempt frequency model has also been developed for the current HEA system, which is derived only from pure components. In addition, an average-atom KMC (AA-KMC) model has been developed to approximate the AA materials without the need of developing a distinct AA interatomic potential [100] for each HEA composition, serving as references for determining the existence of sluggish diffusion. The vacancy-mediated diffusivity obtained from our ANN-KMC and AA-KMC models show excellent agreement with the independent MD simulations, at least within MD's accessible temperature ranges. The ANN-KMC and AA-KMC methods are then used to study the $(FeNiCrCo)_{1-x}Cu_x$ alloys with x = 0 – 30%, with the aim of determining if the percolation of the fastest diffuser (Cu) leads to sluggish diffusion. More importantly, the two high-throughput methods are utilized to explore the extensive compositional space of HEAs (1,500 distinctive non-equiatomic HEA compositions) to study the controversial sluggish diffusion effect.

4.2. Methods

4.2.1 Generating datasets of vacancy migration barriers

To collect the training dataset for the ANN model, the NEB method implemented in the LAMMPS [51] was used to calculate vacancy migration barriers in an equiatomic FeNiCrCoCu HEA. A $10a_0 \times 10a_0 \times 10a_0$ FCC crystal structure with randomly populated Fe, Ni, Cr, Co, and Cu

elements at the equimolar ratio (20 at.% each) was constructed. As mentioned earlier, the EAM potential developed by Farkas et al. was used to describe the interatomic interactions [105]. In each NEB calculation, a vacancy was created by removing an atom and then one of its twelve nearest neighboring atoms was randomly selected to be the moving atom. Once this vacancy-moving atom path was established, the path remained fixed while the atoms (including the moving atom) in the entire system were randomly assembled to constitute the target composition. This random assembly process was repeated about 17,000 times to generate different LACs around the vacancy migration path. Both the initial and final states of a migration event were relaxed by the conjugate gradient algorithm with the force stopping tolerance of 10^{-2} eV/Å and energy convergence criterion of 0.0 eV. The maximum number of iterations was 2,000. In all NEB calculations, the number of NEB images (excluding the initial and final states) was 13 and the spring constant was set to 1.0 eV/Å^2. In this manner, a dataset of ~17,000 samples was collected from the equiatomic FeNiCrCoCu composition, serving as the basis of training and testing data for the ANN model. To assess the generalizability of the trained ANN model, multiple supplementary datasets were also produced using the same NEB approach. Specifically, NEB calculations were carried out on an assortment of randomly chosen non-equiatomic FeNiCrCoCu alloys, yielding approximately 2,500 migration barrier samples. In addition, 2,000 migration barrier samples were collected for each equiatomic sub-system of the FeNiCrCoCu alloy, including five quaternary (i.e., 10,000 barriers in total), ten ternary, and ten binary alloys. It should be emphasized that these supplementary datasets were not included in the ANN model training. Instead, they were used as independent data to verify the predictability of the ANN model.

4.2.2 Training the ANN model

In our previous work, it has been demonstrated that an ANN-based ML model is able to accurately predict vacancy migration barriers in a concentrated binary Ni-Fe alloy of any composition using LAC information as a descriptor [104]. In this work, a more robust LAC representation is introduced: first a raw LAC is constructed then it is transformed to an encoded LAC. The raw LAC collects all element types up to the i^{th} nearest neighboring (NN) shell surrounding both the vacancy site and the migrating atom. Given the one-to-one correspondence between the input training features and neurons in the ANN model, it becomes necessary to maintain the consistency of atom sequence in the raw LACs. In this regard, the "Adaptive Path Alignment (APA)" method is designed, as depicted in Fig. 4.1. Initially, a "reference path" is created to represent the migration path for the pre-determined vacancy-moving-atom pair described in Section 4.2.1. For other migration paths, their local coordinate systems are rotated to align with the chosen "reference path". Note that the choice of the "reference path" does not impact the final ANN performance and the primary objective is to ensure that the input LAC sequence maintains a consistent relative ordering. A similar approach called the "Coordinate System Transformation (CST)" method, has been previously documented in [103].

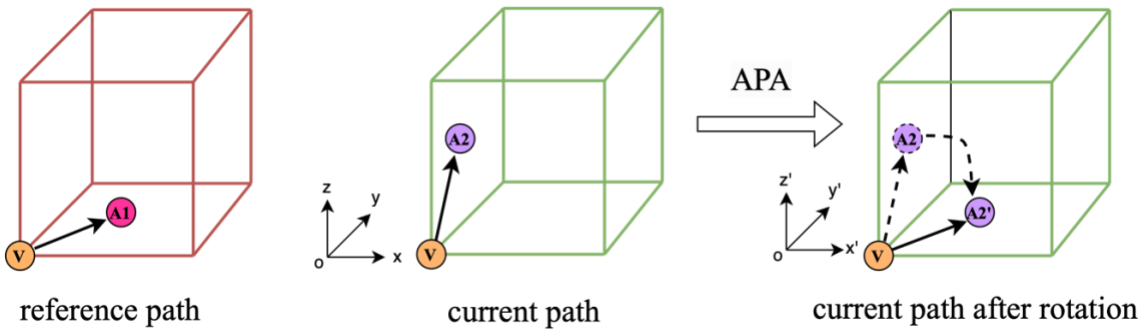

Fig. 4.1. Schematic illustration of the "Adaptive Path Alignment" (APA) method. The reference path (V-A1) corresponds to the pre-determined vacancy-moving-atom pair in Section 2.1. For the current migration path (V–A2), the local coordinate is rotated to a new position (V-A2'), which aligns with the reference path.

Following the APA method, with a given migration event, the raw LAC around the vacancy-moving-atom pair up to i^{th} NN shell can be established. As an example, the first two NN shells, as well as the total raw LAC can be represented below,

$$LAC(raw, 1^{st}nn) = W_{1nn}[3\ 2\ 4\ 2\ 5\ 3\ 2\ 5\ 3\ 4\ 3\ 3\ 2\ 5\ 1\ 5\ 2\ 5\ 5],$$

$$LAC(raw, 2^{nd}nn) = W_{2nn}[1\ 4\ 5\ 5\ 4\ 4\ 2\ 2\ 2\ 1\ 1\ 4],$$

$$LAC(raw, total) = [LAC(raw, 1^{st}nn), LAC(raw, 2^{nd}nn), \ldots, LAC(raw, i^{th}nn)],$$

where the numbers in each list represent the element types, with Fe, Ni, Cr, Co, and Cu denoted by 1, 2, 3, 4, and 5, respectively. W_{1nn} and W_{2nn} signify the initial training weight coefficients for the first and second NN shells, respectively. A closer NN shell is assigned with a larger initial weight, which is then trainable during the ANN model optimization. The 1st NN shell LAC combines the 1st NN atoms around the vacancy and the moving atom. Since four of them overlap, there are a total of 19 atoms, including the moving atom (which is the 1st atom in the list) but not the vacancy site. The 2nd NN shell LAC consists of 12 atoms, some of which overlap with atoms in the 1st NN shell LAC. This overlap occurs because an atom could simultaneously serve as the first NN atom for the vacancy and as the second NN atom for the moving atom, and vice versa.

Therefore, even though those atoms are already included in the 1st NN LAC, they still appear in the 2nd NN LAC. The final total raw LAC is the combination of all considered NN shells.

While the raw LAC representation works well for simpler systems, such as in a binary A-B alloy system where "1" represents A and "2" represents B [75, 104, 107], it can cause a significant imbalance in describing HEAs. In particular, using numerical values like "5" for Cu and "1" for Fe unintentionally emphasizes the role of Cu while downplays the importance of Fe, leading to a biased training during the gradient descent optimization process. To address this issue and ensure that all species are treated equally, we employed the "one-hot" representation with a dimension of five to encode the raw LACs. As a result, the aforementioned raw LAC for the first NN shell ([3 2 4 2 5 3 ...]) is reformulated in this new encoding scheme,

$$LAC(1^{st}nn) = W_{1nn}\begin{bmatrix}000000\\010100\\100001\cdots\\001000\\000010\end{bmatrix},$$

where each column represents one neighboring atom and the position of "1" indicates its type. The rest of NN shells follow the same encoding method. To choose the ANN architecture, a straightforward three-layer structure was constructed, consisting of an input layer, a hidden layer with ten neurons, and an output layer. The encoded LACs serve as the input features for the ANN model. To train and optimize the parameters in the ANN model, the Levenberg-Marquardt method [74] was used, which is a hybrid method that combines the Gauss-Newton update and gradient descent approaches to search for an optimal solution.

To determine the optimal number of NN shells, the number of NN shells in LACs was progressively increased, from only the first NN shell up to a maximum of nine NN shells. It showed that the ANN performance improved with the number of NN shells, as expected. However, a satisfactory performance can be obtained by including only the first three NN shells. Details will be provided in the 4.3. Results. After the ANN model was developed based on the equiatomic composition, multiple supplementary (but independent) datasets as mentioned in Section 4.2.1 were used to evaluate the generalizability of the ANN model for the non-equiatomic HEAs and equiatomic sub-systems that were not covered in the ANN model training and testing.

4.2.3 Coupling ANN and KMC models

Leveraging the well-trained ANN model, the migration barrier for any given LAC can be accurately predicted in an efficient manner. This allows us to treat the ANN model as an on-the-fly barrier calculator for the KMC model (ANN-KMC), which is implemented in the KMCLib package [77] by the present author (Huang). The size of the ANN-KMC system is also $10a_0 \times 10a_0 \times 10a_0$. For each vacancy jump event i, the ANN model collects its LAC information and predicts the migration barriers across all twelve possible migration paths, which are then used to calculate corresponding jump rates,

$$\Gamma_{ij} = \nu_o \exp\left(-\frac{E_{m,ij}}{k_B T}\right), \tag{4.1}$$

where $E_{m,ij}$ is the ANN-predicted migration barrier for the jump event i along a candidate migration path j; v_o is the jump attempt frequency, k_B is the Boltzmann constant, and T is the absolute temperature. The KMC then selects a migration path based on the jump rates and the elapsed time is calculated based on the residence time algorithm [64]. In this work, 300,000 ANN-KMC steps were simulated for each simulation condition to ensure sufficient jump statistics. Using the resulting atomic trajectories, the vacancy diffusion coefficient can be calculated using the sum of atomic square displacements (ASD) of all atoms in the system [104],

$$D = \frac{ASD}{6t} \tag{4.2}$$

where t is the simulation time and the factor of 6 is for the 3D diffusion. For each condition, six independent simulations were conducted and the average diffusivity is reported in this work. It should be noted that the diffusivity calculated here is the vacancy mobility rather than the self-diffusivity. For the latter, the vacancy formation energy distribution should be included, which can be predicted by Zhang et al.'s model [57]. Our ANN model does include the formation energy difference along each migration path because the forward and backward migration barriers are different, giving a direction to the migration path. However, the inclusion of the complete vacancy formation energy distribution in the ANN-KMC modeling is beyond the scope of this work and can be a future research topic.

4.2.4 MD simulations

To validate the reliability of the ANN-KMC results, independent MD simulations of single-vacancy diffusion in a $10a_0 \times 10a_0 \times 10a_0$ FCC system were conducted as benchmarks for considered systems within the accessible temperature range of MD, from 1600 to 2000 K, using LAMMPS [51]. It should be noted that this temperature range is higher than the melting temperatures of many HEAs in experiments, which are typically below 1800 K [7, 108, 109]. However, the EAM potential used in this work predicts the equilibrium melting temperature (solid-liquid coexistence temperature) for the equiatomic HEA is about 2070 K [21]. The use of periodic boundary conditions in MD simulations makes the actual melting point even higher (at the superheating limit). Therefore, all the simulation systems remained crystalline, which were also confirmed by our visual inspections. The MD simulations were performed in a NPT ensemble (constant number of atoms, pressure, and temperature), with the Nose-Hoover-style thermostat and barostat [53, 110] controlling the system temperature and pressure (at zero bar), respectively. A time step of 2 fs was employed in all MD simulations. Four independent simulations were conducted for each condition, each lasting up to 20 ns of simulation time. Same as in ANN-KMC approach, the diffusion coefficients were calculated using the Eq. (4.2).

4.3. Results

4.3.1 ANN model performance

As mentioned in the 4.2. Methods section, the dataset used for training and testing the ANN model was obtained exclusively from the equiatomic FeNiCrCoCu HEA. This dataset was then randomly divided into training (including validation) and testing sets, with a ratio of 9 : 1. The performance of the ANN model was evaluated based on the MAE on the testing set. Figure 4.2 shows the relationship between MAE and the number of NN shells utilized for constructing the LACs. As expected, the MAE decreases as more NN shells are included. For instance, the ANN model considering only the first NN shell, which includes 19 atoms, yields a MAE of 47 meV, while the ANN model including nine NN shells, encompassing 331 atoms, results in a MAE of 25 meV. It is worth noting that during the training of the ANN model incorporating more than six NN shells, overfitting can easily occur due to the increasing degree of freedom of the LACs. To remedy this issue, the number of neurons in the hidden layer was reduced from ten to five. Although including more NN shells does improve the accuracy to some extent, it also raises the computational cost. In addition, it may be challenging to generalize the approach for simulation systems of small sizes, such as those used for density functional theory (DFT) calculations. In fact, it can be seen in Fig. 4.2 that the MAE decreases slowly when three or more NN shells are included. To balance the accuracy and efficiency, the ANN model that incorporates the first three NN shells was found to deliver a satisfactory performance with a MAE of 32 meV and was chosen for this study. Figures 4.3(a – c) show the good performance of this ANN model on training set, testing set and the entire dataset that were obtained from the equiatomic FeNiCrCoCu HEA.

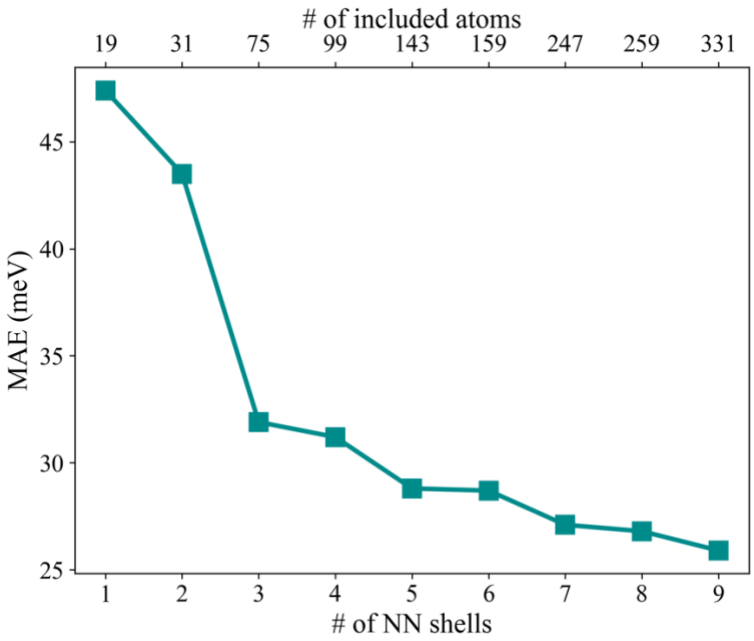

Fig. 4.2. Mean absolute error (MAE) of the ANN model on the testing set in relation to the number of NN shells included in LACs.

Upon finalizing the ANN model, its generalizability was evaluated from two perspectives: (1) its ability to generalize from equiatomic to non-equiatomic HEA compositions, and (2) extension of its predictability to its sub-systems. For the first assessment, the ANN model was applied on a dataset that includes ~2,500 migration barrier samples from randomly selected non-equiatomic FeNiCrCoCu HEAs (as mentioned in Section 4.2.1). Figure 4.3(d) presents the performance of the trained ANN on this supplemental dataset. It can be seen that the ANN model achieves a satisfactory accuracy with a MAE of 42 meV, despite this extra dataset being entirely independent to the dataset used to train the ANN model. This underscores the predictive capability

of the ANN model to extend beyond the equiatomic composition, demonstrating its potential for studying non-equiatomic HEA systems.

For the second evaluation, separate tests were conducted on 5 quaternary, 10 ternary, and 10 binary equiatomic sub-systems, each system containing 2,000 migration barrier samples (as mentioned in Section 4.2.1). Again, these migration barriers obtained from the sub-systems are invisible to the trained ANN model. Figure 4.4 illustrates the ANN prediction performance for the five quaternary alloys, FeNiCrCo, FeNiCoCu, FeCrCoCu, FeNiCrCu, NiCrCoCu, with respective MAEs of 34, 47, 39, 38, and 30 meV, and Pearson correlation coefficient (R) of 0.99 in all cases (note R = 1 means the perfect prediction). The overall MAE for the quaternary datasets is 37 meV, indicating an excellent level of prediction accuracy. Figure 4.5 presents the prediction performance for all ten ternary alloys, i.e., CrCoCu, FeCrCo, FeNiCo, FeNiCr, NiCrCo, NiCrCu, NiCoCu, FeNiCu, FeCrCu, and FeCoCu, with respective MAEs of 31, 39, 54, 33, 25, 25, 28, 57, 49, and 73 meV, and R > 0.95 for most cases. The overall MAE for the ternary datasets is 41 meV, which is still a commendable level of accuracy. Figure 4.6 displays the prediction performance for ten binary systems: NiCr, NiCu, FeCr, CoCu, FeNi, CrCo, CrCu, FeCo, FeCu, and NiCo, with respective MAEs of 20, 32, 50, 40, 43, 25, 29, 127, 127, and 40 meV, and R > 0.95 for all cases except for NiCo. The MAEs for FeCo and FeCu are a little bit large. For FeCu, the large MAE could be caused by the difference in lattice constant: the lattice constant for the equiatomic FeNiCrCoCu alloy used for training the ANN model is 3.55 Å, and most sub-systems have the values close to it, whereas that for FeCu is 3.59 Å. The reason for the large MAE in the FeCo is unclear. Nevertheless, the slightly large errors are still considered acceptable. The overall MAE for the binary datasets is 54 meV, which still represents a satisfactory level of accuracy,

particularly when considering the substantial compositional disparity between binary and quinary systems. Based on the good performance on these sub-systems, it is reasonable to state that the trained ANN model can be effectively extended to such sub-systems.

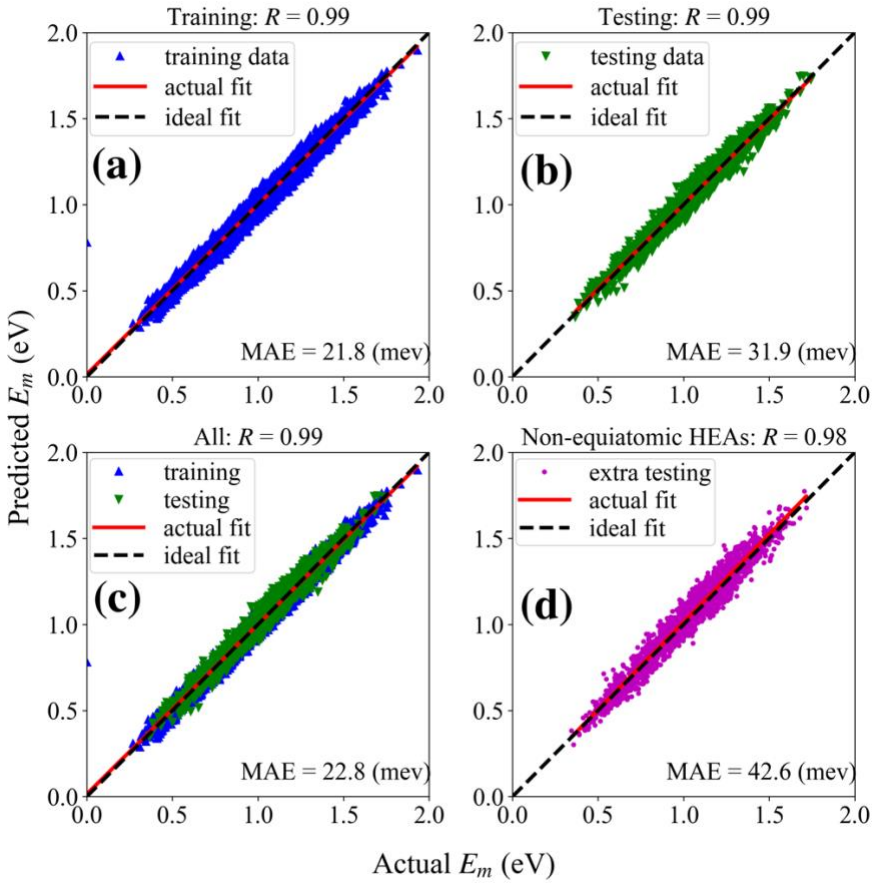

Fig. 4.3. Prediction performance of the ANN model incorporated with the first three NN shells on (a) training set, (b) testing set, (c) the entire dataset from the equiatomic FeNiCrCoCu HEA, and (d) independent supplemental dataset from non-equiatomic FeNiCrCoCu HEAs.

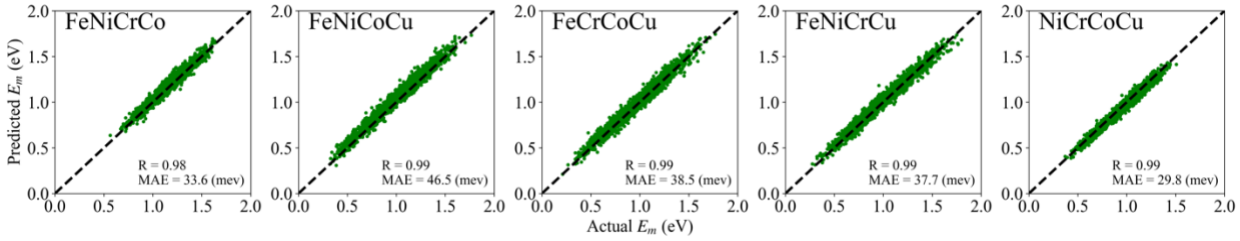

Fig. 4.4. Prediction performance of the ANN model on five independent quaternary systems.

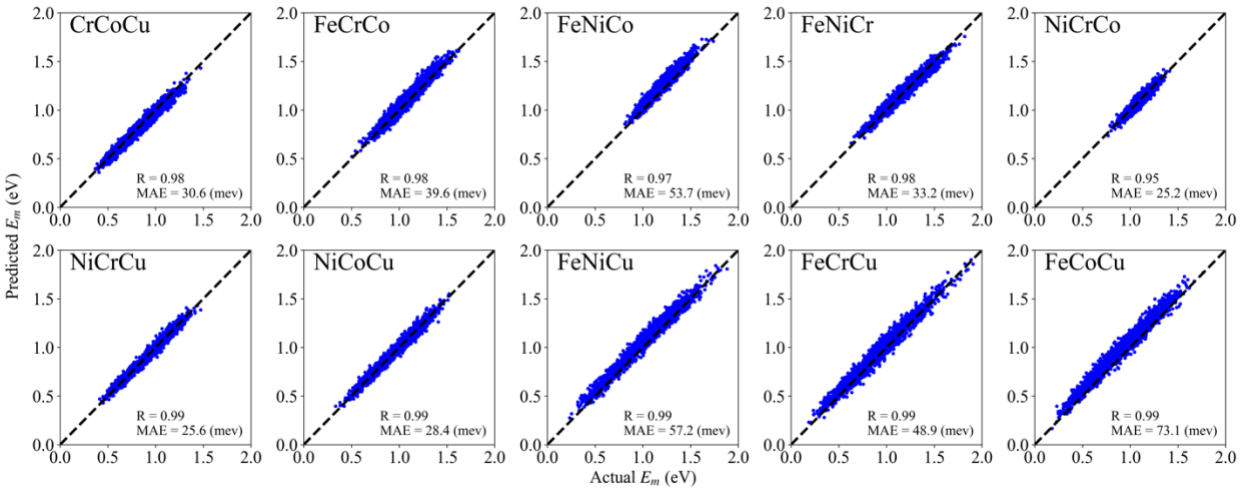

Fig. 4.5. Prediction performance of the ANN model on ten independent ternary systems.

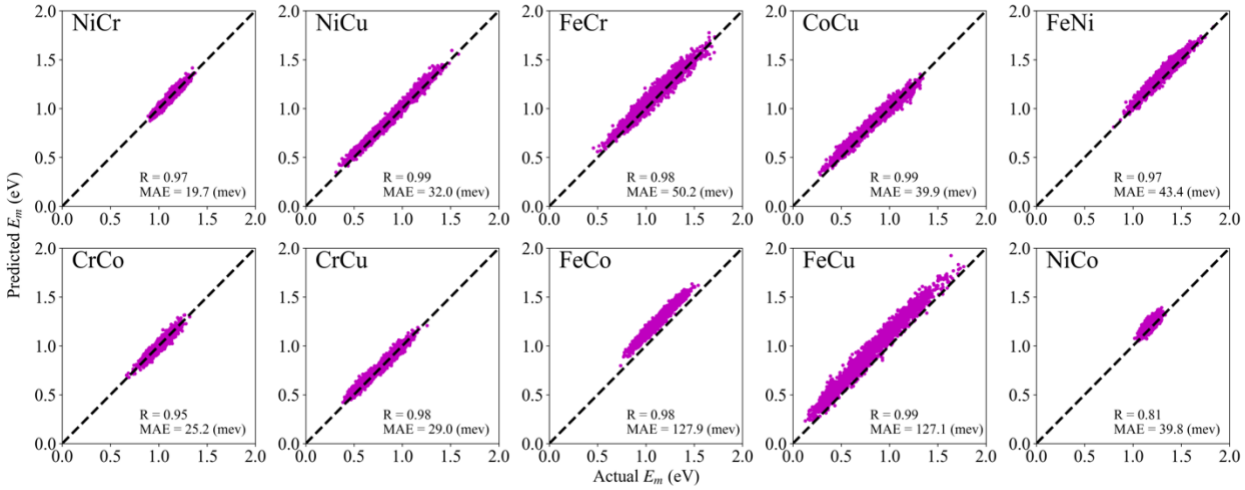

Fig. 4.6. Prediction performance of the ANN model on ten independent binary systems.

4.3.2 ANN-KMC and AA-KMC Results

After the well-trained ANN model is developed, it is coupled with KMC (ANN-KMC) to investigate vacancy-mediated diffusion in various HEAs. While many conventional KMC simulations commonly employ a constant jump attempt frequency (v_o = 10^{12} ~ 10^{13} s^{-1}) [80, 111], our recent study has demonstrated that v_o can be affected significantly by the temperature and composition in concentrated alloys [104]. To determine v_o for our ANN-KMC simulations of HEAs, the conventional KMC simulations were performed first with a fixed v_o = 10^{13} s^{-1} for each of the five pure components of the FeNiCrCoCu HEA, which are entirely independent of the ANN model since the migration barrier is constant for each pure component.

Figure 4.7(a) displays the diffusion coefficients of five pure components obtained from the conventional KMC using the fixed v_o in the Arrhenius plots. The results from independent MD

simulations are also shown as benchmark data. Evidently, there are some discrepancies between KMC and MD results for some pure components, such as Fe and Cu, suggesting that the fixed v_o value is likely the reason for these discrepancies. By fitting the results of KMC to MD for these pure components, the v_o of each pure component can be approximated as a linear function with temperature, as shown in Fig. 4.7(b). The fitted functions of v_o for the five pure components are provided in Eqs. (4.3) – (4.7). The jump attempt frequency for an alloy, v_o^{alloy}, is then treated as the weighted sum of its components based on the alloy composition, as expressed in Eq. (4.8).

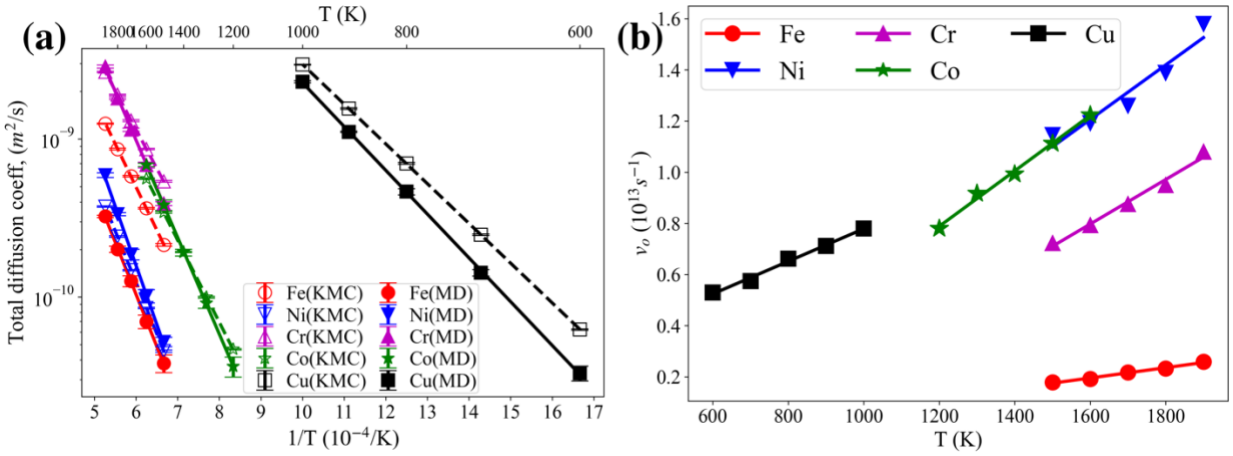

Fig. 4.7. (a) Diffusion coefficients for five pure components obtained from the conventional KMC simulations (open symbols and dashed lines) at different temperatures in the Arrhenius plots, using a fixed v_o value of 10^{13} s^{-1}. The independent MD results (filled symbols and solid lines) are shown for comparison. (b) The v_o derived from fitting the conventional KMC to MD results for each pure component at their respective temperature ranges.

$$v_o^{Fe}(T) = 2.01 \times 10^{-4}T - 0.126, \quad (4.3)$$

$$v_o^{Ni}(T) = 1.07 \times 10^{-3}T - 0.499, \quad (4.4)$$

$$v_o^{Cr}(T) = 8.71 \times 10^{-4}T - 0.596, \quad (4.5)$$

$$v_o^{Co}(T) = 1.08 \times 10^{-3}T - 0.511, \quad (4.6)$$

$$v_o^{Cu}(T) = 6.37 \times 10^{-4}T + 0.141, \quad (4.7)$$

$$v_o^{alloy}(T) = \sum_{X \in alloy} C_X v_o^X(T). \quad (4.8)$$

In Eq. (4.8), C_X is the concentration of the component X in the alloy. The unit is 10^{13} s^{-1} in all of the Eqs. (4.3) – (4.8). There are two possible strategies to implement the composition- and temperature-dependent v_o model for alloys in the ANN-KMC calculations. The first approach is to specify the corresponding v_o^X values for different moving atoms according to their species. For example, v_o^{Fe} is applied if Fe is the moving atom, and so forth. The second approach employs the v_o^{alloy} as described in Eq. (4.8) for the entire alloy system. Both strategies yielded comparable results in terms of the total diffusion coefficients, which is the primary focus in this work. Consequently, the second approach (Eq. (4.8)) is adapted due to its simplicity in the KMC modeling.

Using the v_o^{alloy} from Eq. (4.8), the vacancy diffusivities in the equiatomic FeNiCrCoCu HEA, and the five quaternary equiatomic sub-systems were calculated from the ANN-KMC simulations from 1600 K to 2000 K, with an interval of 100 K. To validate the ANN-KMC model,

diffusivities were also calculated by the independent MD simulations in these alloys. Figure 4.8 shows a complete comparison of the results between ANN-KMC and MD using Arrhenius treatments in the temperature range from 1600 K to 2000 K. The error bar for each diffusivity data indicates the standard deviation derived from six independent simulations in ANN-KMC or four independent simulations in MD. The activation energies for diffusion are extracted for both ANN-KMC and MD results, as indicated in each sub-figure. Overall, the ANN-KMC results agree very well with the independent MD results, in terms of both diffusivities and activation energies, across various alloy systems and temperatures. Slight discrepancies can be seen in two quaternary sub-systems: FeCrCoCu and NiCrCoCu. However, given the fact that the ANN model is trained using the dataset exclusively from the equiatomic five-component FeNiCrCoCu HEA, and the attempt jump frequency (v_o^{alloy}) in the KMC is a weighted sum of pure components (Eq. (4.8)), those small discrepancies are deemed as reasonable and acceptable. Experimentally, HEAs typically do not contain Cu so there are no experimental data to directly compare with our model HEA results. For quaternary HEAs, some experimental self-diffusivity data are available for the equiatomic FeNiCrCo HEA [112]. Since the EAM potential predicts a different melting temperature from the realistic HEA, here only the comparison of the activation energy is made. The self-diffusion activation energy of the FeNiCrCo HEA is about 280 kJ/mol in experiment, which is comparable to 295 kJ/mol obtained in this modeling work. Note to compare the self-diffusion activation energy, the mean vacancy formation energy of 1.62 eV or 156 kJ/mol is added to the vacancy diffusion activation energy shown in Fig. 4.8, because the vacancy in our simulations is pre-created. For individual components, their activation energies are also comparable between experiments and this modeling work, although the order among the components has some discrepancies. Similar

observation was also found in Seoane et al.'s work [21]. Overall, the model HEA system used in this work captures many essential features of realistic HEAs such as single FCC phase, complex PEL, and variation in component diffusivities. Therefore, it is expected that the scientific conclusions obtained from this model HEA can be generalized to many realistic HEA systems.

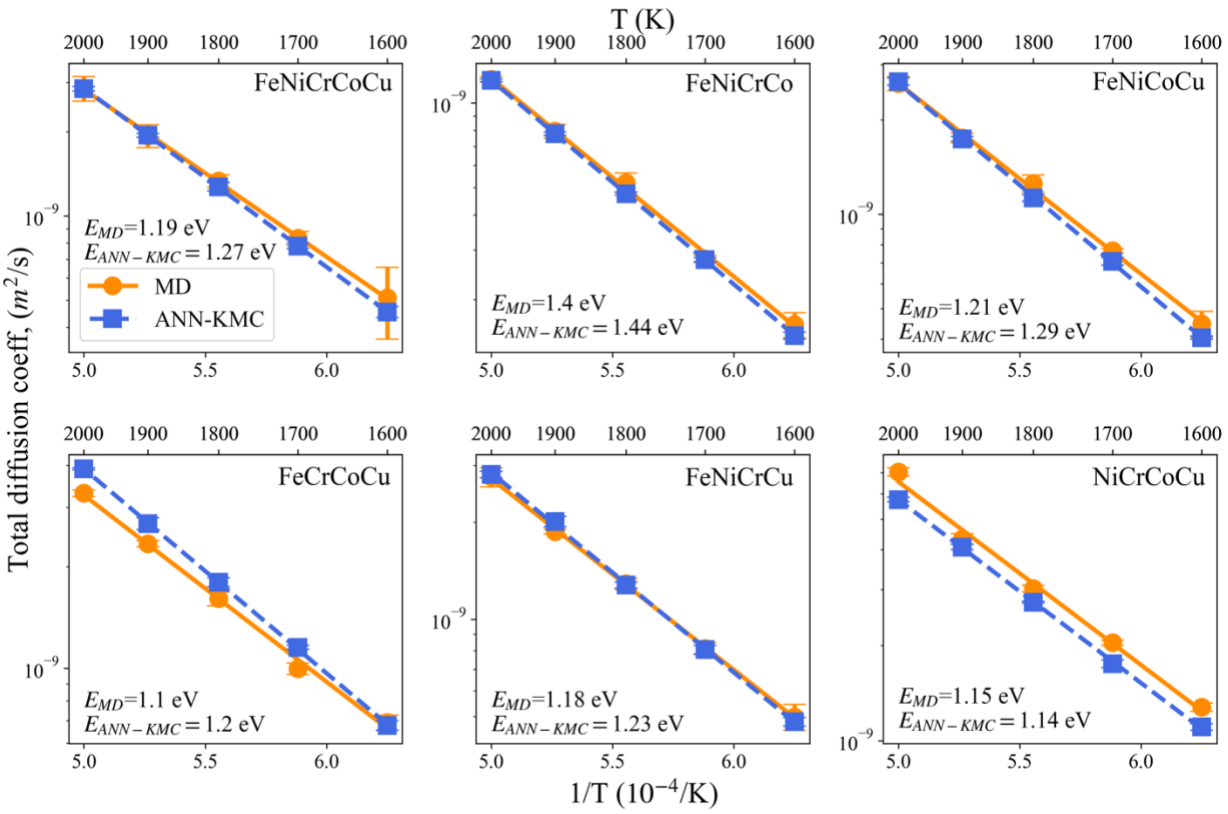

Fig. 4.8. Arrhenius plots of vacancy diffusion coefficients for the equiatomic FeNiCrCoCu HEA and its five equiatomic quaternary alloys obtained from ANN-KMC and MD simulations in the temperature range from 1600 to 2000 K.

One challenge in determining if diffusion is "sluggish" in HEAs or concentrated alloys arises from the absence of a universal criterion. For example, Daw and Chandross proposed four different criteria and each of them can be used to define sluggish diffusion [113]. Experimentally, the HEA diffusivities were typically compared with those of pure components or simpler alloys to determine if the diffusion is sluggish [12, 114]. However, such comparisons might not be very fair because a HEA is a very different material from its pure components or simpler alloys. As mentioned earlier, in this work a “sluggish diffusion” is determined if the diffusivity in an alloy is slower than the counterpart predicted by the average-atom (AA) model [100], similar to our previous work [21, 98]. This criterion is similar as comparing with the rule of mixture of the diffusivities of pure components [21], which is one of Daw et al.’s criteria [113]. The AA model is an EAM potential for a hypothetical single element. It predicts the average bulk properties nearly identical as the HEA while it does not have HEA’s compositional complexity. For example, Seoane et al. [21] reported that an AA material predicts similar lattice constant, elastic constants, vacancy formation and migration energies as the average values in an equiatomic FeNiCrCoCu HEA. Therefore, using the AA material as the reference can isolate the effect of HEA’s inherent chemical disorder and elucidate if such an effect leads to a sluggish diffusion. It should be noted that such a comparison is only achievable through computer modeling because a hypothetical AA material does not exist experimentally. However, each HEA composition requires a distinct AA EAM potential. Therefore, it is impractical to develop numerous AA models for the vast non-equiatomic HEA compositional space. To tackle this challenge, another high-throughput method, termed as AA-KMC, is developed in this work to approximate the diffusion properties in AA materials. Based on the definition of the AA material [100], this approach sets the vacancy

migration barrier in the AA-KMC modeling the same as the mean migration barrier of its corresponding HEA to substitute developing an AA EAM potential. By utilizing our well-trained ANN model (Section 4.3.1), the static migration barrier distribution and its mean in a HEA of any composition can be easily obtained, without the need of conducting computationally expensive NEB calculations. Subsequently, conventional KMC modeling can be conducted to calculate the diffusivities for AA materials, using the same jump attempt frequency v_o^{alloy} as described in Eq. (4.8).

To validate the AA-KMC approach, Figure 4.9 presents the diffusivities and activation energies obtained from the AA-KMC calculations and the independent MD counterparts using the AA EAM potential. The corresponding ANN-KMC and MD diffusivity data for the equiatomic FeNiCrCoCu HEA are also shown for comparison, which are the same as those shown in the first sub-figure of Fig. 4.8. It is evident that the AA-KMC method yields diffusivities nearly identical to the independent MD results based on the corresponding AA EAM potential, demonstrating the feasibility of the AA-KMC method. Consistent with our previous results that are solely based on MD simulations [21], the comparison between the HEA and AA material (regardless via MD or KMC) confirms the absence of vacancy-mediated sluggish diffusion in the equiatomic FeNiCrCoCu HEA, which is also consistent with experimental observations [11].

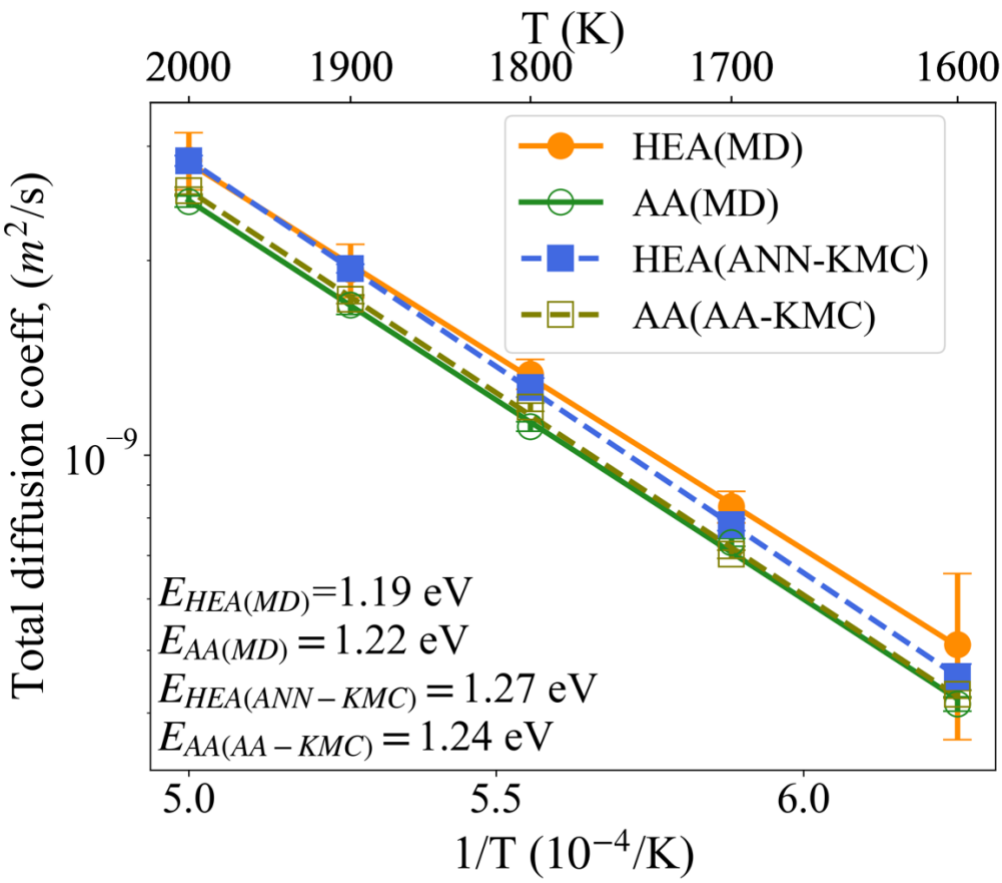

Fig. 4.9. Arrhenius plots of the vacancy-mediated diffusivities for the equiatomic FeNiCrCoCu HEA and its corresponding AA material using MD, ANN-KMC, and AA-KMC simulations at the temperatures ranging from 1600 K to 2000 K.

4.3.3 Percolation effects of fastest diffuser – Cu

Osetsky et al. [16, 99] argued that the faster diffuser in the binary Ni-Fe alloys, Fe, can cause a local trapping effect when its concentration is below the percolation threshold in an FCC crystal, 20 at.%. As a result, the total diffusivity reaches a minimum at this threshold. To

investigate if such a percolation effect also exists in HEAs, a series of non-equiatomic FeNiCrCoCu alloys were prepared in which the concentration of the fastest-diffusing species (i.e., Cu) was varied from x = 0 – 30 at.% with an interval of 5 at.% and the other four components were in equiatomic ratios, denoted as $(FeNiCrCo)_{100-x}Cu_x$. An additional x = 1 at.% of Cu composition is also studied. Figure 4.10(a) shows the total diffusion coefficients of $(FeNiCrCo)_{100-x}Cu_x$ and its corresponding AA materials, as determined by MD, ANN-KMC, and AA-KMC simulations at 1800 K. Here the AA EAM potentials for those $(FeNiCrCo)_{100-x}Cu_x$ HEAs were developed based on the method described in [100]. Again, there is good agreement between ANN-KMC and MD results for HEAs over the entire Cu concentrations, as well as between AA-KMC and MD results for AA materials. Notably, both HEA and AA materials exhibit a monotonic and nearly linear increase in diffusivity with the increasing Cu concentration, indicating that the percolation threshold (x = 20 at.%) does not guarantee the slowest diffusivity in the $(FeNiCrCo)_{100-x}Cu_x$. This is consistent with the observation found in the ternary CoCrNi alloy [17]. However, when compared with AA materials, HEAs show marginally slower diffusivities at 1800 K when the Cu concentration is ≤ 15 at.%, indicating the presence of sluggish diffusion according to the criterion discussed in the previous section. Figure 4.10(b) presents the total diffusivity for the same systems obtained from ANN-KMC and its corresponding AA-KMC at 900 K. Since MD cannot provide reliable diffusivity calculations at this low temperature, no MD results were obtained for HEAs or AA materials. At 900 K, the slower diffusivities in HEAs compared to AA materials become more evident with the decreasing Cu concentration, suggesting that the local trapping effects by Cu are more pronounced at lower temperatures. The results also demonstrate the necessity of using low-temperature simulations to magnify the presence of sluggish diffusion in this HEA system,

consistent with an experimental study in which the sluggish diffusion in an FeNiCrCoMn HEA grain boundary is more evident at low temperatures [115]. These observations suggest a competitive interplay between the local trapping effect and the enhanced total diffusivity due to the incorporation of the fastest diffuser – Cu. However, unlike in the binary Ni-Fe system [16, 99], the competition does not lead to a diffusivity minimum, probably because Cu diffusivity is a few orders of magnitude faster than other components (Fig. 4.7(a)) so that the diffusion enhancement overpowers the local trapping effect.

Figures 4.11 and 4.12 illustrate several key diffusion factors for studying the underlying diffusion mechanisms in $(FeNiCrCo)_{100-x}Cu_x$. Figure 4.11(a) showcases the migration barriers of AA materials at different Cu concentrations using NEB calculations based on the EAM potentials, alongside the mean migration barriers of HEAs predicted by the ANN model. To obtain the latter, a vacancy was sequentially created at each lattice site in a HEA and a random migration path was chosen from the twelve nearest neighboring atoms of the vacancy. The migration barrier was then predicted by the ANN model based on the LAC around the migration path. Repeating this process, 4000 migration barriers in each HEA were obtained and the mean value is reported in Fig. 4.11(a). The figure shows that the average migration barrier of each non-equiatomic HEA closely resembles the migration barrier of the corresponding AA material, further validating the assumption of the migration barrier in the AA-KMC method. Also, a noticeable decrease in the migration barrier for both HEA and AA is observed as the Cu concentration increases, consistent with the inverse trend of the diffusivity in Fig. 4.10. Figure 4.11(b) demonstrates the absolute jump fraction by each species at 1800 K. When Cu concentration is 1 at.%, its jump fraction is already large (~15%) but does not dominate. When Cu concentration is 5 at.%, its jump fraction becomes

the largest among other components, nearly 50%. As the Cu concentration increases further, it increasingly dominates the vacancy jumps, such as over 80% in $(FeNiCrCo)_{70}Cu_{30}$. Figure 4.11(c) shows the normalized jump ratios of the HEA components with respect to their compositions at different Cu concentrations at 1800 K. Clearly, the fastest diffusing species (Cu) "over-jumps" significantly with respect to its composition, and the over-jump ratio increases with the decreasing Cu concentration. Again, the result demonstrates that the vacancy prefers to exchange with the fastest-diffusing species. If many of such preferential jumps are back-and-forth ones, they can lead to a local trapping effect.

The correlation factor for diffusion ($0 \leq f_c \leq 1$) is a useful parameter to characterize if the defect jumps lead to a local trapping effect (small f_c) or a long-range diffusion (large f_c). Here the correlation factor for each species in a HEA is calculated using the formula [17],

$$f_c^X = \frac{ASD_X}{N_X \Delta^2}, \tag{4.9}$$

where ASD_X and N_X are the ASD and the number of jumps of the species X in a HEA, respectively, and Δ is the vacancy jump distance (the 1st nearest neighbor distance). The same equation is also used to calculate the correlation factors in the entire HEAs (f_c^{HEA}) and AA materials (f_c^{AA}) during the ANN-KMC and AA-KMC simulations. Figure 4.12 shows the calculated correlation factors as a function of Cu concentration at 1800 K and 900 K, respectively. At both temperatures, the correlation factor for the single-component AA material is $f_c^{AA} \approx 0.78$ at all Cu concentrations, which is in excellent agreement with the theoretical value of 0.78146 for a 3D vacancy diffusion in a pure FCC crystal [116]. On the other hand, f_c^{HEA} is significantly lower than f_c^{AA}, suggesting

that the vacancy jumps in HEAs can result in a trapping effect due to their rough PEL. For the five components in the HEAs, their correlation factors reversely correspond to their pure-component diffusivities (Fig. 4.7(a)), namely, a component with a lower diffusivity yields a higher correlation factor. Furthermore, the addition of Cu leads to a slight increase in the correlation factor for the other four components. At all Cu concentrations, the Cu correlation factor is very low, implying its strongest ability to interchange with the vacancy and many of them are back and forth jumps, thus potentially creating local traps. In terms of temperature effect, the Cu correlation factor at 900 K (Fig. 4.12(b)) is much lower than that at 1800 K (Fig. 4.12(a)). This result indicates that the local trapping effect by Cu is stronger at low temperatures, consistent with the more pronounced sluggish diffusion at 900 K than at 1800 K (Fig. 4.10). As previously discussed, due to the significantly higher diffusivity of Cu, the effect of diffusion enhancement likely predominates over localized trapping effects. The overall correlation factor of the HEA has its lowest value at the equiatomic composition (i.e., 20 at.% Cu), which could be attributed to the maximum compositional complexity at this composition. However, it is observed that such compositional complexity does not directly impact the total diffusivity in the equiatomic HEA in comparison with its AA counterpart as they yield similar diffusivities at this composition.

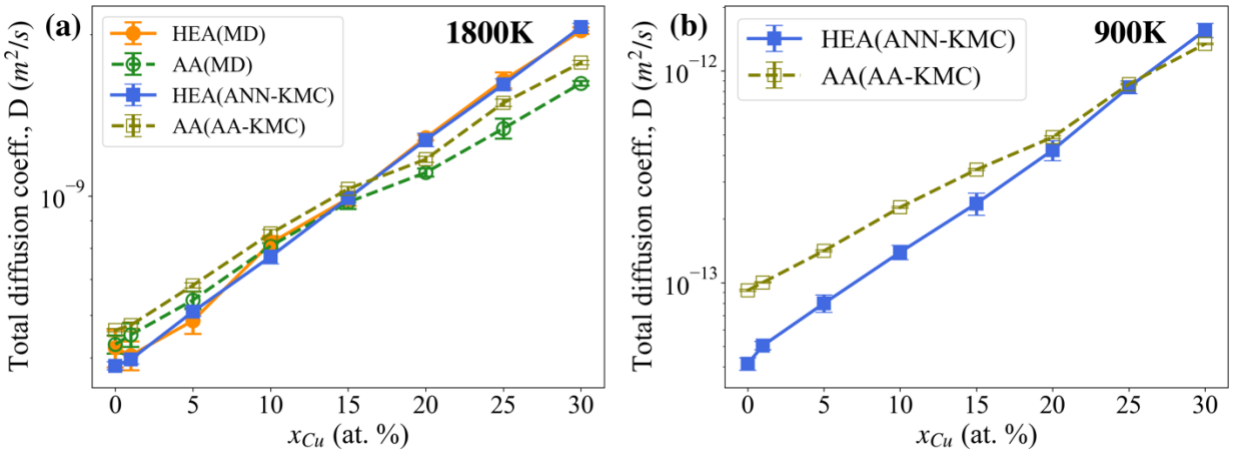

Fig. 4.10. Total diffusivities of $(FeNiCrCo)_{100-x}Cu_x$ and AA materials at different Cu concentrations, (a) determined by MD, ANN-KMC, and AA-KMC simulations at 1800 K, and (b) determined by ANN-KMC and AA-KMC simulations at 900 K.

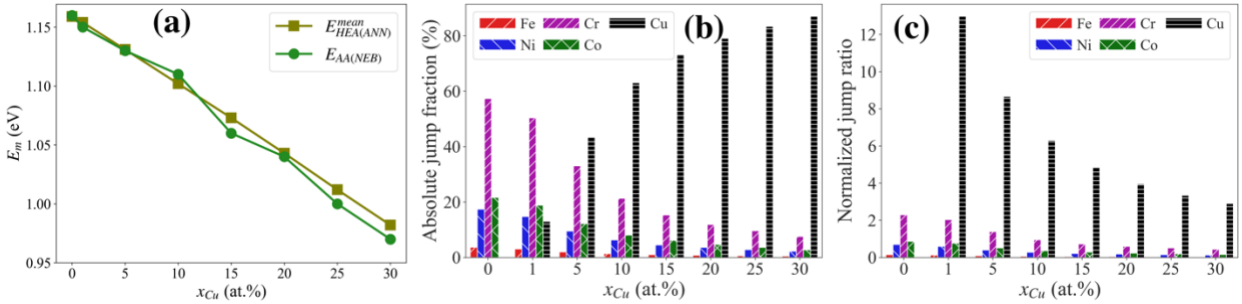

Fig. 4.11. Diffusion governing factors in the $(FeNiCrCo)_{100-x}Cu_x$ HEAs and AA materials: (a) migration barriers of AA materials (by NEB) and mean migration barriers of HEAs (by ANN), (b) absolute jump fractions of individual components at 1800 K, and (c) normalized jump ratios of individual components with respect to their compositions at 1800 K.

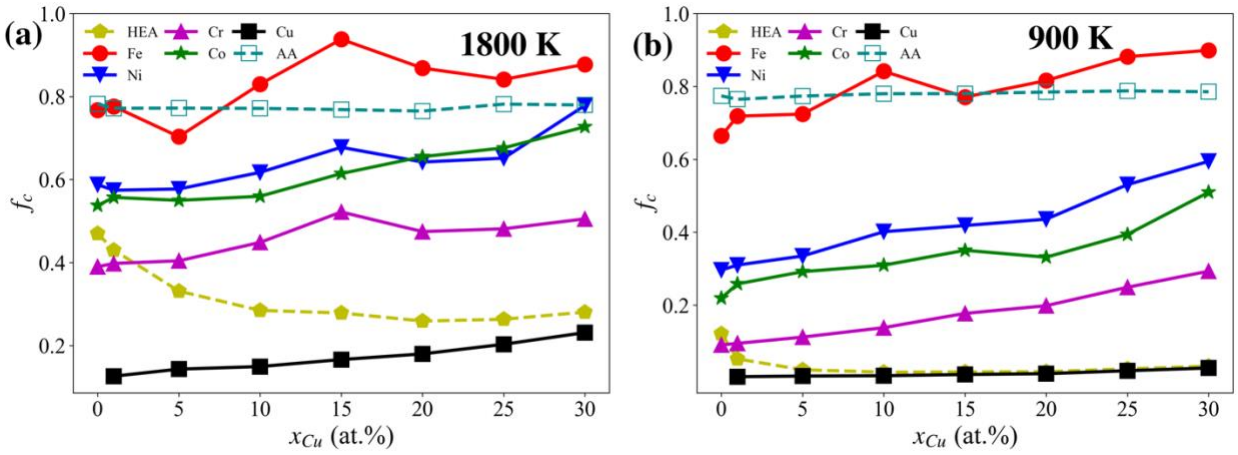

Fig. 4.12. Total and elemental correlation factors at (a) 1800 K and (b) 900 K.

4.3.4 High-throughput investigation of the vast compositional space of HEAs

The results presented in the previous sections have demonstrated the reliability of the ANN-KMC and AA-KMC methods, and revealed the existence of sluggish diffusion in non-equiatomic HEAs as Cu concentration varies, especially at a low temperature of 900 K. Therefore, the two methods are used to further explore the more diverse compositional space of HEAs and search for those exhibiting greater degrees of sluggish diffusion at 900 K. To achieve this, the concentrations of all five species were randomly varied with a 5 at.% interval to create 1,500 unique non-equiatomic HEAs (e.g., $Fe_{25}Ni_{15}Cr_{50}Co_5Cu_5$), each of these HEAs has the same system size as the equiatomic HEA. Taking advantage of the well-trained ANN model, the static migration barrier distribution for each HEA composition is obtained using the same way as that for obtaining the mean barriers in Fig. 4.11(a). From the distribution, its mean barrier ($\mu_{E_m}^{static}$) and standard deviation ($\sigma_{E_m}^{static}$) can be obtained, with the former ($\mu_{E_m}^{static}$) employed for AA-KMC simulations.

In addition, during an ANN-KMC simulation, the executed vacancy hops and their corresponding migration barriers were recorded, resulting in a dynamic barrier distribution with its respective mean ($\mu_{E_m}^{dynamic}$) and standard deviation ($\sigma_{E_m}^{dynamic}$).

Figures 4.13(a) and (b) show the diffusivities for those 1,500 HEA compositions at 900 K calculated from ANN-KMC simulations, in relation to $\mu_{E_m}^{static}$ and $\sigma_{E_m}^{static}$, as well as $\mu_{E_m}^{dynamic}$ and $\sigma_{E_m}^{dynamic}$, respectively. Here two types of sluggish diffusion are categorized: "strong" sluggish diffusion if the HEA diffusivity is more than one order of magnitude slower than its AA counterpart (i.e., $D_{HEA} < \frac{1}{10} D_{AA}$), and "mild" sluggish diffusion if the HEA diffusivity is slower than at least half of its AA counterpart (i.e., $\frac{1}{10} D_{AA} < D_{HEA} < \frac{1}{2} D_{AA}$). Note here if the HEA diffusivity is only slightly lower than its AA counterpart (i.e., $\frac{1}{2} D_{AA} < D_{HEA} < D_{AA}$), it is not considered as sluggish because the AA-KMC method could exhibit some uncertainties in calculating the AA diffusivities. This treatment increases the comparison margin and reduces the uncertainties in identifying the sluggish compositions. It should be noted that the above definitions of strong and mild sluggish diffusion are somewhat arbitrary. However, the main conclusions of this study remain unchanged if these thresholds are modified slightly, e.g., defining strong sluggish as $D_{HEA} < \frac{1}{5} D_{AA}$. While many HEAs show mild sluggish diffusion, six HEAs display strong sluggish diffusion: $Fe_{60}Ni_5Cr_{20}Co_{10}Cu_5$, $Fe_{60}Ni_{20}Cr_5Co_{10}Cu_5$, $Fe_{60}Ni_5Cr_5Co_{10}Cu_{20}$, $Fe_{60}Ni_{25}Cr_5Co_5Cu_5$, $Fe_{55}Ni_5Cr_{10}Co_5Cu_{25}$, and $Fe_{45}Ni_{20}Cr_{10}Co_{20}Cu_5$, as marked by red circles in Fig. 4.13. In Fig. 4.7(a), the diffusivity order of pure components is: Fe < Ni < Co ≈ Cr < Cu. Therefore, these strong sluggish HEAs generally contain a high concentration of slowest-diffusing species,

Fe. In terms of the sum of the two slowest species (Fe + Ni), it exceeds 60% in all cases. Figure 4.13(a) also reveals that these sluggish HEAs (both strong and mild) possess a relatively higher $\mu_{E_m}^{static}$. However, the $\sigma_{E_m}^{static}$ does not exhibit a clear influence on diffusivity, as the sluggish HEAs have both large and moderate $\sigma_{E_m}^{static}$. This observation suggests that the variations in static migration barriers is not critical in shaping the diffusion behavior, in agreement with the previous study [22]. Conversely, Figure 4.13(b) shows a different trend, where a sluggish HEA generally has a larger $\sigma_{E_m}^{dynamic}$ while its $\mu_{E_m}^{dynamic}$ spans from low to moderate. In particular for the 4 out of 6 strong sluggish HEAs, their $\sigma_{E_m}^{dynamic}$ are extremely large. The higher $\sigma_{E_m}^{dynamic}$ indicates a greater variation in the executed migration barriers in a HEA. This variation could result in regions with both low and high migration barriers that act as traps for diffusing atoms. In this scenario, either vacancy hops via high-energy barrier sites could occur, or the likelihood of localized back-and-forth hops via low-energy barriers may increase, ultimately leading to a reduction in the overall diffusivity.

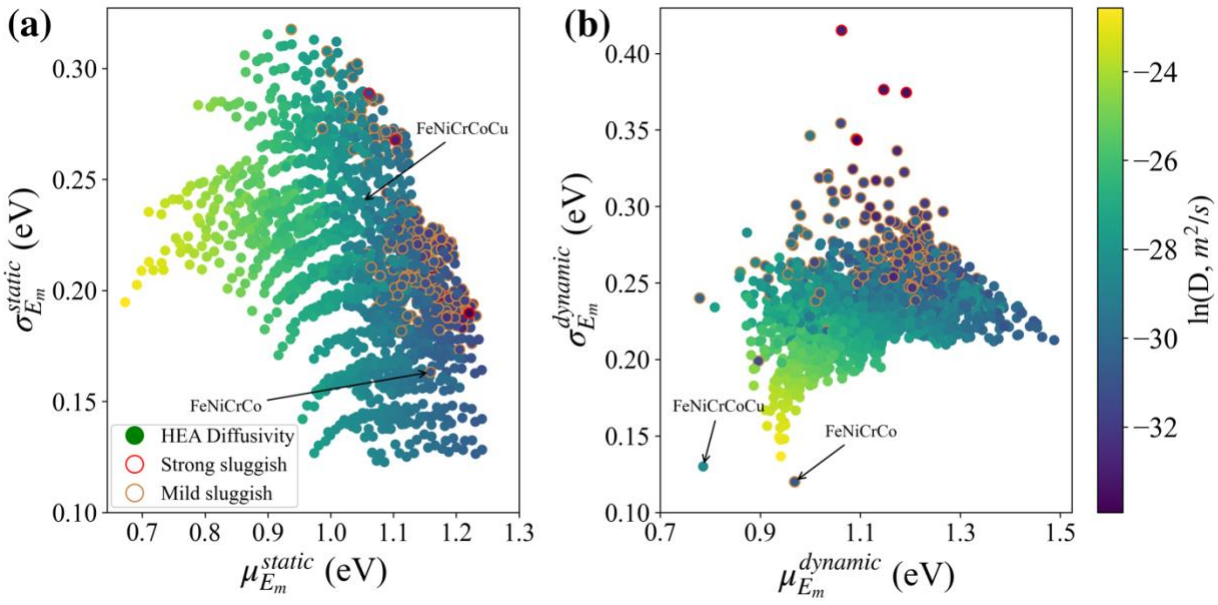

Fig. 4.13. Diffusivities of 1,500 unique non-equiatomic HEA compositions calculated by ANN-KMC at 900 K in relation to (a) $\mu_{E_m}^{static}$ and $\sigma_{E_m}^{static}$, and (b) $\mu_{E_m}^{dynamic}$ and $\sigma_{E_m}^{dynamic}$. The color of each filled circle indicates the magnitude of diffusivity. HEAs exhibiting sluggish diffusion with respect to their AA counterparts are classified as strong ($D_{HEA} < \frac{1}{10} D_{AA}$, red circle line) or mild ($\frac{1}{10} D_{AA} < D_{HEA} < \frac{1}{2} D_{AA}$, orange circle line) degree, respectively.

In prolonged diffusion scenarios, short-range orders (SROs) may develop and impact the diffusion behavior [102]. Evidence from both our recent work and other studies have demonstrated that SROs can introduce extra trapping effects and further slower the diffusion [48, 104]. However, in this study, the utilized EAM potential, characterized by its low heat of mixing, ensures that the tendency of chemical ordering remains minimal even after long-time KMC simulations. To

provide a quantitative assessment of the possible SROs development, the Warren-Cowley parameter [55] for each pair of elements is computed, as defined by

$$\alpha_k^{ij} = 1 - \frac{\langle N_k^{ij} \rangle}{c_j N_k}, \tag{4.10}$$

where *i* and *j* represent i^{th}-type and j^{th}-type of elements (e.g., Fe, Cr), *k* represents the k^{th} nearest-neighbor shell, $\langle N_k^{ij} \rangle$ represents the average number of j^{th}-type atoms surrounding i^{th}-type atoms at its k^{th}-nearest-neighbor shell, N_k is the total number of atoms in the k^{th} nearest-neighbor shell, and c_j is the concentration of j^{th}-type atoms in the entire system. α_k^{ij} should approach zero in a random solid-solution alloy, while a negative value means favorable *i-j* pair formation and vice versa. As an illustrative example, the SRO values at the 1st nearest-neighbor shell for the $Fe_{55}Ni_5Cr_{10}Co_5Cu_{25}$ before and after 300,000 KMC steps are shown in Figs. 4.14(a) and (b), respectively, which exhibits strong sluggish diffusion in Fig. 4.13. Clearly, the SRO values for most of elemental pairs in the initial structure (Fig. 4.14(a)) are close to zero, indicating the initial atomic configuration is random. The SRO value for the Co-Co pair deviates from zero slightly, possibly due to insufficient statistics from its low concentration (5 at.%). After the KMC simulation (Fig. 4.14(b)), the SRO values only change slightly for these pairs, confirming that an extended KMC simulation does not introduce significant SROs. This finding suggests that the trapping effect discussed here is not significantly impacted by SROs.

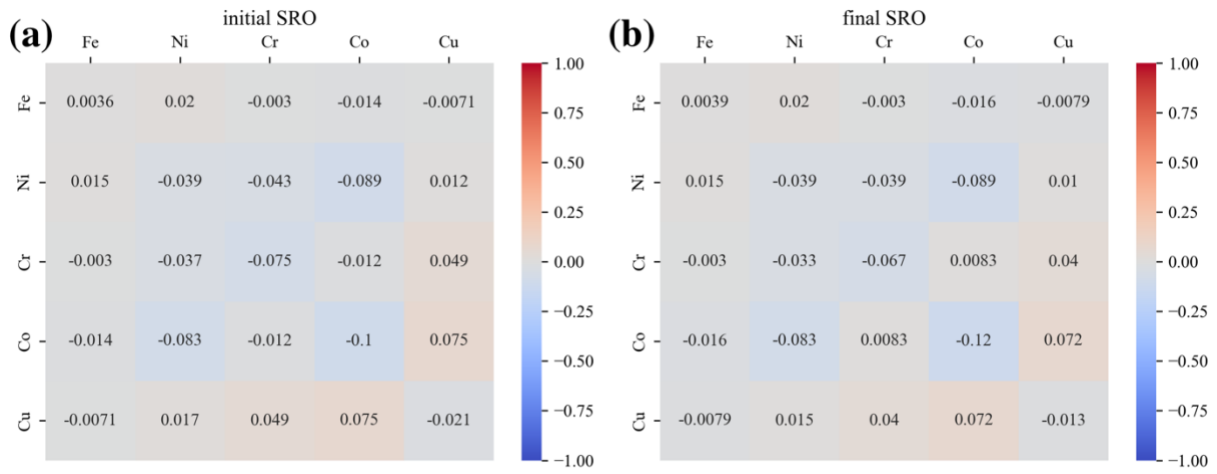

Fig. 4.14. Warren-Cowley SRO parameters of all element pairs in the $Fe_{55}Ni_5Cr_{10}Co_5Cu_{25}$ alloy for the (a) initial structure, and (b) final structure after 300,000 KMC steps at 900 K. Note this alloy shows a strong sluggish diffusion in Fig. 4.13.

4.4. Discussion

Molecular dynamics (MD) offers a wealth of advantages for studying diffusion properties in alloys, granting atomic-scale insights into the complex diffusion mechanisms in HEAs. However, it is computationally expensive for exploring the extensive compositional space in HEAs. Moreover, MD simulations are limited to high temperatures and short timescales, which pose challenges for exploring the complex potential energy landscape (PEL) in HEAs. Theoretical models, such as random barrier/trap (RB/RT) model or continuous-time random walk model [117, 118], are unable to accurately describe the complex PEL in HEAs. On-the-fly off-lattice KMC method [16] is able to explore the complex PEL in concentrated alloys, but it is computationally

expensive because the migration barriers need to be dynamically calculated at every step. In this regard, the coupling of machine learning (ML) with KMC as used in this work presents a promising solution for studying the complex diffusion problems in HEAs, in which the well-trained ANN-based ML model is able to capture the non-linear dependency of PEL on local atomic configurations (LACs). As such, there has been growing interest in employing ML for similar purposes in concentrated alloys [29, 119-121]. While some ML-based studies have achieved promising accuracies in predicting the vacancy migration barriers for a specific HEA composition, generalizing these ML models to other HEA compositions or their subsystems remains challenging. This limitation leads to a dilemma where one must either collect extensive datasets encompassing various compositions or build separate ML models for each composition. The present work shows that it is possible to use a small dataset (e.g., equiatomic composition) as the training data and use the trained ANN model to predict other compositions (e.g., non-equiatomic compositions and sub-systems). The performance of a ML model is highly dependent on the quality of dataset and the choice of descriptors. In this study, the ANN model performance was systematically assessed with respect to the number of nearest neighboring (NN) shells used for constructing LACs, as shown in Fig. 4.2. While the ANN model presented here is built using LACs surrounding the vacancy-migration atom pair up to the third NN shells, it should be noted that our ANN model can still achieve an acceptable MAE of 47 meV and 42 meV when considering only the first NN atoms or up to the second NN atoms, respectively. Therefore, this approach could be extended to other smaller-size systems such as those for density functional theory (DFT) calculations, which typically have less than two hundred atoms. However, more work is needed in the future to determine if the advantages (e.g., small dataset and fewer NN shells for training) of our ANN

model can be applied to other HEA systems. In particular, this HEA model system predicts the stable FCC phase for a wide range of random solid-solution compositions. In some aluminum (Al) containing HEAs, multiple phases can coexist [106]. Applying the ANN model developed in this work for such complex systems would be challenging. Nevertheless, it is expected that the LAC-ANN model developed in this work can be extended to some other HEA systems with DFT-calculated migration barriers. If a good DFT-ANN-KMC model can be developed, the development of EAM potentials is no longer necessary and the migration barriers may be more accurate than those obtained from interatomic potentials. In turn, the calculated diffusivities could be more comparable with experiments.

To test how the calculated diffusivity is sensitive to the accuracy of the ANN model, three "artificial" ANN models are constructed by introducing Gaussian noises with a mean of zero and varying standard deviations (0.1, 0.2, and 0.3 eV). This treatment widens the deviation in ANN predictions while keeping the mean migration barrier nearly unchanged, as indicated by the red linear regression lines in Figure 4.15(a-d). Figure 4.15(b-d) contrasts the performance of the three artificial ANN models with the actual model (Fig. 4.15(a)), as the MAE value increases from the original 31.9 meV to 85.7, 163.3, and 244.3 meV, respectively. These modified ANNs are coupled with KMC to calculate the diffusivities of the equiatomic FeNiCrCoCu at different temperatures, and the results are compared with the original model, as shown in Fig. 4.15(e-h). Notably, as seen in Fig. 4.15(f), even with a relatively large MAE of 85.7 meV (artificial-1), the ANN-KMC model still agrees reasonably well with the independent MD results. It should be noted that this artificial MAE is much larger than all of those in the actual quinary and quaternary systems (Figs. 4.3-4), which are used for diffusivity calculations. Although it is close to those in a few ternary and binary

compositions (Figs. 4.5-6), they are not used for any diffusivity calculations in this work. Therefore, the small MAEs in the ANN models for the quinary and quaternary systems should not significantly affect the accuracy of predicted diffusivities. However, if amplified errors are introduced (artificial-2 and artificial-3), the predicted diffusivities notably deviate from the MD data even though the mean migration barrier is similar. This sensitivity analysis demonstrates the risk of using the mean migration barrier in the conventional KMC simulations for HEAs while ignoring its variance, which is a common practice in literature but could yield inaccurate results.

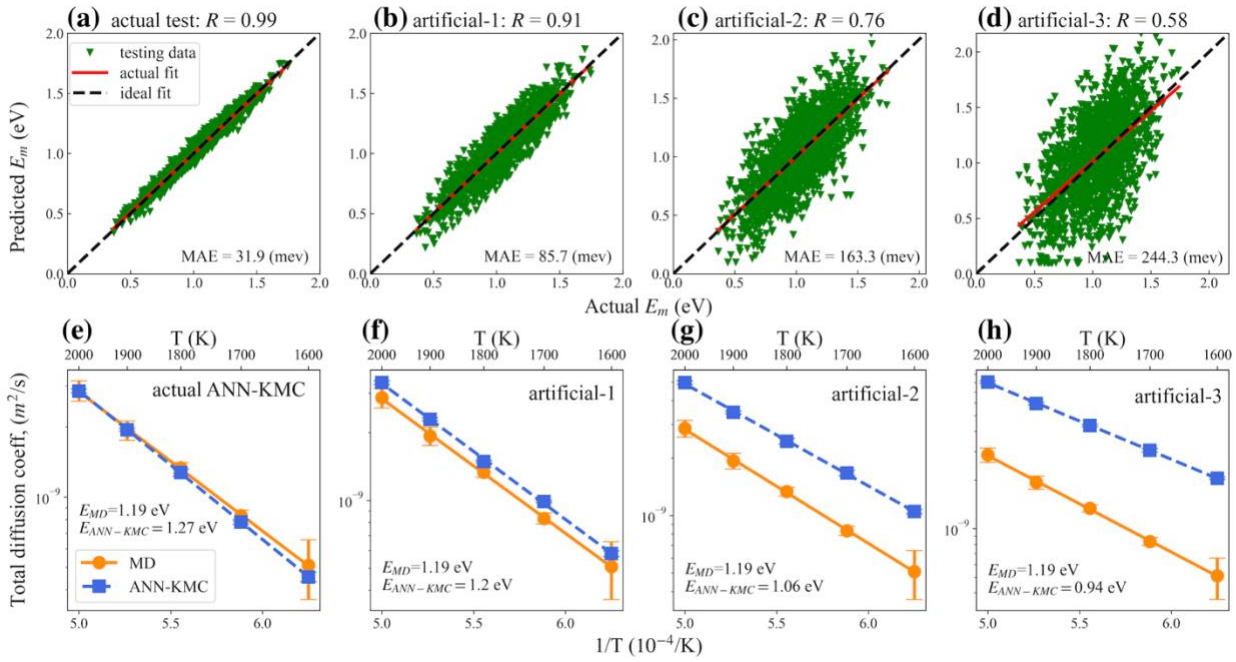

Fig. 4.15. (a) - (d) Performance comparison of the actual ANN model with three "artificial" ANN models for the equiatomic FeNiCrCoCu, constructed with Gaussian noises with a mean value of zero and varying standard deviations (0.1, 0.2, and 0.3 eV). (e) - (h) ANN-KMC calculated diffusivities using the actual and three artificial ANN models at different temperatures. The same set of MD data is shown in each sub-figure as a reference.

In this work, the determination of sluggish diffusion is based on the comparison between HEAs and their corresponding AA materials. The comparison aims to isolate the effect of compositional complexity in HEAs and understand how it influences the diffusion behavior, similar as in our previous studies [21, 98]. Building upon prior studies [17, 21] that suggest neither equiatomic compositions nor percolation thresholds guarantee slowest or sluggish diffusion in HEAs, our results also confirm that the equiatomic FeNiCrCoCu HEA exhibits no sign of sluggishness when compared to its AA counterpart, as demonstrated in Fig. 4.9. While the percolation threshold of the fastest diffuser does not yield the sluggish diffusion in the $(FeNiCrCo)_{100-x}Cu_x$ HEAs, they can be deemed as sluggish when Cu concentration is below the percolation threshold (< 20 at.% Cu). The sluggish effect becomes more evident at low temperatures (e.g., 900 K). Although the sluggish diffusion is observed as compared to AA counterparts, the overall diffusivity in the $(FeNiCrCo)_{100-x}Cu_x$ HEAs increases with the increasing Cu concentration (Fig. 4.10(b)), which seems contradictory. This could be due to the two competing effects by Cu: trapping and enhanced diffusion. When Cu is not percolated, the back-and-forth exchange (through low migration barriers) between Cu and vacancy can cause a local trapping effect, leading to a sluggish diffusion (in comparison with the AA counterparts). On the other hand, since Cu diffusion is so fast, it can overpower the trapping effect and enhance the total diffusivity (in comparison with 0 at.% Cu composition) as its concentration increases.

This work shows that even though the diffusion in the equiatomic FeNiCrCoCu HEA is not sluggish, the diffusion in non-equiatomic compositions could be sluggish. Therefore, the high-

throughput modeling approach developed in this work is useful for exploring the large composition space and study how the complex PEL influences the diffusion kinetics. For example, Figure 4.13(a) shows that these sluggish HEAs tend to have high average static migration barriers ($\mu_{E_m}^{static}$), while their variances ($\sigma_{E_m}^{static}$) can be either high or moderate; Figure 4.13(b) shows that these sluggish HEAs tend to have large variances ($\sigma_{E_m}^{dynamic}$) in the accepted migration barriers, while their means ($\mu_{E_m}^{dynamic}$) span from low to moderate. The discrepancies between the static and dynamic (accepted) barrier distributions indicate that sluggish diffusion has a complex relationship with HEA composition and thus the PEL. A seemingly rough static PEL (i.e., having large $\sigma_{E_m}^{static}$), which is based on all atomic sites in the system regardless they are visited or not, does not necessarily lead to a sluggish diffusion. This is because a vacancy could find some alternative paths to "bypass" the trapping or high-barrier sites so that those sites may never be visited during the diffusion. On the other hand, if the system consists of effective local trapping sites that a vacancy cannot escape easily, such as some low-barrier sites enclosed by high-barrier sites, the sluggish diffusion effect could be strong. In such case, the dynamic PEL should have large $\sigma_{E_m}^{dynamic}$.

In Section 4.3.4, six compositions exhibiting strong sluggish diffusion (at least 10 times slower than the AA counterpart) have been identified. The general trend is that they contain high concentrations of slowest diffusing species (Fe and Ni) and low concentrations of fastest diffusing species (Cu). To check if the mild sluggish diffusion ($\frac{1}{10}D_{AA} < D_{HEA} < \frac{1}{2}D_{AA}$) also follows the same trend, Figure 4.16 shows a 3-D plot of the diffusion behavior with respect to Cu, Ni, and Fe concentrations. Clearly, the majority of the sluggish compositions contain less than 10 at.%Cu but

more than 40 at.%Fe. It should be noted that this composition analysis is consistent with Fig. 4.13. When the system contains more slow diffusing species such as Fe and Ni, the mean static barrier ($\mu_{E_m}^{static}$) will be high, consistent with Fig. 4.13(a). On the other hand, if the system contains a small amount of fast diffusing species such as Cu, the fast diffuser may form non-percolated local traps and thus increase the variances of the accepted barriers ($\sigma_{E_m}^{dynamic}$), consistent with Fig. 4.13(b). The results from this work could provide some useful insight for experimental alloy design. To design a HEA with sluggish diffusion, our suggestion is that the alloy should contain high-concentration slow diffusing species and low-concentration fast diffusing species. However, the fast diffuser should not be as fast as Cu to avoid the predominance of its diffusion enhancement over its local trapping effect. If the fast diffuser can form some non-percolated local precipitates due to its low solubility, the local trapping effect and thus the sluggish diffusion could be even stronger. Of course, these suggested alloy design guidelines need to be experimentally validated by the research community in the future.

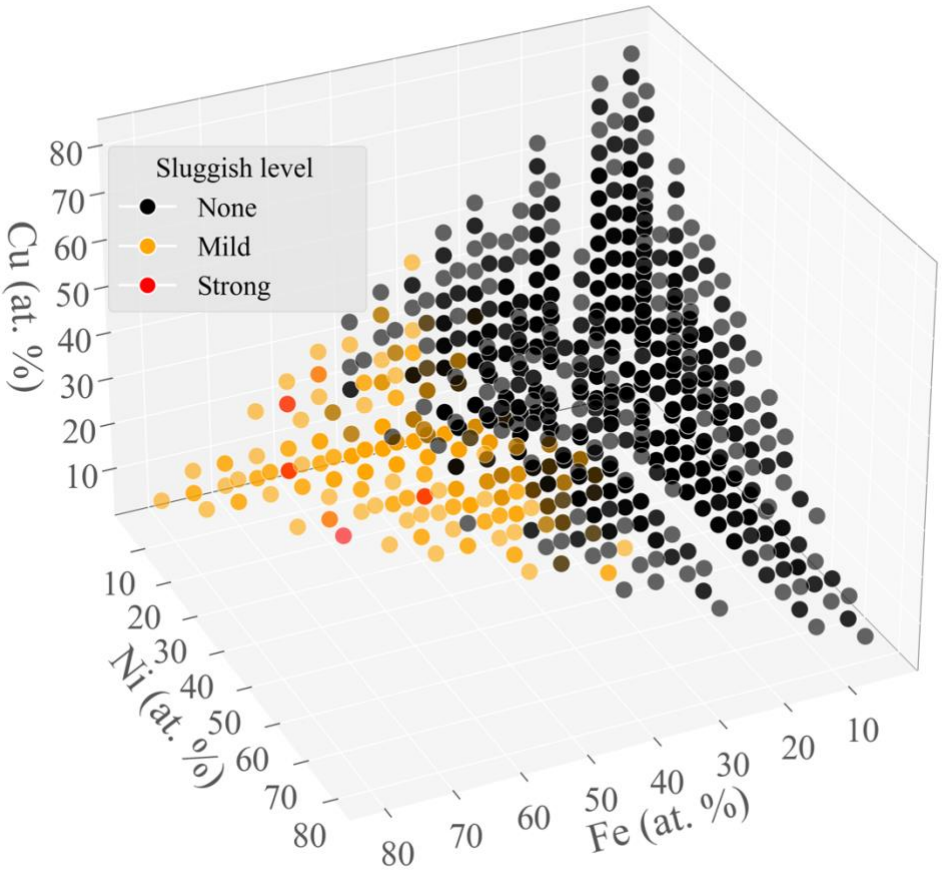

Fig. 4.16. Relation between the diffusion behavior in 1500 non-equiatomic HEA compositions with faster diffuser Cu, and slower diffuser (Ni, Fe) concentrations. Here strong sluggish ($D_{HEA} < \frac{1}{10} D_{AA}$), mild sluggish ($\frac{1}{10} D_{AA} < D_{HEA} < \frac{1}{2} D_{AA}$), and non-sluggish ($D_{HEA} > \frac{1}{2} D_{AA}$) compositions are represented by red, orange, and black filled circles, respectively.

4.5. Conclusions

- *A high-throughput machine learning informed KMC modeling framework has been developed to study the possible sluggish vacancy diffusion in a wide range of FeNiCrCoCu HEA compositions*

In this work, an innovative artificial neural network (ANN) based machine learning model has been developed to predict local-atomic-configuration (LAC) dependent vacancy migration barriers in a quinary FeNiCrCoCu HEA system. Despite the ANN model being trained solely on the data from the equiatomic HEA, it can predict barriers in many non-equiatomic compositions and its subsystems with a reasonable accuracy. By integrating this ANN model as an on-the-fly barrier calculator for KMC modeling, termed as ANN-KMC in this work, it can calculate vacancy-mediated diffusivities in alignment with independent MD simulations across a range of HEA compositions, but with a much higher efficiency. In addition, a composition- and temperature-dependent jump attempt frequency model has also been developed for KMC modeling of the HEA system. To evaluate the possible existence of sluggish diffusion, the HEA diffusivities are compared to its average atom (AA) counterparts, which describes a hypothetical element having nearly identical bulk properties as the HEA but without HEA's compositional complexity. To avoid the development of a specific AA EAM potential for every HEA composition, a high-throughput AA-KMC model has also been developed, which can predict the vacancy diffusivities comparable with those from independent MD simulations using AA EAM potentials. Using the high-throughput ANN-KMC and AA-KMC methods, the diffusivities in many non-equiatomic HEA compositions have been calculated at a wide range of temperatures and long timescales to search

for the possible sluggish diffusion. It is expected that the high-throughput approaches can be applied to DFT-calculated barriers, enabling the prediction of more accurate diffusivities without the need of developing interatomic potentials for different HEAs.

- *The fastest diffuser (Cu) can lead to both sluggish diffusion due to the local trapping effect and diffusion enhancement due to its fast diffusivity when its concentration is below the percolation threshold*

To study the percolation effects of the fastest-diffuser (Cu) on the overall diffusion behavior in the FeNiCrCoCu HEA system, its concentration was systematically varied from 0 to 30 at.%. It is found that the equiatomic composition or the percolation threshold (20% Cu) in this HEA system does not result in either a minimum diffusivity or sluggish diffusion, which is in stark contrast to the binary Ni-Fe alloy system [16, 99]. Instead, the total diffusivity in the HEA system increases nearly linearly with the increasing Cu concentration. On the other hand, the HEA diffusion is slower than its AA counterpart when the Cu concentration is below its percolation threshold. The seemingly contradictory results suggest a complex interplay between the local trapping effects and enhanced global diffusion due to the incorporating of the ultrafast diffusing element (Cu). The former results in a sluggish diffusion with respect to the AA material when Cu is not percolated and can exchange with vacancy back and forth, while the latter overpowers the local trapping effect and leads to the enhancement of overall diffusivity in comparison to the 0% Cu composition.

- *This work demonstrates that although sluggish diffusion may not exist at the equiatomic composition, it could exist at non-equiatomic compositions. In addition, a rough dynamic migration barrier distribution is more important than a static one for sluggish diffusion*

To search for the sluggish compositions, the diffusivities of 1500 non-equiatomic HEAs and their AA counterparts were calculated by the high-throughput ANN-KMC and AA-KMC, respectively. It is found that many non-equiatomic compositions exhibit sluggish diffusion, and six of them show very strong sluggish diffusion (more than 10 times slower than the AA counterpart). To understand the underlying mechanisms, both static and dynamic migration barrier distributions of the 1500 HEA compositions have been analyzed. The former ones are based on every atomic sites regardless of being visited or not, while the latter ones are only from those accepted migration events during diffusion. A key observation is that the variance in the static migration barrier distribution has a limited influence on diffusion, suggesting that a seemingly rough PEL is not necessary to lead a sluggish diffusion. This is because vacancies may find alternative paths to bypass high-barrier or trapping sites, leaving those sites unvisited during the diffusion. Conversely, it is found that the accepted/executed migration barriers have distinctly large variances in those sluggish compositions. This observation suggests that the effective trapping sites are those with localized low-energy barriers surrounded by high-barrier sites. In such cases, vacancies may perform many back-and-forth hops before they can escape.

- *The results from this work could provide valuable insights for experimental HEA design*

The compositions in these sluggish HEAs have been analyzed in detail (Fig. 4.16). It is found that they typically contain high-concentrations of slowest diffusing species (Fe or Ni in this work) and low-concentrations of fastest diffusing species (Cu in this work). In such cases, the local trapping effect is expected to be strong. These findings may provide useful insights for HEA design. It is

envisioned that the high-throughput modeling framework developed in this work could be used to down-select sluggish compositions first, which can be validated experimentally in the future.

CHARPTER 5 Machine Learning - Kinetic Monte Carlo Simulations of Interstitial Diffusion in FeNiCrCoCu High Entropy Alloys

5.1 Introduction

Recent progresses have been made in understanding the causes of vacancy-mediated sluggish diffusion from binary CSAs to quinary HEAs [16, 17, 21, 22, 104, 122, 123]. For example, Osetsky et al. demonstrated that in Ni-Fe concentrated alloys, the sluggish nature of compositional-dependent vacancy diffusivity primarily arises from the blend effects of site percolation and chemically biased diffusion [16]. Conversely, research on concentrated CoCrNi ternary alloys suggested that the local potential energy landscape, rather than the percolation effect, plays a more critical role in determining the diffusion sluggishness [17]. Therefore, directly extrapolating the knowledge learned from CSAs with fewer components to HEAs may lead to inaccurate interpretations. This conclusion highlights the necessity for a more detailed and targeted research to deepen our understanding of sluggish diffusion in HEAs with at least five components. Interstitial atoms typically exhibit significantly higher diffusivity than vacancies, making their diffusion a crucial factor for the microstructure evolution under irradiation. Both experimental and simulation works have shown that interstitial kinetics are markedly slower in Ni-Fe concentrated alloys compared to their pure components, resulting in delayed interstitial cluster formation and reduced radiation damage [124, 125]. This evidence strongly suggests the presence of sluggish interstitial-mediated diffusion in CSAs. Interstitial-mediated diffusion within alloys typically takes the form of dumbbells, with the specific type of these dumbbells playing crucial role in influencing the diffusion process. There are 15 different types of interstitial dumbbells in a five-component

HEA. This makes interstitial diffusion inherently more complex than vacancy diffusion, and this complexity increases significantly in HEAs due to their varied atomic interactions. Consequently, there is a pressing need for more detailed research to better understand interstitial diffusion mechanisms in HEAs.

In this context, atomistic simulations of interstitials in HEAs can provide valuable insights by directly probing specific micromechanisms of interest. To assess sluggish diffusion effectively, a fair and reliable reference system is needed. A notable point of debate arises in that sluggish diffusion effects are often observed when evaluated on a homologous temperature scale rather than an absolute one [11]. Experimentally, diffusivities in HEAs are often compared to those in their pure components or simpler alloys to determine sluggishness [12, 114]. From a computational standpoint, Daw et al. suggested four types of reference systems, including the use of geometric average of pure components [113]. Additionally, a hypothetic average atom (AA) material serves as a suitable reference because it isolates the effects of compositional and chemical complexities in its HEA counterpart while reflecting HEA's average bulk properties [100]. Compositionally non-monotonical diffusion behaviors have been widely observed, and compositions exhibiting the most sluggishness are often non-equiatomic [16, 122, 123]. Therefore, it is crucial to develop an efficient simulation model for high-throughput studies of interstitial diffusion in HEAs across various compositions.

Molecular dynamics (MD) simulations, while powerful, are often constrained by their short timescale, making them less efficient at studying rare events, particularly at low temperatures. The kinetic Monte Carlo (KMC) method can extend the simulation timescale and is capable of studying these rare events. However, it struggles to accurately describe the complex local energy landscapes

typical in HEAs. Approximations such as random sampling method and species-average migration barrier method may oversimplify the local energy variations, potentially leading to incorrect conclusions about diffusion mechanisms. On-the-fly determination of migration barriers using method like nudged elastic band (NEB) [25] method or the kinetic activation relaxation technique (k-ART) [26] incurs significant computational overhead and is often impractical for high-throughput simulations.

In this study, we explore the self-interstitial diffusion in HEAs, specifically using FeNiCrCoCu as a model system, through MD and different KMC models, including the conventional KMC (C-KMC), random-sampling KMC (RS-KMC), and machine learning KMC (ML-KMC). Our results suggest that both C-KMC and RS-KMC methods tend to overestimate diffusivities and fail to reflect the actual diffusion patterns in HEAs. Conversely, ML-KMC, with its ability to incorporate local energy variations dynamically, closely reproduces the independent MD results and can be adaptable to various compositions for long-term simulations where MD is not feasible. Sluggish diffusion is noted when comparing the equiatomic HEA with several reference systems at different temperature scales from MD results. The study also investigates the geometric percolation effect and suggests that local variations in dumbbell formation energy can significantly influence atomic transport.

5.2 Methods

5.2.1 MD simulations

In this work, molecular dynamics (MD) simulations of interstitial-mediated diffusion in the FeNiCrCoCu model HEA were implemented through the LAMMPS package [51], and an interatomic potential of the embedded-atom method (EAM) type developed by Farkas et al. [105] was used. This potential ensures a stable face-center-cubic (fcc) phase across a board range of compositions, effectively minimizes the multiphase complexities seen in some HEA systems [106]. Also, the potential has a negligible heat of mixing (-0.0002 kJ/mol), reducing the impact of local ordering effects. All simulations used a cubic box of $10a_0 \times 10a_0 \times 10a_0$ in an fcc structure. The temperature range for the simulations spanned from 600 to 1000 K, increasing in 50 K increments. An initial interstitial dumbbell configuration was created at the center of the box by inserting a random atom to form a $\langle 100 \rangle$ dumbbell. The MD simulations were performed in an NPT ensemble, using Nose-Hoover-style thermostat and barostat [53, 110] to control the system temperature and pressure at zero bar, respectively. A time step of 2 fs was employed in all simulations, which lasted for 40 ns, with six independent simulations conducted for each condition. The position and type of current interstitial dumbbell were monitored by the Wigner-Seitz cell analysis every 2 ps during diffusion, as facilitated by the OVITO software [126]. The total diffusion coefficient was calculated based on the sum of atomic square displacement (ASD) [78],

$$D = \frac{ASD}{6t} \tag{5.1}$$

where *t* is the simulation time and the factor of 6 is for 3D diffusion. The final reported diffusivities were averaged from those six independent simulations at each condition.

5.2.2 Formation energy calculations

To determine the formation energy of various interstitial dumbbell types in a HEA, five different types of atoms (Fe, Ni, Cr, Co, Cu) were sequentially inserted into each lattice site to form a $\langle 100 \rangle$ dumbbell. After insertion, the system was allowed to relax, which is important because the interstitial dumbbell configuration post-relaxation may differ from the pre-relaxation one if it attains a more stable state. The type of the resulting dumbbell was identified using the OVITO software. The corresponding formation energy was computed based on the energy difference between the defective system and the defect-free system, written as,

$$E_f^i = E_{db}^i - E_0 - \mu_i \tag{5.2}$$

where E_{db}^i is the potential energy of the system with the interstitial dumbbell, E_0 is the potential energy of the defect-free systems, and μ_i denotes the chemical potential of the atom inserted at lattice site *i*. To compute μ_i, the Widom-type substitution method [56] was utilized. This approach quantifies the difference in chemical potentials between two different atomic species based on the energy difference observed before and after one atomic species is substituted for the other, written as,

$$\mu_i - \mu_j = E_{ij} - E_0 \tag{5.3}$$

$$\sum_i^{n=5} N_i \mu_i = E_{ij} \tag{5.4}$$

where E_{ij} is the current potential energy after using an atomic species *i* to replace an original *j* species, and N_i denotes the number of species *i* in the current configuration.

5.2.3 KMC simulations

⟨100⟩ dumbbell interstitial diffusion is simulated in all KMC models, including conventional KMC (C-KMC), random-sample KMC (RS-KMC), and machine learning KMC (ML-KMC). The migration energies of dumbbells are approximated by correlating them with the formation energy difference between successive dumbbell configurations [127, 128], expressed as,

$$E_{ijk}^{m} = max\left[max(0, \Delta E_f),\ E_{m,iso}^{j} + \frac{\Delta E_f}{2}\right] \tag{5.5}$$

where $E_{m,iso}^{j}$ is the reference migration barrier for species *j*, typically derived from pure component data. $\Delta E_f = E_f^{jk} - E_f^{ij}$ represent the formation energy difference between the final (*j*-*k*) and initial (*i*-*j*) dumbbell configurations. This approximation is applicable because the reaction path of a dumbbell in lattice KMC simulations have a fixed distance. In C-KMC, the E_f of a dumbbell uses the average formation energy of the corresponding dumbbell from static calculations. Therefore, if the dumbbell configuration does not change after a jump, the migration barrier simply uses the $E_{m,iso}^{j}$ from the corresponding pure component. In a RS-KMC simulation, the E_f of a dumbbell is randomly sampled from the formation energy distribution of the corresponding dumbbell from static calculations. In ML-KMC, the E_f is predicted dynamically based on the local atomic configuration.

A KMC simulation follows the steps:

1. Start with the same initial structure as in MD simulations, introducing a random ⟨100⟩ dumbbell interstitial at the center of the simulation box.

2. For each of two atoms forming the dumbbell, four possible jumps to nearest neighbor sites are considered, with total eight possible migration paths in one KMC step.

3. Migration barriers are estimated from the Eq. (5.5), and an empirical jumping attempt frequency (v_o) of 2.5 THz is consistently applied in all systems. The rate constant for each possible migration path is calculated by,

$$R_i = v_o \, exp\left(\frac{-E_i^m}{k_b T}\right) \tag{5.6}$$

4. A migration path *j* is selected from the *n* possible paths using a random number r_1 in the range of (0, 1], based on the cumulative sum condition,

$$\sum_{i=1}^{j} R_i > r_1 \cdot \sum_{i=1}^{n} R_i \tag{5.7}$$

5. Define another random number r_2 in the range of (0, 1] to evolve time according to,

$$\Delta t = \frac{-ln(r_2)}{\sum_{i=1}^{n} R_i} \tag{5.8}$$

6. After updating to a new state, repeat steps 2 to 5 for a total of 100,000 jumps to ensure the converge of the diffusion coefficient. Three independent KMC simulations are performed for each system and the reported diffusion coefficient is the averaged value of the three.

5.2.4 Machine learning model predicting dumbbell formation energies

An artificial neural network (ANN) model was developed to predict a dumbbell formation energy based on its local atomic configuration (LAC). Initially, the LAC was constructed by specifying the dumbbell type and configurations up to 4^{th} nearest neighboring shell surrounding the central vacancy site within the dumbbell, as depicted in Fig. 5.1, where the "white ball" denotes the vacancy site. Similar to previous work [123], for different dumbbell orientation, such as $\langle 010 \rangle$ and $\langle 001 \rangle$, the local Cartesian coordinates were rotated to align with a pre-defined $\langle 100 \rangle$ orientation to ensure the consistent ordering of the LAC sequency. In addition, a "one-hot" representation was applied to convert categorial numbers (i.e., atomic species 1 to 5) into one-hot vectors, for example, number 3 is represented as [0 0 1 0 0]. The ANN model employed a fully-connected architecture consisting of three hidden layers with 256, 128, and 64 neurons, respectively. The last hidden layer was followed by a normalization layer and a dropout layer with a dropout probability of 0.2 to remedy the overfitting problem. A ReLU activation function was utilized in all hidden layers, and the Adam optimizer was used for weight optimization [129]. The database was obtained from the dumbbell formation energy calculations in $(FeNiCo)_{1-x}(CrCu)_x$ HEAs, where x ranges from 0 to 100 at.% with an interval of 10 at.%. A total of 40,000 samples were collected. The chemical potentials of the five components of each alloy composition were calculated for dumbbell formation energy calculations, shown in Appendix 5.6, Fig. 5.A1. During the training phase, 80% the data were used for training and validation, while the remaining 20% were reserved for testing.

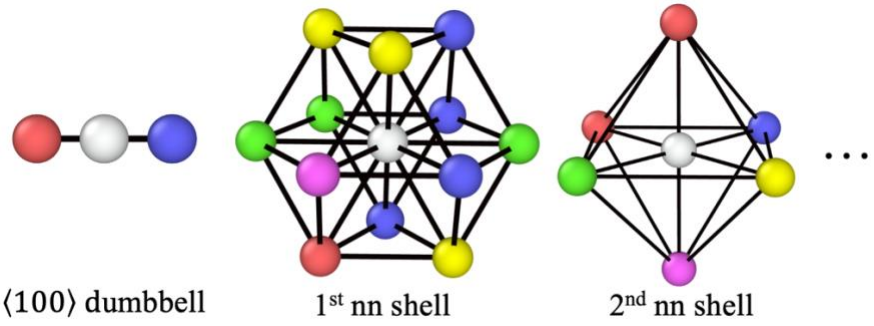

Fig. 5.1 Schematic illustration of the construction of local atomic configurations (LACs), where the "white ball" indicates a vacancy site.

5.3 Results

5.3.1 Sluggish diffusion in the HEA

To fully assess the sluggish diffusion, the interstitial diffusion coefficients (D) derived from MD simulations for an equiatomic HEA and several reference systems—including pure elements, their geometric average, AA material, and a sub-alloy (an equiatomic FeNiCo alloy)—are presented in Fig. 5.2. Specifically, Figure 5.2(a) plots these coefficients using absolute temperature scale, while Figure 5.2(b) uses the homologous temperature scale, both formatted as Arrhenius plots. The error bar on each diffusivity data point represents the standard deviation from six independent simulations. Table. 5.1 lists the melting temperature (T_m), activation energy (E^a), scaled activation energy (E^a/T_m), and pre-exponential factor (D_0) derived from Arrhenius treatments for all systems.

Figure 5.2(a) shows that the HEA exhibits pronounced sluggish diffusion compared to each of the five pure components, their geometric average, and AA materials at absolute temperature. However, the diffusivity in the FeNiCo alloy is lower than that observed in the HEA. Figure 5.2(b) further highlights that when assessed on a homologous temperature scale, the sluggish diffusion in HEA becomes even more apparent, with lower diffusivities than those in all reference systems, including the FeNiCo alloy. These findings suggest that interstitial diffusion in the HEA can be characterized as "sluggish" since it is slower than nearly all reference systems, regardless of the temperature scale used. However, these results also indicate that the conclusion of "sluggish diffusion" is contingent upon on the choice of a reference system (e.g., FeNiCo can be slower than the HEA at an absolute temperature scale), underscoring the importance of establishing a standard for identifying sluggish diffusion. Thus, rather than merely confirming the existence of sluggish diffusion, it is crucial to delve deeper into the controlling parameters that govern the diffusion mechanism.

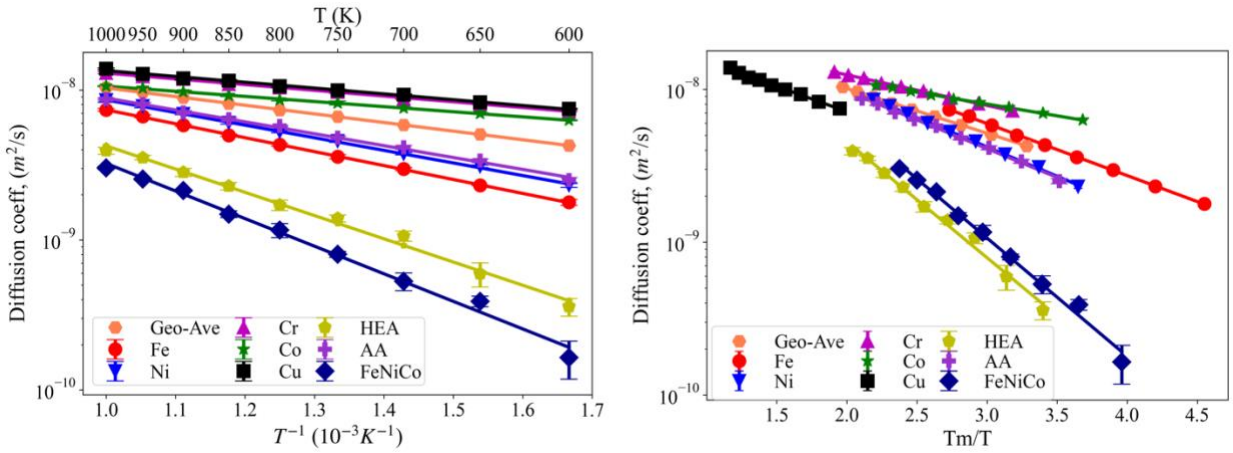

Fig. 5.2. Arrhenius plots of the diffusivities in the HEA, five pure components, geometry average, the FeNiCo alloy, and AA material for temperatures from 600 to 1000 K at (a) the absolute temperature scale, and (b) the homologous temperature scale.

Table 5.1. Melting temperature (T_m), activation energy (E^a), scaled activation energy (E^a/T_m), and pre-exponential factor (D_0).

	HEA	**FeNiCo**	**AA**	**Geo-Ave**	**Fe**	**Ni**	**Cr**	**Co**	**Cu**
$\boldsymbol{T_m}$ (K)	2040	2370	2110	1970	2730	2190	1910	2210	1170
$\boldsymbol{E^a}$ **(eV)**	0.31	0.37	0.16	0.11	0.18	0.17	0.08	0.07	0.08
$\boldsymbol{D_0}$ **(m^2/s)**	1.50e-7	2.2e-7	5.47e-8	3.88e-8	6.25e-8	5.94e-8	3.11e-8	2.32e-8	3.28e-8
$\boldsymbol{E^a/T_m}$	1.52e-4	1.56e-4	7.58e-5	-	6.59e-5	7.76e-5	4.18e-5	3.16e-5	6.84e-5

5.3.2 Dumbbell configurations

Figure 5.3(a) and (b) present the fraction of different dumbbell types observed during the diffusion process in the equiatomic HEA across different temperatures. These interstitial dumbbells are categorized both by geometric configuration—⟨100⟩, ⟨110⟩, and ⟨111⟩ dumbbell families—and species configuration (e.g., Fe-X dumbbells, where X represents one of the five species in the HEA). In the simulations, snapshots capturing the spatial position and species of each dumbbell were taken every 2 ps, accumulating data on 2,000 dumbbells per simulation run. Figure 5.3(a) reveals that the ⟨100⟩ dumbbell family remains the most dominant (over 90%) throughout the temperature range, although the ⟨110⟩ and ⟨111⟩ families exhibit slight increase

with rising temperature. This trend aligns with the known stability of the ⟨100⟩ dumbbell in fcc metals such as Ni [130]. Meanwhile, Figure 5.3(b) highlights that the predominant dumbbell species at various temperatures consistently involve Cu and Cr atoms, with the Cu-X dumbbell being the most prevalent. This observation points to the nuanced chemical-biased diffusion between individual species within the HEA, suggesting that the specific characteristics of each atomic type significantly influence the overall diffusion behavior.

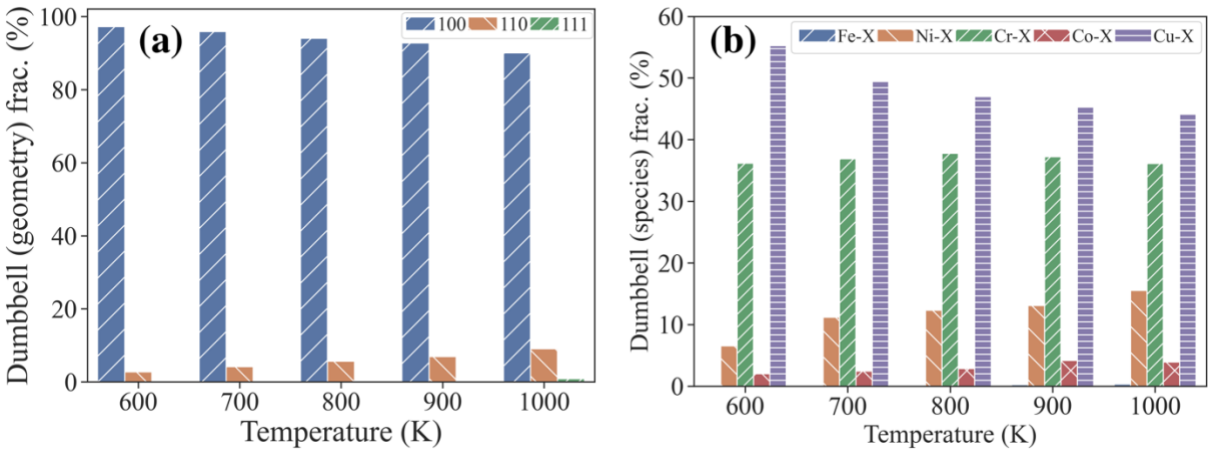

Fig. 5.3 The fraction of different dumbbells during diffusion, in term of (a) geometric configurations and (b) species configuration.

5.3.3 ⟨100⟩ dumbbell formation energy

It has been demonstrated that the local formation energy of migrating defects significantly influences the diffusion process [131]. In this context, since the ⟨100⟩ dumbbell is particularly dominant during diffusion, as illustrated in Fig. 5.4, the subsequent calculation is primarily focused

on this dumbbell configuration. Figure 5.4 presents the formation energy distributions for all fifteen possible ⟨100⟩ dumbbell configurations, each fitted to a Gaussian distribution, with the mean and standard deviation detailed in Table 5.2. Nota that, each subplot in Fig. 5.4 includes two numbers in the upper right corner: the upper number indicates the actual count of dumbbells post-relaxation, while the lower number reflects the count of pre-relaxation. The analysis reveals that the formation of dumbbells occurs in a descending order, starting with Cu-, followed by Cr-, Ni-, Co-, and Fe-X dumbbells. This sequence is inversely proportional to the mean formation energies. This pattern underscores a clear and direct correlation between the lower formation energies and the higher prevalence of specific dumbbell configurations during diffusion. Although it reveals a straightforward correlation, average formation energy alone is incomplete to fully describe sluggish diffusion phenomena. For instance, the AA material and the HEA have similar average formation energies—4.89 eV for AA and 4.81 eV for HEA—yet the HEA exhibits significantly slower diffusivities than the AA material, as discussed in Fig. 5.2. This discrepancy highlights that, beyond average formation energy alone, the variations in the formation energy landscape also play a non-neglectable role in influencing interstitial diffusion.

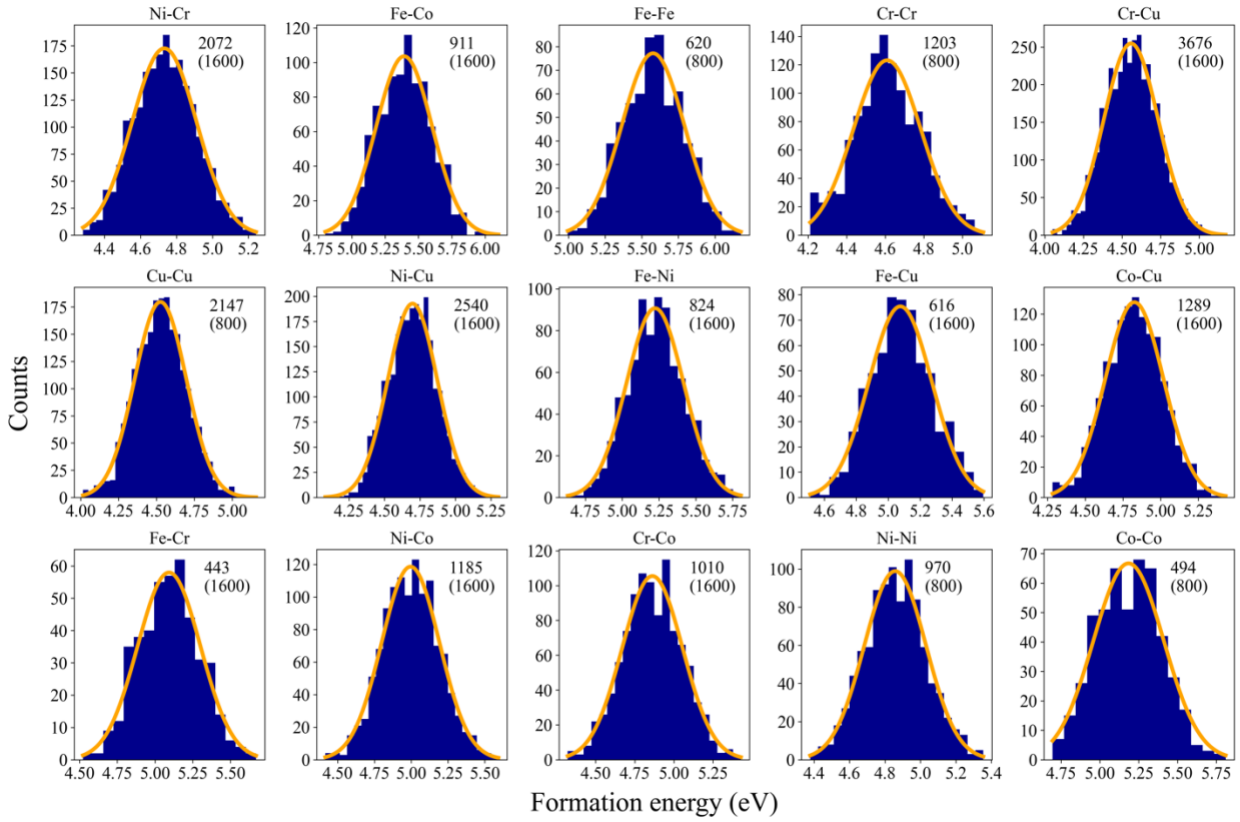

Fig. 5.4. ⟨100⟩ dumbbell formation energy distributions. In each sub plot, the upper number indicates the actual count of dumbbells post-relaxation, while the lower number reflects the count pre-relaxation.

Table 5.2. The mean and standard deviation of ⟨100⟩ dumbbell formation energy for all fifteen configurations in HEA.

	Fe	**Ni**	**Cr**	**Co**	**Cu**	**mean**
Fe	5.58 ± 0.20	5.23 ± 0.19	5.09 ± 0.20	5.39 ± 0.20	5.08 ± 0.19	5.29 ± 0.26
Ni		4.86 ± 0.17	4.74 ± 0.17	5.00 ± 0.19	4.70 ± 0.17	4.83 ± 0.24

Cr	4.61 ± 0.17	4.86 ± 0.19	4.55 ± 0.17	4.67 ± 0.23
Co		5.19 ±0.20	4.82 ± 0.19	5.02 ± 0.28
Cu			4.53 ± 0.17	4.65 ± 0.23
HEA				4.81 ± 0.33

5.3.3 Machine learning and KMC simulations

Figure 5.5 presents a high prediction accuracy of the ANN model on the testing set, achieving an average mean absolute error (MAE) of 0.033 eV and a correlation coefficient (R^2) of 0.98. These results imply that the ANN model can accurately predict the dumbbell formation energies across various compositions. Figure 5.6 illustrates the diffusion coefficients calculated from C-KMC, RS-KMC, and ML-KMC methods for an equiatomic HEA. These results are compared alongside the independent MD results. It is noted that the both C-KMC and RS-KMC methods underestimates the activation energy and overestimate the diffusivities when compared to the MD results, but the ML-KMC method can closely replicates the activation energy and diffusivities obtained from the MD simulations. This confirms the efficacy of ML-KMC in capturing the true diffusion behavior in an HEA.

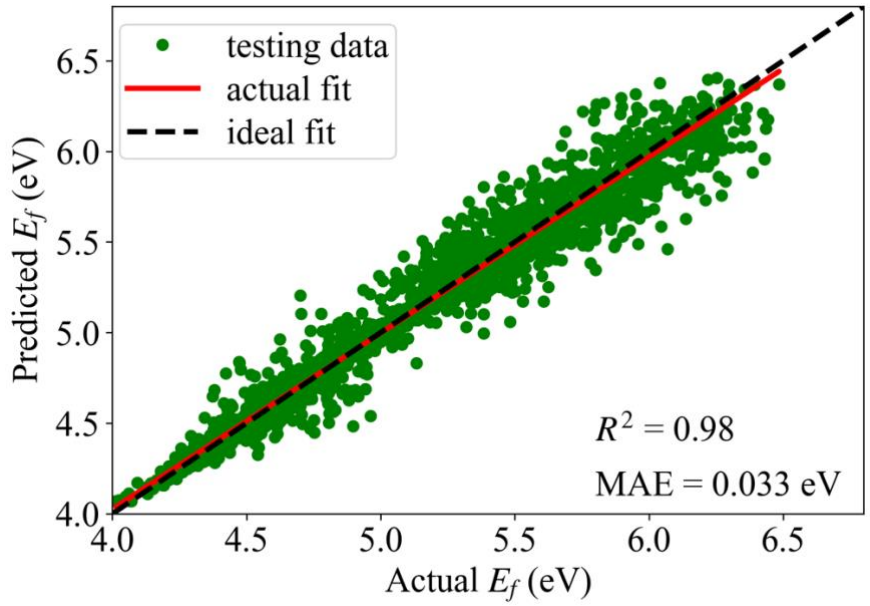

Fig. 5.5 Prediction performance of the ANN model on the testing set.

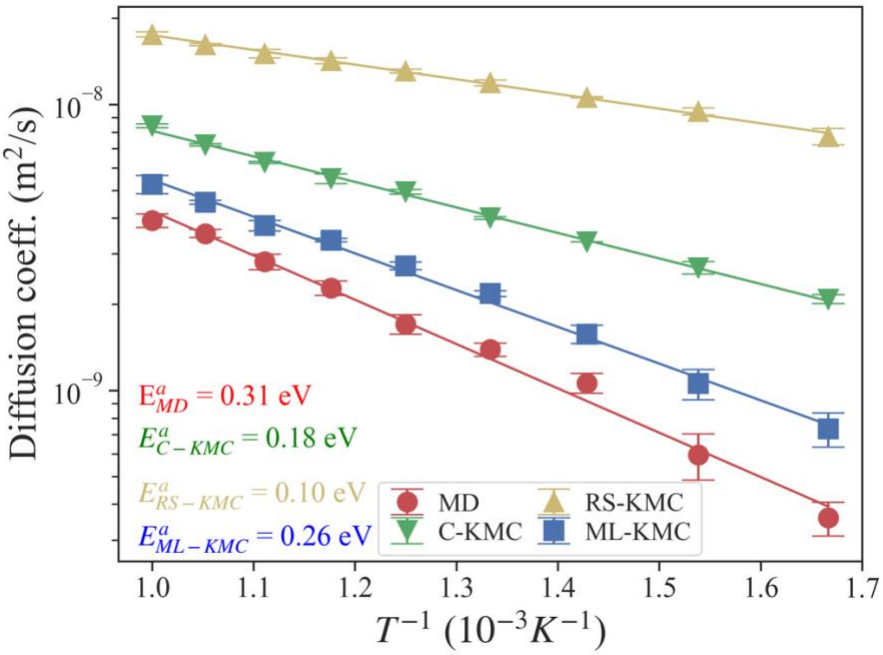

Fig. 5.6 ⟨100⟩ dumbbell interstitial diffusivities calculated from C-KMC, RS-KMC, and ML-KMC, alongside with the independent MD data.

Figures 5.7(a)-(d) display the fractions of dumbbell species configurations from MD, C-KMC, RS-KMC, and ML-KMC simulations, respectively. The result shows that C-KMC tends to overestimate the frequency of Cr-X dumbbell configurations while underestimate Cu-X dumbbells. RS-KMC inaccurately raises concurrence of rarer events such as Fe- and Co-X dumbbells. These highlights the limitations of C-KMC and RS-KMC in capturing the full spectrum of dynamic events, leading to mispredictions of different dumbbell characteristics. In contrast, by comparing Fig. 5.7(d) and (a), ML-KMC demonstrates a more accurate reproduction of both frequent and rare dumbbell migration events, aligning more closely with the MD results. This improved accuracy in ML-KMC simulations is attributed to its ability to predict local variations in dumbbell formation energies, which better reflects the complex interactions within HEA systems. Further insights into the diffusion disparity between those KMC simulations are provided in Fig. 5.8, which plots the formation energy difference (ΔE_f) between successive dumbbell transition at 600 K. In C-KMC simulations, as shown in Fig. 5.8(a), ΔE_f exhibits a mean value of -0.0 eV and a standard deviation of 0.07 eV, suggesting a diffusion pattern akin to a "random barrier" model. This model is characterized by uniform potential wells and varying saddle energies, which may artificially enhance diffusion rates by not adequately penalizing energetically unfavorable transitions [22]. Figure 5.8(b) reveals that RS-KMC has a ΔE_f distribution with a mean value of -0.0 eV and a large standard deviation of 0.28 eV, likely due to its inaccurate sampling rare dumbbell transitions, such as Fe- or Co-X configurations, thereby artificially increasing energy variation. The Figure 5.8(c) shows that ML-KMC exhibits a ΔE_f with a mean value of -0.0 eV and a moderate standard

deviation of 0.12 eV, indicating that both under- and over-estimations of energy variation by KMC methods can lead to incorrect diffusion simulations.

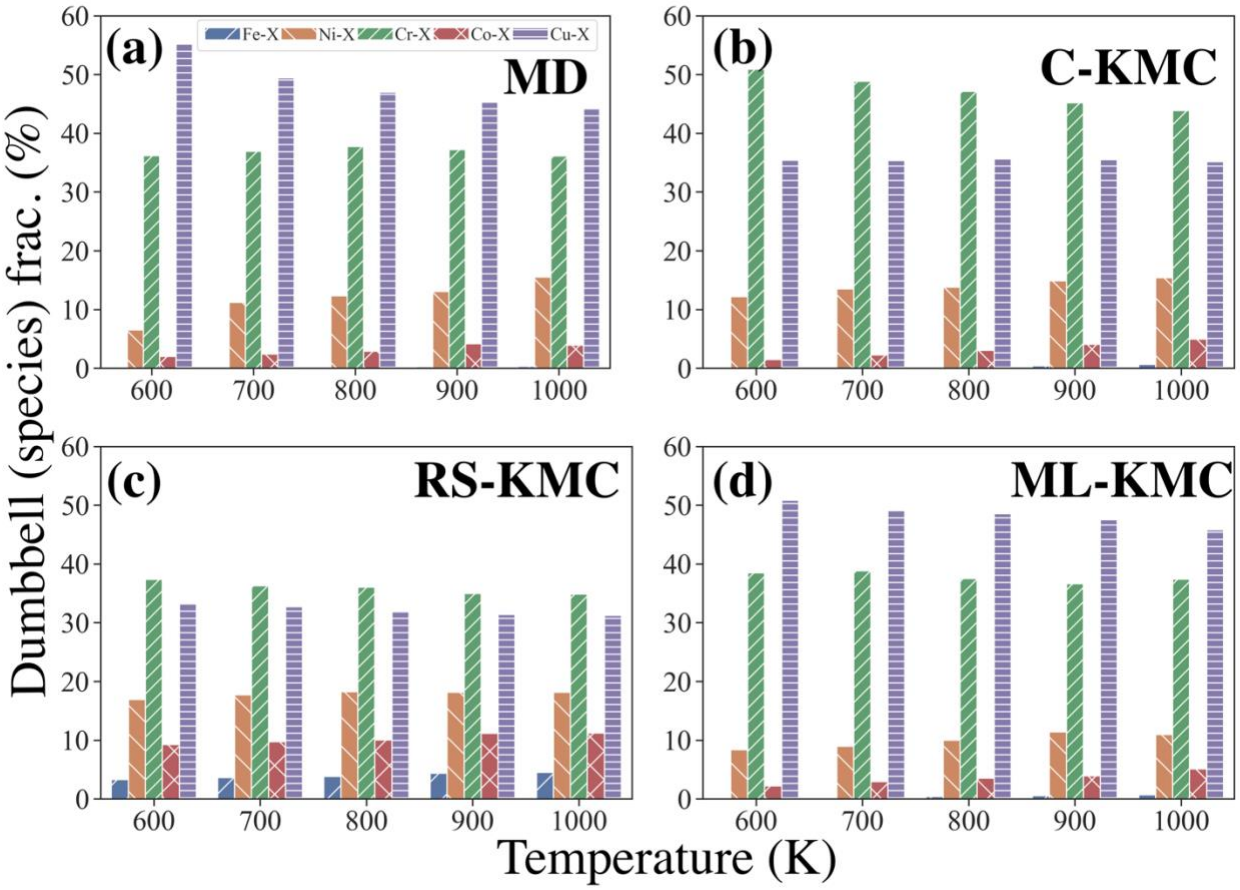

Fig. 5.7 The fraction of dumbbell species configurations in (a) MD, (b) C-KMC, (c) RS-KMC, and (b) ML-KMC.

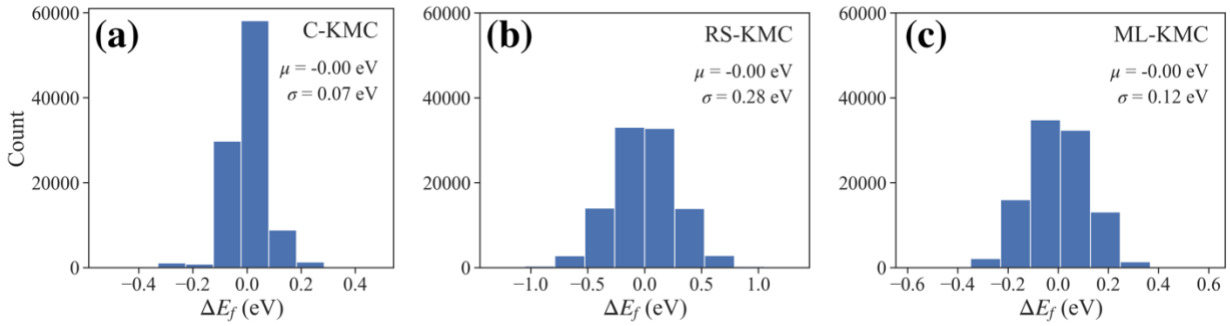

Fig. 5.8 Formation energy difference (ΔE_f) between successive dumbbell migrations at 600 K in (a) C-KMC, (b) RS-KMC, and (c) ML-KMC.

Figure 5.9 shows correlation factors (f_c) derived from C-KMC, RS-KMC, and ML-KMC for the HEA across different temperatures, along with data from simulations using AA material. The f_c was calculated using the formula,

$$f_c = \frac{ASD}{Nr^2} \tag{5.9}$$

where N is the number of KMC steps and $r = a_0/\sqrt{2}$ is the jump length. The f_c serves as an indicator of the degree of anti-correlation in jumps within KMC simulations; a lower f_c signifies stronger anti-correlated jumps. The AA materials exhibits an f_c of ~0.43 across all temperatures, which is consistent with the random walk behavior typical of a pure element [132]. Due to the inherent characteristics of the random-sample method, the RS-KMC exhibits f_c closest to the random walk behavior. The ML-KMC consistently shows the lowest f_c values compared to both C-KMC and RS-KMC across the temperature spectrum, confirming its enhanced correlation

between successive dumbbell transitions and a higher likelihood of local trapping and retarded diffusion.

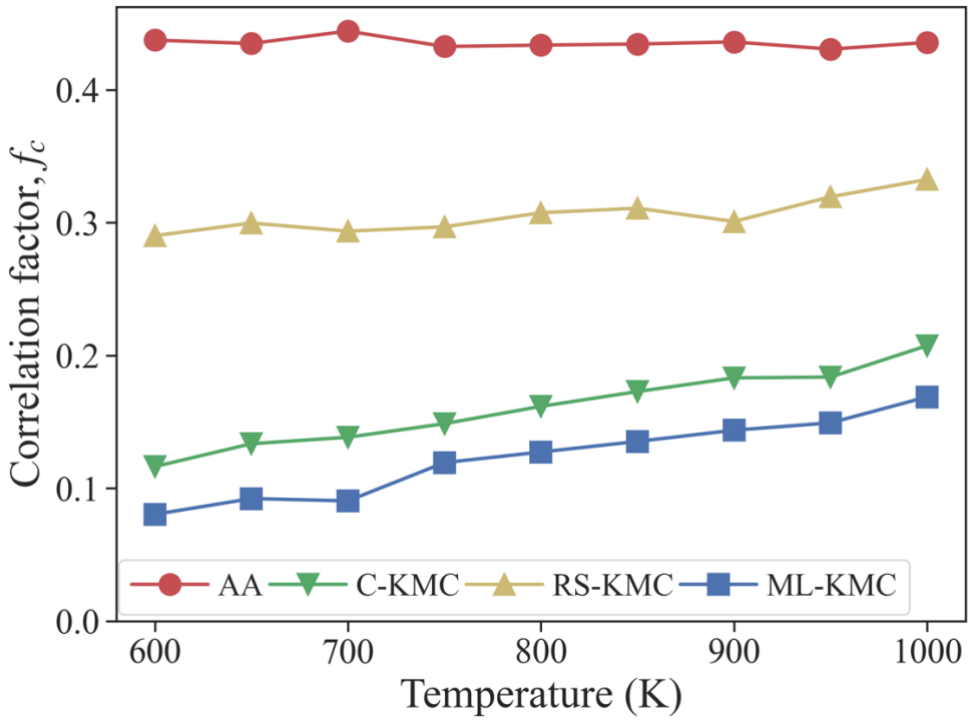

Fig. 5.9 Correlation factor (f_c) from C-KMC, RS-KMC, and ML-KMC for HEA, along with the data from AA material.

5.3.4 Percolation effects

Geometric percolation effects, recognized for influencing diffusion characteristics in binary CSAs, are of significant interest in the study of diffusion dynamics, particularly regarding how they contribute to sluggish diffusion. Previous studies [16, 131] have shown that in binary Ni-Fe alloys, diffusion behaviors exhibit specific patterns based on the concentration of alloy

components. For vacancy diffusion, the slowest diffusion rates typically occur when the concentration of the faster-diffusing species is around 20 at. %, while for self-interstitial diffusion, the slowest rates are observed when the faster diffuser approaches ~70 at. %. These two concentrations correspond to percolation thresholds of vacancy and ⟨100⟩ dumbbell diffusion, respectively. To explore the possibility of similar percolation effects in HEAs, a series of non-equiatomic $(FeNiCo)_{1-x}(CrCu)_x$ alloys were prepared, where x ranges from 0 to 100 at.%. In this context, the (FeNiCo) and (CrCu) components are treated as distinct units, with each component within these units being equiatomic. Given that pure Cr and Cu exhibit similar and notably fast diffusivities (as illustrated in Fig. 5.2), and considering that the Cr- and Cu-X dumbbell configurations dominate the diffusion process, (CrCu) is designated as the "faster diffuser" and (FeNiCo) as the "slower diffuser," effectively mimicking a binary alloy system.

Figure 5.10 presents a complete comparison of the results from ML-KMC and MD simulations using Arrhenius treatments across temperatures ranging from 600 K to 1000 K for $(FeNiCo)_{1-x}(CrCu)_x$ alloys. The activation energy (E^a), extracted from for both ML-KMC and MD results, is detailed in each sub-figure. Overall, the results of ML-KMC agree well with the independent MD results. Some discrepancies are observed when the (CrCu) concentration exceeds 50 at. %, where the ML-KMC tends to overestimate the diffusivities. However, given the use of a constant jump frequency (v_o) and the approximation of migration barriers in KMC simulations, these discrepancies are considered reasonable and acceptable. Figure 5.11(a) displays the diffusion coefficients of $(FeNiCo)_{1-x}(CrCu)_x$ alloys at 800 K from both ML-KMC and MD results, illustrating a consistent trend over the (CrCu) concentrations. Specifically, both ML-KMC and MD exhibit that the lowest diffusivity is achieved at a (CrCu) concentration of 10 at. %; however,

no percolation effect is detected (which would be expected as a (CrCu) concentration of 70 at. %). This observation is consistent with our recent findings on vacancy-mediated diffusion in the same HEA systems, where no percolation effect was observed neither [123], underscoring the need for a more general model for studying various HEA compositions. ML-KMC method emerges as a promising candidate for such modeling, as demonstrated by its efficient simulations across diverse compositions and temperatures. Figure 5.11(b) further illustrates the E^a from both ML-KMC and MD results for $(FeNiCo)_{1-x}(CrCu)_x$ alloys, where the ML-KMC closely reproduces the E^a trend observed in independent MD results for most of compositions. This confirms the capability of ML-KMC in applying to non-equiatomic HEA compositions.

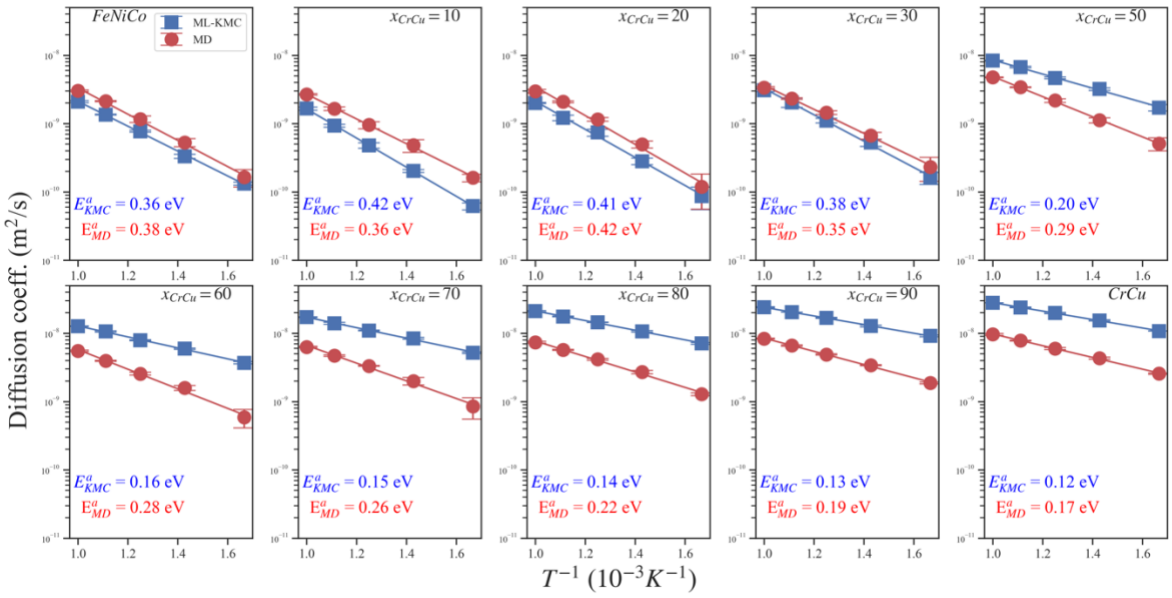

Fig. 5.10 Arrhenius plots of diffusion coefficients for the (FeNiCo)1-x(CrCu)x alloys obtained from ML-KMC and MD simulations in temperature range from 600 K to 1000 K.

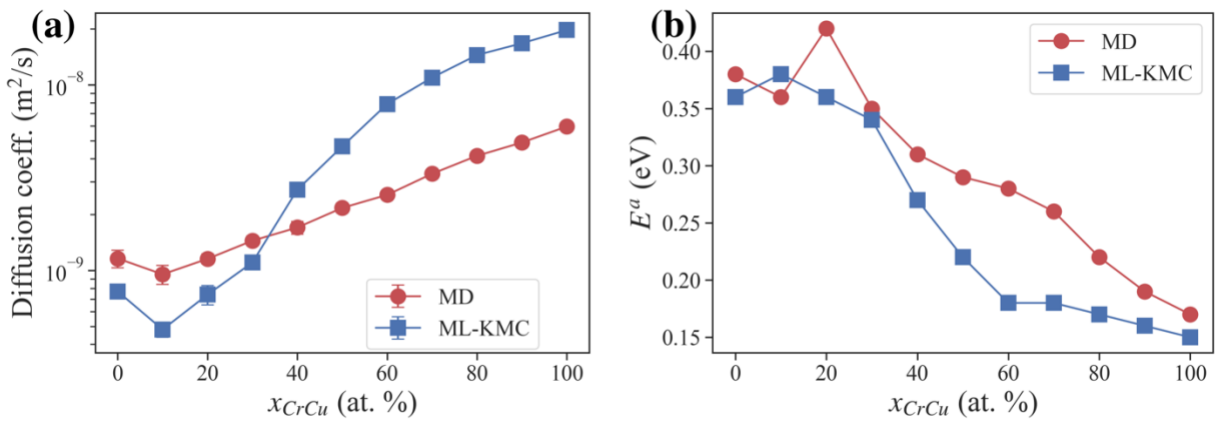

Fig. 5.11 (a) Diffusion coefficients of $(FeNiCo)_{1-x}(CrCu)_x$ alloys at 800 K. (b) Activation energies extracted derived from ML-KMC and MD simulations.

Although a constant v_o is employed in the current work, it should ideally be compositional-dependent to reflect more accurate dynamic behavior of different compositions. Figure 5.12(a) displays the diffusivities of five components of a HEA from MD and KMC simulations, all using a fixed v_o of 2.5 THz in KMC. The noticeable discrepancies between KMC and MD results for those pure components underscore that v_o indeed varies with composition. Further exploration is presented in Figure 5.12(b), which illustrates the fitted v_o values of pure components in KMC simulations, adjusted to benchmark the MD results at different temperatures. It shows that the temperature has limited effects on v_o but elements like Ni, Co, and Fe tend to exhibit larger v_o values compared to Cr and Cu. Moreover, when fitting the ML-KMC results to benchmark the MD results, the v_o value shows a nearly monotonic compositional dependency, as shown in Fig. 5.12(c), where an (FeNiCo)1-x(CrCu)x alloy with lower (CrCu) concentration has higher v_o values and an equiatomic CrCu alloy has the lowest one. This trend is qualitatively consistent with

the behaviors observed for the pure elements, indicating that using ML-KMC results can also accurately captured some insights of the atomic vibrations within the system. Therefore, incorporating a compositionally dependent v_o in ML-KMC is expected to yield results that closely align with those from MD. Nevertheless, the influence of v_o on diffusion coefficient is linear, while the E^a can exponentially affect the diffusivity. Thus, accurately predicting the E^a is more critical. As demonstrated in Fig. 5.11(b), the ML-KMC can reasonably reproduce the E^a for most of non-equiatomic compositions.

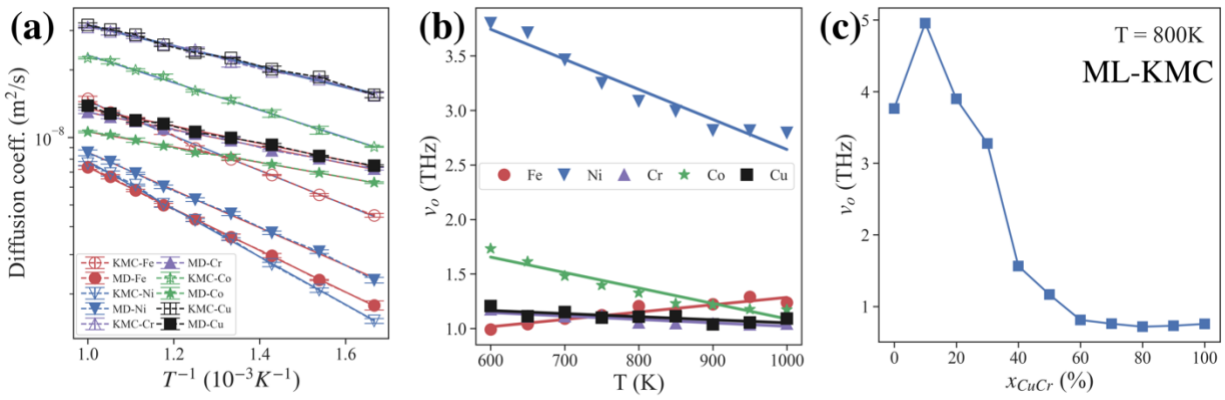

Fig. 5.12 (a) Diffusivities of five pure components from MD and KMC simulations. (b) the fitted $v_o$values for each pure component. (c) the fitted $v_o$values in ML-KMC for $(FeNiCo)_{1-x}(CrCu)_x$ alloys.

5.4. Discussions

In real HEA systems, the interactions between atomic species are notably complex, typically resulting in a rugged potential energy landscape. The mean-field or random-sample

approach used in C-KMC or RS-KMC simulations failed to capture the actual local energy variances, which can lead to incorrect estimation on diffusion coefficients. Dumbbell interstitial diffusion is characterized by specific chemical configurations and influenced by local atomic configurations. Consequently, the same type of dumbbell can have different formation energies dependent on its immediate neighboring atoms. Therefore, with the ability of predicting dumbbells formation energy dynamically based on the local atomic environment, the ML-KMC method offers a more accurate approximation of the actual diffusion behavior in HEAs.

In prolonged diffusion scenarios, the potential for the development of short-range orders (SROs) could significantly influence the interstitial diffusion behavior. However, in this study, the employed EAM potential, characterized by its low heat of mixing, minimizes the tendency for chemical ordering even after extended periods of KMC simulations. To quantify SRO, the Warren-Cowley parameter for the 1st nearest neighboring shell is calculated,

$$\alpha^{ij} = 1 - \frac{\langle N^{ij} \rangle}{c_j N} \tag{5.10}$$

where i and j represent atom species, $\langle N^{ij} \rangle$ is the average number of j-type atoms surrounding i-type atoms, N is the total number of atoms in the 1st nearest neighboring shell, and c_j is the concentration of j-type atom species in the system. The evolution of SROs throughout the simulations is shown in Fig. 5.13. It shows that all pairs are close to zero, confirming the sustained randomness of the HEA system during diffusion. This characteristic is crucial as it ensures that the material retains a degree of configurational typical of HEA, thereby avoiding the pronounced effects of chemical ordering that could otherwise influence material properties unpredictably.

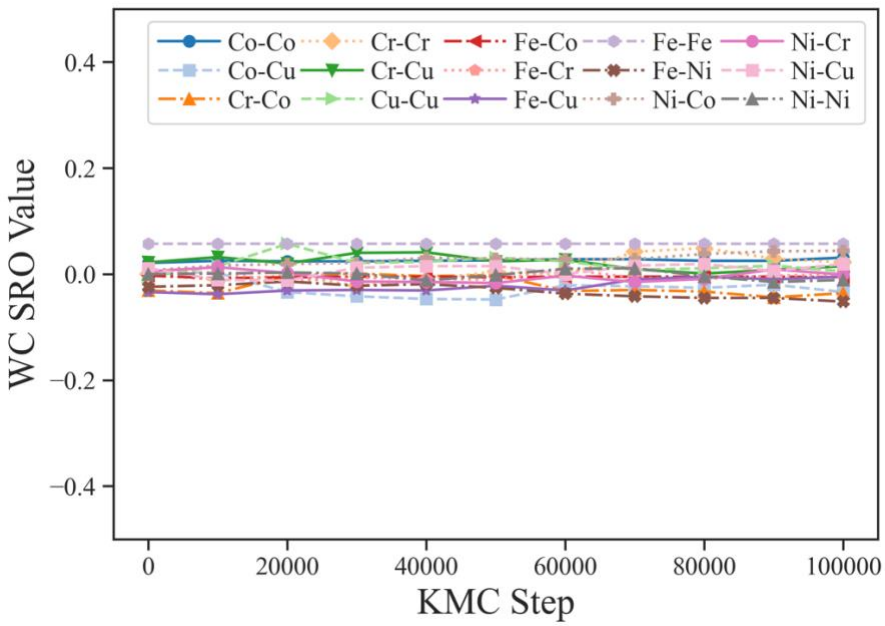

Fig. 5.13 SRO evolution for ML-KMC simulation for an equiatomic HEA at 600 K.

As discussed in this work, interstitial diffusion in the equiatomic HEA can be identified as "sluggish" compared to various reference systems. However, a previous study on the same HEA system reported no sluggishness in vacancy-mediated diffusion [21]. This difference highlights the impact of defect formation energy on diffusion processes. Unlike a vacancy in a HEA, which lacks its chemical identity, an dumbbell interstitial shows a significant variation in formation energy depending on the specific configuration. Figure 5.14 (a) shows the average vacancy formation energy is similar regardless of the species removed, while Figure 5.14 (b) exhibits a broad formation energy distribution across different dumbbells. The standard deviation of vacancy formation energy is 0.21 eV, while its activation energy is significantly higher than 1.22 eV described in Figure 4.9. In contrast, interstitial dumbbell formation energies from this study have

a standard deviation of 0.33 eV, which is comparable to its activation energy of 0.31 eV. Therefore, vacancy diffusion appears to similar to a random-barrier model, where larger barriers do not necessarily hinder diffusion if lower alternative barriers are available, thereby potentially enhancing diffusion. In contrast, interstitial diffusion experiences a broad distribution of formation energies that likely creates local traps, causing dumbbells to spend more time at specific sites and slowing diffusion. This observation aligns with the findings from a prior study by Thomas et al., which concluded that a broader distribution of formation energies, more than migration barriers, can impede diffusion [22].

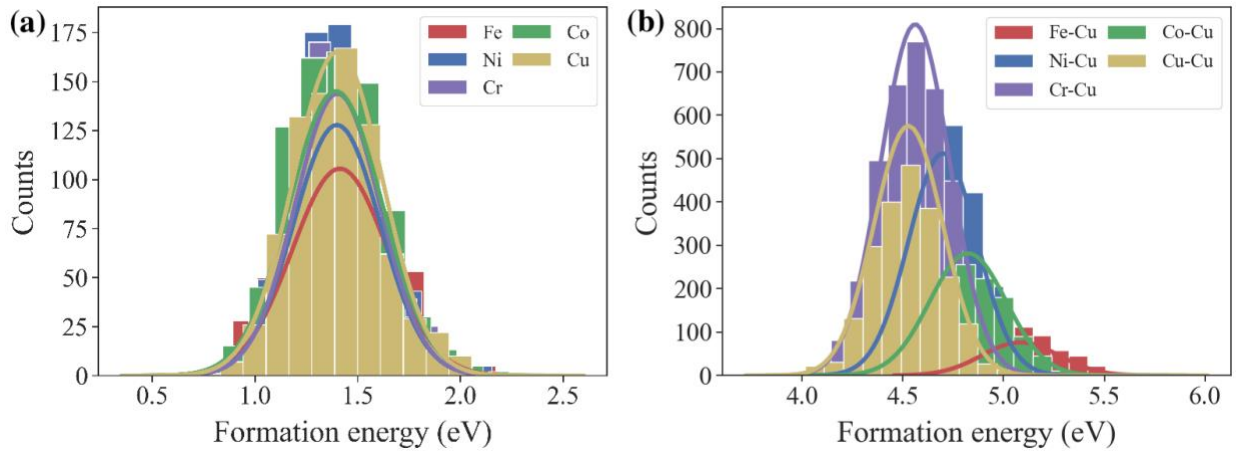

Fig. 5.14 (a) Vacancy formation energy distributions in the FeNiCrCoCu HEA. (b) Cu-type dumbbell formation energy distributions in the FeNiCrCoCu HEA.

5.5. Conclusions

MD part: sluggish interstitial diffusion is observed in the equiatomic HEA and no percolation threshold is observed for faster diffuser (CrCu)

In this study, sluggish interstitial diffusion in an equiatomic FeNiCrCoCu HEA has been assessed by comparing it with a range of reference systems. These systems include its five pure components, their geometric average, average atom (AA) materials, and its sub-alloy system FeNiCo, evaluated under both absolute and homologous temperature scales. The MD simulations reveal significant sluggish interstitial diffusion within the HEA, as it exhibits lower diffusion coefficients than nearly all the reference systems under both temperature scales, except for the sub-alloy system FeNiCo at absolute temperatures. To investigate the possible percolation effects, the two fastest diffusing species, Cr and Cu, were collectively treated as one entity (CrCu), while the remaining species (FeCrCo) were treated as another, effectively mimicking a binary alloy system. The concentration of (CrCu) was systematically varied from 0 to 100 at.%. Contrary to expectations based on the binary alloy systems, where a percolation threshold at approximately 70 at. % of faster diffuser correlates with minimal diffusivity; no such threshold or sluggish diffusion was observed in the $(FeCrCo)_{1-x}(CrCu)_x$ HEA system. Remarkably, the total diffusivity in the HEA system reached its lowest at a (CrCu) concentration of 10 at. %. These results confirm that a non-equiatomic composition, e.g., $Fe_{30}Cr_{30}Co_{30}Cr_5Cu_5$, can achieve more pronounced sluggish diffusion than the equiatomic composition as well as its sub-alloy system. This underscores the need of developing a high-throughput modeling techniques in HEA systems to gain a comprehensive understanding of the diffusion properties.

KMC part: A machine learning-KMC method can reasonably replicate the MD results across various temperatures and composition. This method can serve as an effective compromise for high-throughput modeling in HEA systems.

The conventional and random-sample KMC (C-KMC and RS-KMC) methods, which employ a simple mean-field model and random sampling method, respectively to approximate dumbbell transition energies, fails to accurately capture the diffusion dynamics in HEAs. To address these limitations, the machine learning KMC (ML-KMC) method has been developed. This approach dynamically predicts dumbbell formation energies based on local atomic configurations, allowing it to closely replicate the diffusion behaviors of various HEA compositions. This is evidenced by the close alignment of activation energies E^a derived from both ML-KMC and independent MD results, as well as the similar diffusivities across most compositions studied. The primary discrepancy in diffusivity between ML-KMC and MD primarily stems from the use of a constant jumping attempt frequency v_o and the approximation of the migration barriers. Nevertheless, ML-KMC accurately predicts the occurrence of different dumbbell configurations during diffusion and identifies the composition with the lowest diffusivities in (FeCrCo)1-x(CrCu)x HEAs, confirming the absence of percolation threshold in HEAs.

The findings from this study can offer valuable insights into the diffusion properties of HEAs when the formation energy plays a pivotal role in governing interstitial dumbbell diffusion. Firstly, the average formation energy significantly influences preferential dumbbell diffusion; for instance, dumbbells involving Cr or Cu, which both have lower average formation energies than other dumbbells, are more likely to form during diffusion. Secondly, the formation energy

variation is critical in governing the diffusion process, and overestimating or underestimating it can lead to incorrect conclusions. Therefore, a comprehensive spectrum of formation energies is necessary for a more detailed description of diffusion. The success of the ML-KMC simulation lies in its ability to predict formation energy on-the-fly during simulations, enhancing its predictive accuracy and reliability. Additionally, the current ML-KMC offers the advantage of avoiding costly on-the-fly calculations of migration barriers by approximating them using more easily computed formation energies, making it an effective high-throughput modeling framework. This approach is expected to be applicable to other HEA systems and assist in the down-selection of sluggish HEA compositions for optimized HEA design.

5.6 Appendix

1. Chemical potentials (μ) for $(FeNiCo)_{1-x}(CrCu)_x$ alloys were determined using the Widom-type substitution method [56]. This involved performing substitutions between two different species at each lattice site, each with four times of substitutions, resulting in a total of 16,000 linear equations based on Eq. (5.3) and (5.4). The chemical potentials of these species were derived using the least squares method, shown in Fig. 5.A1.

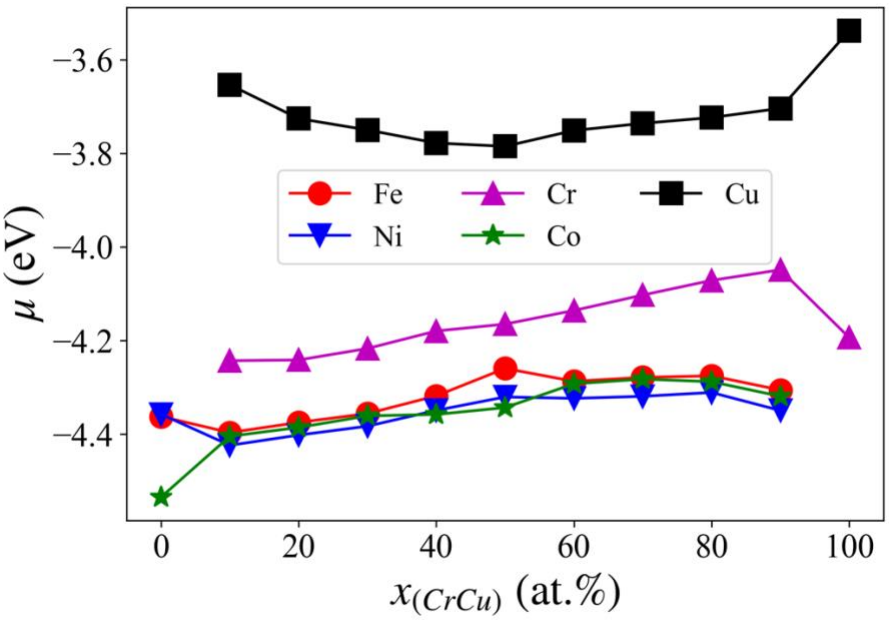

Fig. 5.A1. Compositional-dependent chemical potentials of all five components in $(FeNiCo)_{1-x}(CrCu)_x$ alloys.

CHAPTER 6 Outlook

This chapter serves as a forward-looking discourse on the trajectory of ongoing research endeavors that extend beyond the scope of the completed work. It outlines the significance and the anticipated impact of two meaningful yet unfinished projects that promise to further the field of diffusion research using advanced computational methodologies. The first project aims to extend the machine learning-kinetic Monte Carlo (ML-KMC) framework to predict interstitial migration barriers on-the-fly and thus generate more accurate diffusion simulations. Although the ML model for predicting interstitial migration barriers has been established, its integration into the KMC framework remains an open chapter with vast potential for exploration. The second project aspires to develop a comprehensive ML potential for high-entropy alloys (HEAs), with the aim at refining the predictive capabilities of the ML-KMC model. Progress has been charted for equiatomic systems; however, generating a complete ML potential for HEAs is a formidable challenge due to the immense data and computational demands involved. The forthcoming sections will delve into the introductory aspects and initial findings related to these two projects.

6.1 Interstitial migration barrier prediction

6.1.1 Introduction

Chapters 3 and 4 showcased the successful application of combining ML with KMC techniques to elucidate vacancy-mediated diffusion mechanisms in binary and quinary concentrated alloys. The ML model, trained on a comprehensive database of vacancy migration barriers across various local atomic configurations (LACs), acts as an accurate, on-the-fly

calculator for KMC simulations. The ML-KMC methodology has proven pivotal in revealing the intricacies of sluggish and chemically biased diffusion mechanisms, providing a promising high-throughput approach for traversing the extensive compositional spectrum of concentrated alloys, pinpointing compositions endowed with significant sluggish diffusion. Chapter 5 has emphasized the critical need to understand the diffusion mechanisms of self-interstitials and developed a ML model to predict the interstitial dumbbell formation energies. This method effectively simulated various HEA compositions across different timescales and temperature ranges, circumventing the substantial computational overhead typically associated with calculating migration barriers on-the-fly. As such, it represents an efficient high-throughput modeling approach for studying HEAs. However, since the interstitial migration barriers were approximated by correlating changes in dumbbell formation energies, this method introduces some errors during diffusion simulations. In this context, a ML model that can directly predict the dumbbell migration barriers can offer a promising solution to overcome this problem. Once proven adaptability for both vacancy and interstitial defects, this methodology could be extended to more complex defect structures.

However, unlike vacancy-mediated diffusion, self-interstitials in alloys typically form as dumbbells, with the specific type of interstitial dumbbell playing a crucial role in the diffusion process. This complexity makes training a ML model for predicting interstitial migration barriers a more challenging task. Additionally, the challenge extends to extensive nudged elastic band (NEB) calculations required for constructing the training dataset for a ML model. Interstitial configurations in face-centered cubic (fcc) structures, for instance, can possibly be octahedral, tetrahedral, and crowdion, as well as [100], [110], and [111] dumbbells [130]. Including all possible interstitial configurations in the training data significantly complicates NEB calculations

and increases computational demands. Moreover, maintaining the stability of interstitial configurations during NEB calculations is necessary, as configurations may change due to initial unstable states, a phenomenon highlighted by the interstitial dumbbell formation energy analysis in Chapter 5. In this work, the ANN model has been trained to predict interstitial migration barriers in FeNiCrCoCu model systems only for the [100] dumbbell configuration, which has been identified as the most stable and prevalent dumbbell form in Chapter 5. To ensure the accuracy of NEB calculations, both the initial and final dumbbell interstitial configurations are precisely defined and maintained throughout.

6.1.2 Preliminary methods and results

NEB calculations implemented in LAMMPS are utilized to gather training data for an ANN model, which is designed to predict migration barriers for interstitial dumbbells in an equiatomic FeNiCrCoCu HEA. A 10×10×10 fcc lattice structure is constructed with five elements randomly distributed in equimolar proportions. As shown in Fig. 6.1(a), an initial dumbbell configuration (A-V1-B) is established by inserting an atom at the center of the lattice to form a [100] dumbbell, followed by simulating its migration to a [001] dumbbell (B-V2-C) using the NEB method. The NEB calculations specify 15 images and a spring constant of 10.0 eV/Å^2. The initial and final states of each migration event undergo relaxation via the conjugate gradient algorithm, adhering to a force stopping tolerance of 10^{-2} eV/Å and an energy convergence threshold of 0.0 eV, with a maximum number of iterations of 2,000. To obtain a sufficient dataset, the dumbbell positions are held constant while the surrounding atoms are randomly rearranged to produce a variety of

LACs, resulting in approximately 37,000 samples from the FeNiCrCoCu equiatomic composition for the development of the ANN model.

The feature input for the ANN model is derived from LAC characterizing both the initial and final states of the dumbbell configurations. The raw LAC gathers the types of elements extending to the i^{th} nearest neighbor (NN) shell around the central vacancy sites of the initial and final dumbbells, as shown in V1 or V2 in Fig. 6.1(a), with weights assigned to each NN shell reflecting their respective distances from the central vacancy, following the approach described in Section 4.2.2. In this work, the raw LACs are considered up to the 10^{th} NN because the spatial influence of an interstitial dumbbell is more significant than a vacancy [133]. Due to the complexity inherent in dumbbell configurations, rather than employing a one-hot encoding scheme as for the vacancy case, an embedding layer is utilized [134], permitting the ANN to determine the most effective representation of elemental types in "n" dimensions. This embedding layer is then followed by a flattened layer, six dense layers with "ReLU" activation and batch normalization, and a dropout layer to predict barrier energies, as illustrated in Fig. 6.1(b). After optimizing the ANN's hyperparameters, the embedding layer's output dimension is set to 10, with the six hidden layers comprising [512, 256, 128, 64, 32, 16] neurons, and a dropout rate of 0.2. The model performance is evaluated using the hold-out testing approach, partitioning the dataset into 90% for training and 10% for testing, with a further 20% of the training set reserved for validation purposes during the ANN model's training phase. Fig. 6.1(c) presents the model performance on the testing set, achieving a mean absolute error (MAE) of 11.6 meV and a Pearson correlation coefficient (R) of 0.98. These metrics suggest that the ANN model is highly accurate in predicting interstitial migration barriers. Therefore, by incorporating the ANN model into KMC simulations, interstitial

dumbbell simulations are expected to be improved further. Because in this approach, dumbbell migration barriers are predicted directly and without approximation as described in Equation (5.4).

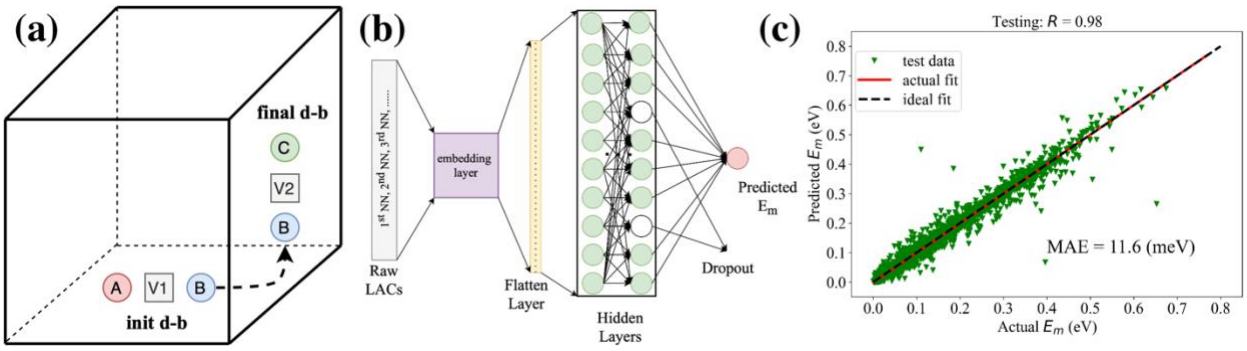

Fig. 6.1 (a) Schematic representation of the NEB calculation illustrating the migration of an interstitial dumbbell from the [100] to the [001] direction. (b) Diagram of the ANN model structure. (c) Performance metrics for the ANN model's prediction of migration barriers, with R representing the Pearson correlation coefficient and MAE denoting the mean absolute error.

6.2 Machine learning potential for HEAs

6.2.1 Introduction

Interatomic potentials are critical in MD simulations, describing how the potential energy varies with the positions of atoms. The traditional interatomic potentials, such as Lennard-Jones, Reactive Force Field (ReaxFF) [135], and Embedded-Atom Method (EAM)—the latter of which has been utilized in the previous chapters—rely on simplified mathematical models to approximate

atomic interactions within a system. This approximation facilitates the simulation of large systems over extensive periods, a primary advantage of their computational efficiency over the more computationally expensive ab initio MD simulations (AIMD). This efficiency is crucial for exploring material phenomena that would be too costly or impractical with more precise quantum mechanical methods such as AIMD, making these potentials invaluable for investigating processes like diffusion, phase transitions, and mechanical properties across a broad spectrum of materials. However, the simplicity of these empirical potentials also comes with limitations. Their accuracy is closely tied to the specific system and conditions they were developed for, often necessitating a compromise between generality and precision. Such potentials might not fully capture the complexity of atomic interactions in materials with elaborate electronic structures or in conditions significantly different from those they were designed for. This shortfall is particularly noticeable in studies involving new materials (such as HEAs), or complex defects, where the essential physics is not sufficiently represented by the potential.

ML potentials present a promising solution to address these limitations, providing a means to maintain the computational efficiency of empirical potentials while significantly improving their accuracy and range of applicability. By leveraging the data from detailed quantum mechanical calculations such as density-functional theory (DFT), ML potentials learn the intricate relationship between atomic configurations and their potential energies, thereby capturing the nuances of electronic interactions. Furthermore, as more training data are available, ML potentials can be systematically improved, allowing for ongoing refinement and adjustment to accommodate new materials and complex defects. This capacity for iterative improvement represents a marked advantage over traditional empirical potentials, which may necessitate thorough re-

parameterization to tackle new challenges. Four commonly used ML potentials are neural network potential (NNP) [136, 137], the Gaussian approximation (GAP) [138], the spectral neighbor potential (SNAP) [139, 140], and the moment tensor potential (MTP) [141]. In this work, an NNP is used to train a ML potential for an FeNiCrCoMn equiatomic HEA, chosen for its ubiquity and compatibility with LAMMPS. The training data for this model are collected from DFT calculations.

6.2.2 Preliminary methods and results

The special quasi-random structure (SQS) [142] method is employed to simulate random fcc structures in DFT calculations, a technique broadly utilized for assessing the synthesizability and diverse characteristics of multicomponent systems. The Alloy Theoretic Automated Toolkit (ATAT) [143] is used to generate the 2×2×5 supercell (80 atoms) of the equiatomic CoCrFeMnNi HEA with the cubic symmetry and ideal FCC lattice site occupations. Geometry optimization and determination of ground state energies are conducted using the Vienna Ab initio Simulation Package (VASP) [144], with the ion-core and valence-electron interactions being accounted for by the projector augmented wave (PAW) method [145]. The exchange-correlation functional is approximated by the generalized gradient approximation (GGA) as formulated by Perdew, Burke, and Ernzerhof (PBE) [146]. The simulations also incorporate an energy cutoff of 450 eV and a Monkhorst–Pack k-point mesh of 4 × 4 × 2. Energy minimization is converged until the total free energy variation falls below 10^{-4} eV and the forces on all atoms are smaller than 0.02 eV/Å.

The accuracy of a ML potential is fundamentally dependent on the quality of the training data, typically derived from costly first-principles calculations, such as DFT. To address this

constraint, an active learning strategy is adopted — an area of supervised learning that aims to develop a robust model with the least possible amount of training data [147]. In essence, this process begins by training four preliminary ANN models, each sharing the same architecture but initiated with distinct weights, on a limited dataset. This dataset contains configurations of both a perfect fcc lattice and a vacancy-containing structure, along with their respective ab initio calculated energies and forces. Subsequently, these models are employed within MD simulations to navigate a wider span of configurational space, acquiring on-the-fly feedback. When a particular configuration shows substantial discrepancies in the energies and forces predicted by the four models, it is flagged and subject to DFT simulations to ascertain its true energy and forces. These newly acquired configurations are then integrated into the training dataset, refining the four models iteratively. This cycle persists until the models have explored an extensive array of configurations and achieved convergence.

The DeePMD-kit package [148] is utilized for training ANN models, with MD simulations implemented in LAMMPS. Through active learning, these models explore configurations within both NVT (constant number of atoms, volume, and temperature) and NPT (constant number of atoms, pressure, and temperature) ensembles across temperatures ranging from 50 to 2000 K for both perfect fcc structures and those with a vacancy. The resultant training data consists of approximately 4,000 snapshots, with 90% being randomly selected for training the final ANN model and the remaining 10% designated for testing. The testing set yields a root mean square error (RMSE) of approximately 3 meV for energy and about 70 meV/Å for force per atom, demonstrating the ANN model's high accuracy in predicting energy and force across various conditions in this equiatomic HEA. This ANN model is then converted into an interatomic

potential for additional MD validation studies (ANN-MD). The first validation uses ANN-MD to optimize the lattice constant of two random structures, one with 108 atoms and the other with 4000 atoms. The results are compared with independent DFT simulations. The second validation involves calculating the chemical potentials for each species using ANN-MD (using the ML potential), comparing these results with those reported in the literature. Fig. 6.2 displays the total energy of CoCrFeMnNi as a function of lattice parameter from both ANN-MD and DFT simulations, showing closely matched trends and energies, indicating excellent agreement between ANN-MD and DFT simulations. For the chemical potential calculations, the Widom-type substitution method [56], detailed in Section 5.2.2, was applied. Table 6.1 presents the chemical potentials derived from ANN-MD simulations alongside previous ab initio results [46, 149, 150], revealing a strong alignment and further validating the reliability of the ANN potential, at least for the total energy calculations of the defect-free systems. In extend the capacity of the current ML potential to defective systems, such as those containing vacancies or interstitials, additional data and more careful parameter tuning are required.

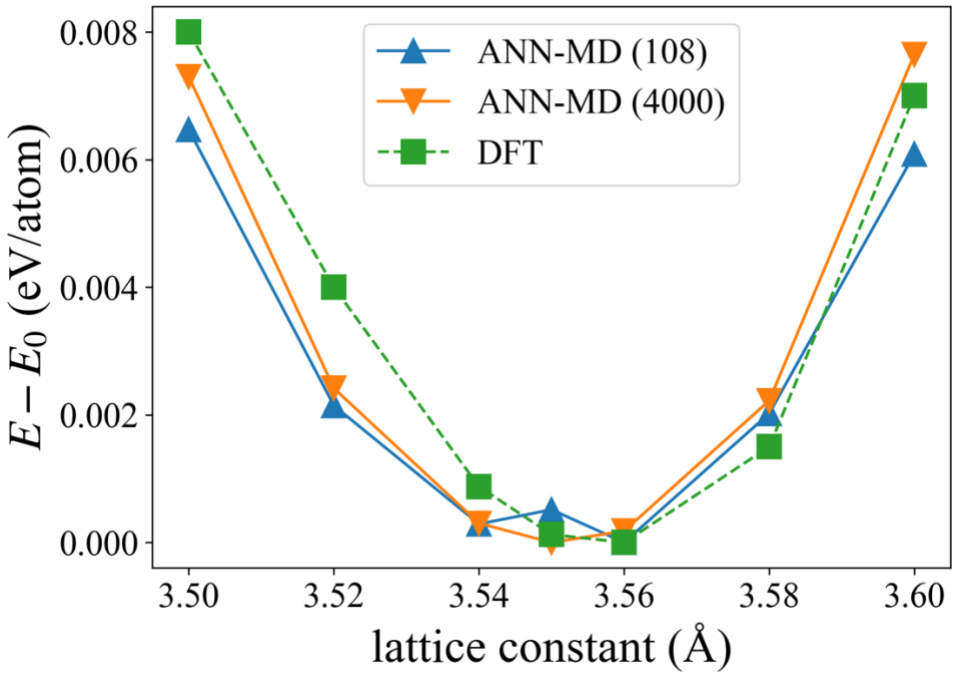

Fig. 6.2 Total energy of CoCrFeMnNi as a function of lattice parameter, derived from ANN-MD and DFT simulations.

Table 6.1 Mean chemical potential of each element in CoCrFeMnNi HEA from current work and previous studies. All energies are in eV/atom.

	current work	**Ref [150]**	**Ref [149]**	**Ref [46]**
μ_{Co}	-6.93	-6.86	-7.03	-7.10
μ_{Cr}	-9.45	-9.39	-9.35	-9.76
μ_{Fe}	-7.83	-8.10	-8.21	-8.38
μ_{Mn}	-8.95	-8.83	-9.00	-8.96
μ_{Ni}	-5.68	-5.40	-5.54	-5.56

List of Scientific Communications

Journal articles from this work and other collaborations

Huang, W., Farkas, D., & Bai, X. M. (2023). High-throughput machine learning-Kinetic Monte Carlo framework for diffusion studies in Equiatomic and Non-equiatomic FeNiCrCoCu high-entropy alloys. Materialia, 32, 101966

Huang, W., & Bai, X. M. (2023). Machine learning based on-the-fly kinetic Monte Carlo simulations of sluggish diffusion in Ni-Fe concentrated alloys. Journal of Alloys and Compounds, 937, 168457

Conference Presentation and Poster

Wenjiang Huang, Xianming Bai, *The Minerals, Metals & Materials Society (TMS)* (2021)

Wenjiang Huang, Xianming Bai, *The Minerals, Metals & Materials Society (TMS)* (2023)

Wenjiang Huang, Xianming Bai, *The Minerals, Metals & Materials Society (TMS)* (2024)

bibliography

[1] J.-W. Yeh, Alloy design strategies and future trends in high-entropy alloys. *Jom* **65**, 1759-1771 (2013).

[2] B. Gludovatz *et al.*, A fracture-resistant high-entropy alloy for cryogenic applications. *Science* **345**, 1153-1158 (2014).

[3] Y. F. Ye, Q. Wang, J. Lu, C. T. Liu, Y. Yang, High-entropy alloy: challenges and prospects. *Materials Today* **19**, 349-362 (2016).

[4] Y. Qiu, S. Thomas, M. A. Gibson, H. L. Fraser, N. Birbilis, Corrosion of high entropy alloys. *npj Materials degradation* **1**, 1-18 (2017).

[5] Y. W. Zhang *et al.*, Atomic-level heterogeneity and defect dynamics in concentrated solid-solution alloys. *Current Opinion in Solid State & Materials Science* **21**, 221-237 (2017).

[6] C. Lu *et al.*, Enhancing radiation tolerance by controlling defect mobility and migration pathways in multicomponent single-phase alloys. *Nature communications* **7**, 1-8 (2016).

[7] K. Y. Tsai, M. H. Tsai, J. W. Yeh, Sluggish diffusion in Co-Cr-Fe-Mn-Ni high-entropy alloys. *Acta Materialia* **61**, 4887-4897 (2013).

[8] C. Lu *et al.*, Radiation-induced segregation on defect clusters in single-phase concentrated solid-solution alloys. *Acta Materialia* **127**, 98-107 (2017).

[9] H.-W. Chang *et al.*, Influence of substrate bias, deposition temperature and post-deposition annealing on the structure and properties of multi-principal-component (AlCrMoSiTi) N coatings. *Surface and Coatings Technology* **202**, 3360-3366 (2008).

[10] D. B. Miracle, O. N. Senkov, A critical review of high entropy alloys and related concepts. *Acta Materialia* **122**, 448-511 (2017).

[11] J. Dąbrowa *et al.*, Demystifying the sluggish diffusion effect in high entropy alloys. *Journal of Alloys and Compounds* **783**, 193-207 (2019).

[12] S. V. Divinski, A. V. Pokoev, N. Esakkiraja, A. Paul, A mystery of" sluggish diffusion" in high-entropy alloys: the truth or a myth? *Diffusion foundations* **17**, 69-104 (2018).

[13] W. Kucza *et al.*, Studies of “sluggish diffusion” effect in Co-Cr-Fe-Mn-Ni, Co-Cr-Fe-Ni and Co-Fe-Mn-Ni high entropy alloys; determination of tracer diffusivities by combinatorial approach. *Journal of Alloys and Compounds* **731**, 920-928 (2018).

[14] A. Mehta, Y. Sohn, Investigation of sluggish diffusion in FCC Al0. 25CoCrFeNi high-entropy alloy. *Materials Research Letters* **9**, 239-246 (2021).

[15] E. Pickering, N. Jones, High-entropy alloys: a critical assessment of their founding principles and future prospects. *International Materials Reviews* **61**, 183-202 (2016).

[16] Y. N. Osetsky, L. K. Beland, A. V. Barashev, Y. W. Zhang, On the existence and origin of sluggish diffusion in chemically disordered concentrated alloys. *Current Opinion in Solid State & Materials Science* **22**, 65-74 (2018).

[17] B. Xu *et al.*, Exploring the influence of percolation on vacancy-mediated diffusion in CoCrNi multi-principal element alloys. *Materials & Design* **223**, 111238 (2022).

[18] F. X. Zhang *et al.*, Local Structure and Short-Range Order in a NiCoCr Solid Solution Alloy. *Physical review letters* **118**, 205501 (2017).

[19] J. Y. He *et al.*, A precipitation-hardened high-entropy alloy with outstanding tensile properties. *Acta Materialia* **102**, 187-196 (2016).

[20] T. Yang *et al.*, Multicomponent intermetallic nanoparticles and superb mechanical behaviors of complex alloys. *Science* **362**, 933-937 (2018).
[21] A. Seoane, D. Farkas, X.-M. Bai, Influence of compositional complexity on species diffusion behavior in high-entropy solid-solution alloys. *Journal of Materials Research* **37**, 1403-1415 (2022).
[22] S. L. Thomas, S. Patala, Vacancy diffusion in multi-principal element alloys: The role of chemical disorder in the ordered lattice. *Acta Materialia* **196**, 144-153 (2020).
[23] J. Kottke *et al.*, Experimental and theoretical study of tracer diffusion in a series of (CoCrFeMn) 100− xNix alloys. *Acta Materialia* **194**, 236-248 (2020).
[24] K. Ferasat *et al.*, Accelerated kinetic Monte Carlo: A case study; vacancy and dumbbell interstitial diffusion traps in concentrated solid solution alloys. *The Journal of Chemical Physics* **153**, 074109 (2020).
[25] G. Henkelman, B. P. Uberuaga, H. Jonsson, A climbing image nudged elastic band method for finding saddle points and minimum energy paths. *Journal of Chemical Physics* **113**, 9901-9904 (2000).
[26] N. Mousseau *et al.*, The activation-relaxation technique: Art nouveau and kinetic art. *Journal of Atomic and Molecular Physics* **2012** (2012).
[27] K. T. Butler, D. W. Davies, H. Cartwright, O. Isayev, A. Walsh, Machine learning for molecular and materials science. *Nature* **559**, 547-555 (2018).
[28] T. Mueller, A. G. Kusne, R. Ramprasad, Machine learning in materials science: Recent progress and emerging applications. *Reviews in computational chemistry* **29**, 186-273 (2016).
[29] Z. Fan, B. Xing, P. Cao, Predicting path-dependent diffusion barrier spectra in vast compositional space of multi-principal element alloys via convolutional neural networks. *Acta Materialia* **237**, 118159 (2022).
[30] B. Xu *et al.*, Exploring the influence of percolation on vacancy-mediated diffusion in CoCrNi multi-principal element alloys. *Materials & Design*, 111238 (2022).
[31] W. Huang, P. Martin, H. L. Zhuang, Machine-learning phase prediction of high-entropy alloys. *Acta Materialia* **169**, 225-236 (2019).
[32] Y. Ye, Q. Wang, J. Lu, C. Liu, Y. Yang, High-entropy alloy: challenges and prospects. *Materials Today* **19**, 349-362 (2016).
[33] N. K. Kumar, C. Li, K. Leonard, H. Bei, S. Zinkle, Microstructural stability and mechanical behavior of FeNiMnCr high entropy alloy under ion irradiation. *Acta Materialia* **113**, 230-244 (2016).
[34] Y. Shi, B. Yang, P. K. Liaw, Corrosion-resistant high-entropy alloys: A review. *Metals* **7**, 43 (2017).
[35] K.-Y. Tsai, M.-H. Tsai, J.-W. Yeh, Sluggish diffusion in co–cr–fe–mn–ni high-entropy alloys. *Acta Materialia* **61**, 4887-4897 (2013).
[36] Y. Zhao, H. Chen, Z. Lu, T. Nieh, Thermal stability and coarsening of coherent particles in a precipitation-hardened (NiCoFeCr) 94Ti2Al4 high-entropy alloy. *Acta Materialia* **147**, 184-194 (2018).
[37] M. Vaidya, S. Trubel, B. Murty, G. Wilde, S. V. Divinski, Ni tracer diffusion in CoCrFeNi and CoCrFeMnNi high entropy alloys. *Journal of Alloys and Compounds* **688**, 994-1001 (2016).

[38] E.-W. Huang *et al.*, Element effects on high-entropy alloy vacancy and heterogeneous lattice distortion subjected to quasi-equilibrium heating. *Scientific Reports* **9**, 1-10 (2019).
[39] A. Mehta, Y. H. Sohn, Fundamental core effects in transition metal high-entropy alloys:“High-entropy” and “sluggish diffusion” effects. *Diffusion Foundations* **29**, 75-93 (2021).
[40] B. Schönfeld *et al.*, Local order in Cr-Fe-Co-Ni: Experiment and electronic structure calculations. *Physical Review B* **99**, 014206 (2019).
[41] F. Zhang *et al.*, Local structure and short-range order in a NiCoCr solid solution alloy. *Physical review letters* **118**, 205501 (2017).
[42] X. Chen *et al.*, Direct observation of chemical short-range order in a medium-entropy alloy. *Nature* **592**, 712-716 (2021).
[43] Q. He *et al.*, Understanding chemical short-range ordering/demixing coupled with lattice distortion in solid solution high entropy alloys. *Acta Materialia* **216**, 117140 (2021).
[44] Z. Su *et al.*, Radiation-assisted chemical short-range order formation in high-entropy alloys. *Scripta Materialia* **212**, 114547 (2022).
[45] S. Zhao, Role of chemical disorder and local ordering on defect evolution in high-entropy alloys. *Physical Review Materials* **5**, 103604 (2021).
[46] H. Guan *et al.*, Chemical environment and magnetic moment effects on point defect formations in CoCrNi-based concentrated solid-solution alloys. *Acta Materialia* **187**, 122-134 (2020).
[47] A. Manzoor, Y. Zhang, Influence of Defect Thermodynamics on Self-Diffusion in Complex Concentrated Alloys with Chemical Ordering. *JOM* **74**, 4107-4120 (2022).
[48] B. Xing, X. Wang, W. J. Bowman, P. Cao, Short-range order localizing diffusion in multi-principal element alloys. *Scripta Materialia* **210**, 114450 (2022).
[49] W. Feng, Y. Qi, S. Wang, Effects of short-range order on the magnetic and mechanical properties of FeCoNi (AlSi) x high entropy alloys. *Metals* **7**, 482 (2017).
[50] M. Jin, P. Cao, M. P. Short, Thermodynamic mixing energy and heterogeneous diffusion uncover the mechanisms of radiation damage reduction in single-phase Ni-Fe alloys. *Acta Materialia* **147**, 16-23 (2018).
[51] S. Plimpton, Fast parallel algorithms for short-range molecular dynamics. *Journal of Computational Physics* **117**, 1-19 (1995).
[52] G. Bonny, D. Terentyev, R. C. Pasianot, S. Ponce, A. Bakaev, Interatomic potential to study plasticity in stainless steels: the FeNiCr model alloy. *Modelling and Simulation in Materials Science and Engineering* **19**, 085008 (2011).
[53] W. G. Hoover, Canonical dynamics: Equilibrium phase-space distributions. *Physical review A* **31**, 1695 (1985).
[54] M. P. Allen, D. J. Tildesley, *Computer simulation of liquids* (Oxford university press, 2017).
[55] J. M. Cowley, An Approximate Theory of Order in Alloys. *Physical Review* **77**, 669-675 (1950).
[56] B. Widom, Some topics in the theory of fluids. *The Journal of Chemical Physics* **39**, 2808-2812 (1963).

[57] Y. Zhang, A. Manzoor, C. Jiang, D. Aidhy, D. Schwen, A statistical approach for atomistic calculations of vacancy formation energy and chemical potentials in concentrated solid-solution alloys. *Computational Materials Science* **190**, 110308 (2021).
[58] A. Le Claire, Solute diffusion in dilute alloys. *Journal of nuclear materials* **69**, 70-96 (1978).
[59] S. Choudhury *et al.*, Ab-initio based modeling of diffusion in dilute bcc Fe–Ni and Fe–Cr alloys and implications for radiation induced segregation. *Journal of nuclear materials* **411**, 1-14 (2011).
[60] V. Ramunni, M. Pascuet, Mobility of U solutes in fcc Al: a theoretical model. *Procedia Materials Science* **8**, 451-460 (2015).
[61] X.-M. Bai, Y. Zhang, M. R. Tonks, Strain effects on oxygen transport in tetragonal zirconium dioxide. *Physical Chemistry Chemical Physics* **15**, 19438-19449 (2013).
[62] Y. N. Osetsky, L. K. Béland, R. E. Stoller, Specific features of defect and mass transport in concentrated fcc alloys. *Acta Materialia* **115**, 364-371 (2016).
[63] C. C. Fu, J. Dalla Torre, F. Willaime, J. L. Bocquet, A. Barbu, Multiscale modelling of defect kinetics in irradiated iron. *Nature Materials* **4**, 68-74 (2005).
[64] A. F. Voter, "Introduction to the kinetic Monte Carlo method" in Radiation effects in solids. (Springer, 2007), pp. 1-23.
[65] M. Trochet, N. Mousseau, L. K. Béland, G. Henkelman, Off-lattice kinetic Monte Carlo methods. *Handbook of Materials Modeling: Methods: Theory and Modeling*, 715-743 (2020).
[66] F. El-Mellouhi, N. Mousseau, L. J. Lewis, Kinetic activation-relaxation technique: An off-lattice self-learning kinetic Monte Carlo algorithm. *Physical Review B* **78**, 153202 (2008).
[67] L. K. Béland, P. Brommer, F. El-Mellouhi, J.-F. Joly, N. Mousseau, Kinetic activation-relaxation technique. *Physical Review E* **84**, 046704 (2011).
[68] H. Jónsson, G. Mills, K. W. Jacobsen, "Nudged elastic band method for finding minimum energy paths of transitions" in Classical and quantum dynamics in condensed phase simulations. (World Scientific, 1998), pp. 385-404.
[69] G. Henkelman, H. Jónsson, Improved tangent estimate in the nudged elastic band method for finding minimum energy paths and saddle points. *The Journal of Chemical Physics* **113**, 9978-9985 (2000).
[70] N. Mousseau *et al.*, The activation-relaxation technique: Art nouveau and kinetic art. *Journal of Atomic and Molecular Physics* **2012**, 14 (2012).
[71] Z. Shen *et al.*, Kinetic Monte Carlo simulation framework for chemical short-range order formation kinetics in a multi-principal-element alloy. *Computational Materials Science* **198**, 110670 (2021).
[72] M. R. Sorensen, A. F. Voter, Temperature-accelerated dynamics for simulation of infrequent events. *The Journal of Chemical Physics* **112**, 9599-9606 (2000).
[73] E. Wigner, F. Seitz, On the constitution of metallic sodium. *Physical Review* **43**, 804 (1933).
[74] S. M. Shakhno, O. P. Gnatyshyn, Algorithm for the solution of a nonlinear least squares problem under secondary conditions. *Zeitschrift Fur Angewandte Mathematik Und Mechanik* **81**, S1023-S1024 (2001).

[75] N. Castin, J. R. Fernandez, R. C. Pasianot, Predicting vacancy migration energies in lattice-free environments using artificial neural networks. *Computational Materials Science* **84**, 217-225 (2014).
[76] N. Castin, L. Malerba, Prediction of point-defect migration energy barriers in alloys using artificial intelligence for atomistic kinetic Monte Carlo applications. *Nuclear Instruments & Methods in Physics Research Section B-Beam Interactions with Materials and Atoms* **267**, 3148-3151 (2009).
[77] M. Leetmaa, N. V. Skorodumova, KMCLib: A general framework for lattice kinetic Monte Carlo (KMC) simulations. *Computer Physics Communications* **185**, 2340-2349 (2014).
[78] H. Mehrer, *Diffusion in solids: fundamentals, methods, materials, diffusion-controlled processes* (Springer Science & Business Media, 2007), vol. 155.
[79] V. A. Borodin, P. V. Vladimirov, A. Moslang, Lattice kinetic Monte-Carlo modelling of helium-vacancy cluster formation in bcc iron. *Journal of Nuclear Materials* **367**, 286-291 (2007).
[80] C. S. Deo *et al.*, Helium bubble nucleation in bcc iron studied by kinetic Monte Carlo simulations. *Journal of nuclear materials* **361**, 141-148 (2007).
[81] D. Terentyev, N. Juslin, K. Nordlund, N. Sandberg, Fast three dimensional migration of He clusters in bcc Fe and Fe-Cr alloys. *Journal of Applied Physics* **105**, 103509 (2009).
[82] M. I. Pascuet, N. Castin, C. S. Becquart, L. Malerba, Stability and mobility of Cu-vacancy clusters in Fe-Cu alloys: A computational study based on the use of artificial neural networks for energy barrier calculations. *Journal of Nuclear Materials* **412**, 106-115 (2011).
[83] A. F. Voter, F. Montalenti, T. C. Germann, Extending the time scale in atomistic simulation of materials. *Annual review of materials research* **32**, 321-346 (2002).
[84] B. P. Uberuaga, A. F. Voter, "Accelerated molecular dynamics methods" in Radiation Effects in Solids. (Springer, 2007), pp. 25-43.
[85] X.-M. Bai, A. F. Voter, R. G. Hoagland, M. Nastasi, B. P. Uberuaga, Efficient annealing of radiation damage near grain boundaries via interstitial emission. *Science* **327**, 1631-1634 (2010).
[86] X.-M. Bai, A. El-Azab, J. Yu, T. R. Allen, Migration mechanisms of oxygen interstitial clusters in UO2. *Journal of Physics: Condensed Matter* **25**, 015003 (2012).
[87] L. Kong, L. J. Lewis, Transition state theory of the preexponential factors for self-diffusion on Cu, Ag, and Ni surfaces. *Physical Review B* **74**, 073412 (2006).
[88] K. Ferasat *et al.*, Accelerated kinetic Monte Carlo: A case study; vacancy and dumbbell interstitial diffusion traps in concentrated solid solution alloys. *Journal of Chemical Physics* **153**, 074109 (2020).
[89] S. J. Zhao, Y. Osetsky, Y. W. Zhang, Diffusion of point defects in ordered and disordered Ni-Fe alloys. *Journal of Alloys and Compounds* **805**, 1175-1183 (2019).
[90] J. W. Yeh *et al.*, Nanostructured high-entropy alloys with multiple principal elements: novel alloy design concepts and outcomes. *Advanced engineering materials* **6**, 299-303 (2004).
[91] Y. Jien-Wei, Recent progress in high entropy alloys. *Ann. Chim. Sci. Mat* **31**, 633-648 (2006).

[92] P. Brown, H. Zhuang, Quantum machine-learning phase prediction of high-entropy alloys. *Materials Today* **63**, 18-31 (2023).
[93] S. Praveen, H. S. Kim, High-entropy alloys: potential candidates for high-temperature applications–an overview. *Advanced engineering materials* **20**, 1700645 (2018).
[94] D. Liu *et al.*, Exceptional fracture toughness of CrCoNi-based medium-and high-entropy alloys at 20 kelvin. *Science* **378**, 978-983 (2022).
[95] H. Cheng *et al.*, Corrosion-resistant high-entropy alloy coatings: a review. *Journal of The Electrochemical Society* **168**, 111502 (2021).
[96] C. Lu *et al.*, Enhancing radiation tolerance by controlling defect mobility and migration pathways in multicomponent single-phase alloys. *Nature communications* **7**, 13564 (2016).
[97] Z. Li, K. G. Pradeep, Y. Deng, D. Raabe, C. C. Tasan, Metastable high-entropy dual-phase alloys overcome the strength–ductility trade-off. *Nature* **534**, 227-230 (2016).
[98] A. Seoane, D. Farkas, X.-M. Bai, Molecular dynamics studies of sluggish grain boundary diffusion in equiatomic FeNiCrCoCu high-entropy alloy. *Journal of Materials Science*, 1-17 (2023).
[99] Y. Osetsky, A. V. Barashev, Y. Zhang, Sluggish, chemical bias and percolation phenomena in atomic transport by vacancy and interstitial diffusion in NiFe alloys. *Current Opinion in Solid State and Materials Science* **25**, 100961 (2021).
[100] C. Varvenne, A. Luque, W. G. Nöhring, W. A. Curtin, Average-atom interatomic potential for random alloys. *Physical Review B* **93**, 104201 (2016).
[101] B. Xu *et al.*, Mechanism of sluggish diffusion under rough energy landscape. *Cell Reports Physical Science* (2023).
[102] B. Xu *et al.*, Influence of short-range order on diffusion in multiprincipal element alloys from long-time atomistic simulations. *Physical Review Materials* **7**, 033605 (2023).
[103] B. Xu *et al.*, Revealing the crucial role of rough energy landscape on self-diffusion in high-entropy alloys based on machine learning and kinetic Monte Carlo. *Acta Materialia* **234**, 118051 (2022).
[104] W. Huang, X.-M. Bai, Machine learning based on-the-fly kinetic Monte Carlo simulations of sluggish diffusion in Ni-Fe concentrated alloys. *Journal of Alloys and Compounds* **937**, 168457 (2023).
[105] D. Farkas, A. Caro, Model interatomic potentials and lattice strain in a high-entropy alloy. *Journal of Materials Research* **33**, 3218-3225 (2018).
[106] M. Asadikiya *et al.*, A review of the design of high-entropy aluminum alloys: a pathway for novel Al alloys. *Journal of Materials Science* **56**, 12093-12110 (2021).
[107] N. Castin, L. Malerba, Calculation of proper energy barriers for atomistic kinetic Monte Carlo simulations on rigid lattice with chemical and strain field long-range effects using artificial neural networks. *The Journal of Chemical Physics* **132** (2010).
[108] J. Cieslak *et al.*, Multi-phase nature of sintered vs. arc-melted CrxAlFeCoNi high entropy alloys-experimental and theoretical study. *Journal of Alloys and Compounds* **801**, 511-519 (2019).
[109] A. Munitz, M. Kaufman, R. Abbaschian, Liquid phase separation in transition element high entropy alloys. *Intermetallics* **86**, 59-72 (2017).
[110] W. Shinoda, M. Shiga, M. Mikami, Rapid estimation of elastic constants by molecular dynamics simulation under constant stress. *Physical Review B* **69**, 134103 (2004).

[111] V. Borodin, P. Vladimirov, A. Möslang, Lattice kinetic Monte-Carlo modelling of helium–vacancy cluster formation in bcc iron. *Journal of nuclear materials* **367**, 286-291 (2007).
[112] M. Vaidya, K. Pradeep, B. Murty, G. Wilde, S. Divinski, Bulk tracer diffusion in CoCrFeNi and CoCrFeMnNi high entropy alloys. *Acta Materialia* **146**, 211-224 (2018).
[113] M. S. Daw, M. Chandross, Sluggish diffusion in random equimolar FCC alloys. *Physical Review Materials* **5**, 043603 (2021).
[114] J. Dąbrowa, M. Danielewski, State-of-the-art diffusion studies in the high entropy alloys. *Metals* **10**, 347 (2020).
[115] M. Vaidya, K. Pradeep, B. Murty, G. Wilde, S. Divinski, Radioactive isotopes reveal a non sluggish kinetics of grain boundary diffusion in high entropy alloys. *Scientific reports* **7**, 12293 (2017).
[116] K. Compaan, Y. Haven, Correlation factors for diffusion in solids. *Transactions of the Faraday Society* **52**, 786-801 (1956).
[117] J. W. Haus, K. W. Kehr, Diffusion in regular and disordered lattices. *Physics Reports* **150**, 263-406 (1987).
[118] I. Webman, Effective-medium approximation for diffusion on a random lattice. *Physical review letters* **47**, 1496 (1981).
[119] N. Castin, L. Messina, C. Domain, R. C. Pasianot, P. Olsson, Improved atomistic Monte Carlo models based on ab-initio-trained neural networks: Application to FeCu and FeCr alloys. *Physical Review B* **95**, 214117 (2017).
[120] A. Manzoor *et al.*, Machine learning based methodology to predict point defect energies in multi-principal element alloys. *Frontiers in Materials* **8**, 673574 (2021).
[121] L. Qiao, Y. Liu, J. Zhu, A focused review on machine learning aided high-throughput methods in high entropy alloy. *Journal of Alloys and Compounds* **877**, 160295 (2021).
[122] K. Ferasat *et al.*, Accelerated kinetic Monte Carlo: A case study; vacancy and dumbbell interstitial diffusion traps in concentrated solid solution alloys. *The Journal of Chemical Physics* **153** (2020).
[123] W. Huang, D. Farkas, X.-M. Bai, High-throughput machine learning-Kinetic Monte Carlo framework for diffusion studies in Equiatomic and Non-equiatomic FeNiCrCoCu high-entropy alloys. *Materialia* **32**, 101966 (2023).
[124] D. S. Aidhy *et al.*, Point defect evolution in Ni, NiFe and NiCr alloys from atomistic simulations and irradiation experiments. *Acta Materialia* **99**, 69-76 (2015).
[125] Y. Zhang *et al.*, Influence of chemical disorder on energy dissipation and defect evolution in concentrated solid solution alloys. *Nature communications* **6**, 8736 (2015).
[126] A. Stukowski, Visualization and analysis of atomistic simulation data with OVITO–the Open Visualization Tool. *Modelling and simulation in materials science and engineering* **18**, 015012 (2009).
[127] B. Puchala, M. L. Falk, K. Garikipati, An energy basin finding algorithm for kinetic Monte Carlo acceleration. *The Journal of Chemical Physics* **132** (2010).
[128] S. T. Dunham, C. D. Wu, Atomistic models of vacancy-mediated diffusion in silicon. *Journal of Applied Physics* **78**, 2362-2366 (1995).
[129] E. Alpaydin, *Machine learning* (MIT press, 2021).

[130] S. Zhao, G. M. Stocks, Y. Zhang, Defect energetics of concentrated solid-solution alloys from ab initio calculations: Ni 0.5 Co 0.5, Ni 0.5 Fe 0.5, Ni 0.8 Fe 0.2 and Ni 0.8 Cr 0.2. *Physical Chemistry Chemical Physics* **18**, 24043-24056 (2016).
[131] Y. Osetsky *et al.*, Tunable chemical complexity to control atomic diffusion in alloys. *npj Computational Materials* **6**, 38 (2020).
[132] N. Peterson, Self-diffusion in pure metals. *Journal of nuclear materials* **69**, 3-37 (1978).
[133] B. Xu *et al.*, Sluggish and Chemically-Biased Interstitial Diffusion in Concentrated Solid Solution Alloys: Mechanisms and Methods. *arXiv preprint arXiv:2311.16727* (2023).
[134] M. Abadi *et al.*, Tensorflow: Large-scale machine learning on heterogeneous distributed systems. *arXiv preprint arXiv:1603.04467* (2016).
[135] A. C. Van Duin, S. Dasgupta, F. Lorant, W. A. Goddard, ReaxFF: a reactive force field for hydrocarbons. *The Journal of Physical Chemistry A* **105**, 9396-9409 (2001).
[136] J. Behler, M. Parrinello, Generalized neural-network representation of high-dimensional potential-energy surfaces. *Physical review letters* **98**, 146401 (2007).
[137] L. Zhang, J. Han, H. Wang, R. Car, E. Weinan, Deep potential molecular dynamics: a scalable model with the accuracy of quantum mechanics. *Physical review letters* **120**, 143001 (2018).
[138] A. P. Bartók, M. C. Payne, R. Kondor, G. Csányi, Gaussian approximation potentials: The accuracy of quantum mechanics, without the electrons. *Physical review letters* **104**, 136403 (2010).
[139] A. P. Thompson, L. P. Swiler, C. R. Trott, S. M. Foiles, G. J. Tucker, Spectral neighbor analysis method for automated generation of quantum-accurate interatomic potentials. *Journal of Computational Physics* **285**, 316-330 (2015).
[140] M. A. Wood, A. P. Thompson, Extending the accuracy of the SNAP interatomic potential form. *The Journal of Chemical Physics* **148** (2018).
[141] I. S. Novikov, K. Gubaev, E. V. Podryabinkin, A. V. Shapeev, The MLIP package: moment tensor potentials with MPI and active learning. *Machine Learning: Science and Technology* **2**, 025002 (2020).
[142] A. Zunger, S.-H. Wei, L. Ferreira, J. E. Bernard, Special quasirandom structures. *Physical review letters* **65**, 353 (1990).
[143] A. Van de Walle *et al.*, Efficient stochastic generation of special quasirandom structures. *Calphad* **42**, 13-18 (2013).
[144] G. Kresse, J. Hafner, Ab initio molecular dynamics for liquid metals. *Physical Review B* **47**, 558 (1993).
[145] P. E. Blöchl, Projector augmented-wave method. *Physical Review B* **50**, 17953 (1994).
[146] J. P. Perdew, K. Burke, M. Ernzerhof, Generalized gradient approximation made simple. *Physical review letters* **77**, 3865 (1996).
[147] L. Zhang, D.-Y. Lin, H. Wang, R. Car, E. Weinan, Active learning of uniformly accurate interatomic potentials for materials simulation. *Physical Review Materials* **3**, 023804 (2019).
[148] H. Wang, L. Zhang, J. Han, E. Weinan, DeePMD-kit: A deep learning package for many-body potential energy representation and molecular dynamics. *Computer Physics Communications* **228**, 178-184 (2018).

[149] M. Mizuno, K. Sugita, H. Araki, Defect energetics for diffusion in CrMnFeCoNi high-entropy alloy from first-principles calculations. *Computational Materials Science* **170**, 109163 (2019).
[150] C. Wang *et al.*, First-principles study of hydrogen-vacancy interactions in CoCrFeMnNi high-entropy alloy. *Journal of Alloys and Compounds* **922**, 166259 (2022).